Carl von Ossietzky Universität Oldenburg

Performance Optimization of Cu(In$_{1-x}$,Ga$_x$)(Se$_{1-y}$,S$_y$)$_2$ Thin-Film Solar Cells by Characterization and Modelling of Temperature and Low-Light Behavior

Der Fakultät für Mathematik und Naturwissenschaften

der Carl von Ossietzky Universität Oldenburg

zur Erlangung des Grades und Titels eines

Doktors der Naturwissenschaften (Dr. rer. nat.)

angenommene Dissertation

von

Hamsa Ahmed

geboren am 16.09.1991

in Alexandria (Ägypten)

*"Let us see how high we can fly before
the sun melts the wax in our wings"*

Edward O. Wilson

Abstract

The standard test conditions (STC) normally used to characterize solar cells are rarely reached outdoors due to the varied weather over the year. Therefore, STC solar cell efficiencies are not the only parameters that define their performance, and other factors become relevant under real atmospheric conditions. The main ones that affect solar cells application significantly, are their stable performance under different temperatures (T) and intensities since the output power of solar cells drops upon increasing temperatures and decreasing intensities. One of the advantages of thin film solar cells based on Cu (In,Ga) (Se,S)$_2$ (CIGS) is their lower sensitivity towards temperature, compared to mono and poly-crystalline Si. Nevertheless, they are known to induce metastable performance upon light exposure. Despite intensive research for several years in the metastability of CIGS thin film solar cells, still some puzzling phenomena and physiochemical characteristics have not been fully understood. Therefore, to further improve and to tailor CIGS temperature coefficients, low light performance, and metastable behavior, it is crucial to gain a detailed understanding of the microscopic mechanisms involved. In this work, the impact of structural variations of CIGS solar cells on their temperature coefficients, their stability, and their low light performance is studied. The layer modifications implemented for this study include different buffer, window layers and back contacts materials, and different double graded absorbers with change in their thickness and sodium post deposition treatment.

For this purpose, various characterization techniques were performed on the varied solar cells. For instance, temperature dependent IV (IV(T)) and external quantum efficiency (EQE(T)), glow discharge optical emission spectroscopy (GDOES) and capacitance voltage (CV) measurements were performed in order to experimentally assess the underlying mechanism that led to an enhancing or detrimental impact on the temperature coefficient values. Spectral dependence EQE (λ), IV (λ), IV(T) and temperature dependent CV (CV(T)) were used to study the mechanisms involved in the metastability of the solar cell. Intensity dependent IV and IV(T, λ) measurements were performed for inspecting the low light performance of these structures. To study the elemental interdiffusion between different layers, TEM/EDX measurements were performed. The one diode model was used to evaluate the fundamental solar cells' physical parameters and their influence on the temperature coefficient.

It was demonstrated that the absorber layer exhibits the largest influence on the temperature dependence of the power output amongst all modified layers of the structure. The buffer and the absorber elemental composition showed to play an important role in the elemental

I

interdiffusion and hence led to the creation of amphoteric defects that are light and temperature sensitive. Studies on the impact of different solar cell structures on the shift of the dominant recombination region at different light intensities were also performed. For this study, a normalized activation energy parameter is introduced to account for the dominant recombination region with respect to the absorber minimum band gap location. It was found that decreasing the recombination in the buffer/window region leads to a remarkable conversion efficiency resilience at different light intensities.

Kurzfassung

Die Standard Test Bedingungen (STC, standard test conditions), welche normalerweise zur Charakterisierung von Solarzellen genutzt werden, werden im Freien aufgrund der über das Jahr variierenden Witterung selten erreicht. Daher sind die STC-Wirkungsgrade von Solarzellen nicht die einzigen Parameter, die ihre Leistung definieren, und andere Faktoren werden unter realen atmosphärischen Bedingungen relevant. Die Leistung der Solarzellen wird maßgeblich durch ihre Abhängigkeit von Temperatur (T) und Lichtintensität beeinflusst. Bei steigenden Temperaturen und abnehmenden Intensitäten sinkt die Leistung. Einer der Vorteile von Dünnschichtsolarzellen auf Basis von Cu(In,Ga) (S,Se)$_2$ (CIGS) ist ihre geringere Temperaturempfindlichkeit im Vergleich zu mono- und polykristallinem Si. Dennoch sind sie dafür bekannt, dass sie bei Lichteinwirkung eine metastabile Leistung aufweisen. Trotz mehrjähriger, intensiver Forschung zur Metastabilität von CIGS-Dünnschichtsolarzellen sind einige Phänomene und physiochemische Eigenschaften noch nicht vollständig verstanden. Um die CIGS-Temperaturkoeffizienten, die Schwachlichtleistung und das metastabile Verhalten weiter zu verbessern und anzupassen, ist es daher entscheidend, ein detailliertes Verständnis der beteiligten mikroskopischen Mechanismen zu gewinnen. In dieser Arbeit wird der Einfluss struktureller Variationen von CIGS-Solarzellen auf deren Temperaturkoeffizienten, ihre Stabilität und ihre Schwachlichtleistung untersucht. Die für diese Studie durchgeführten Schichtmodifikationen umfassen verschiedene Puffer, Fensterschichten und Rückkontaktschichten sowie verschiedene doppelt abgestufte Absorber mit veränderter in der Dicke und der Natrium-Nachbehandlung.

Zu diesem Zweck wurden verschiedene Charakterisierungstechniken an den variierten Solarzellen durchgeführt. Zum Beispiel wurden temperaturabhängige *IV*- Kennlinien (IV(T)) und externe Quanteneffizienz (EQE(T)), optische Glimmentladungs-Emissionsspektroskopie (GDOES, glow discharge optical emission spectorcopy) und Kapazitätsspannungsmessungen (CV, capacitance voltage) durchgeführt, um den zugrundeliegenden Mechanismus experimentell zu bewerten, der zu einem verstärkenden oder nachteiligen Einfluss auf die Größe des Temperaturkoeffizienten führte. Spektralabhängige EQE(λ), IV(λ), IV(T) und temperaturabhängige CV (CV(T)) wurden verwendet, um die Mechanismen zu untersuchen, die an der Metastabilität der Solarzelle beteiligt sind. Intensitätsabhängige IV- und IV(T, λ)-Messungen wurden durchgeführt, um die Schwachlichtleistung dieser Strukturen zu untersuchen. Um die elementare Interdiffusion zwischen den verschiedenen Schichten zu untersuchen, wurden transmission elektron microscopie/energy dispersiv x-strahl TEM/EDX-

Messungen durchgeführt. Das Ein-Dioden-Modell wurde verwendet, um die grundlegenden physikalischen Parameter der Solarzellen und ihren Einfluss auf den Temperaturkoeffizienten zu bewerten.

Es konnte gezeigt werden, dass die Absorberschicht von allen modifizierten Schichten der Struktur den größten Einfluss auf die Temperaturabhängigkeit der Ausgangsleistung aufweist. Es zeigte sich, dass die Elementzusammensetzung des Puffers und des Absorbers eine wichtige Rolle bei der Elementinterdiffusion spielt und somit zur Bildung von amphoteren Defekten führt, die licht- und temperaturempfindlich sind. Untersuchungen zum Einfluss verschiedener Solarzellenstrukturen auf die Verschiebung die dominante Rekombination bei unterschiedlichen Lichtintensitäten wurden ebenfalls durchgeführt. Für diese Studie wurde ein normalisierter Aktivierungsenergie-Parameter eingeführt, um die dominante Rekombinationsregion in Bezug auf die Lage der minimalen Bandlücke des Absorbers zu berücksichtigen. Es wurde festgestellt, dass die Verringerung der Rekombination im Puffer-/Fensterbereich zu einer bemerkenswerten Umwandlungseffizienz-Resilienz bei verschiedenen Lichtintensitäten führt.

List of Figures

List of Tables

Content

Chapter 1 Introduction to photovoltaics

By 2040, it is expected that the worldwide energy demand will increase by more than a quarter as consequence of the 1.7 billion population growth [1]. Therefore, the annual increase in global energy consumption, associated with the increase in world population are playing a big role in the necessity of developing sustainable and environmentally friendly energy sources for replacing the carbonized conventional energy sources such as coal, crude oil, and others.

The International Energy Agency (IEA) has forecasted highly undesirable detrimental climate consequences such as global warming, flooding and extinction of many species due to the future energy demands, unless renewable energy sources become persistently implemented [1]. Therefore, it is urgently required to extensively prevail sustainable and efficient renewable energy sources, such as wind, geothermal, biomass and solar photovoltaics (PV), as an alternative to conventional associated greenhouse gases sources. Over the last decade, PV has strikingly grown in global installations by 35% on a yearly basis, showing an exponential increase [2]. In 2019, China has led both, the PV global production with a 66% share and by 36% of the cumulative global PV installation [3]. The recent statistics has shown that the solar renewable technologies are of great interest to the world, systems powered by solar energy share up to 60% of the overall capacity growth [4]. This indicates the prominence of PV technology as being a reliable power supply contributing to the total global power generation, which is beneficial to reach independence from fossil energy.

1.1 Solar cells evolution history

In the 1800s, PV technologies study were introduced, and in 1954 the first solar cell was invented by D. Chapin, C. Fuller, and P. Pearson in Bell labs [5]. From 1960-1980, PV technology has been extended to the power scale. After 2000, the cost and efficiency of solar cells were greatly developed. There are several types of solar cells PV technologies which differ in their materials properties, manufacturing processes and energy payback time. First generation solar cells based on silicon (Si), such as mono or poly-crystalline, are the oldest and with major presence in the market due to their high efficiency [4], [6]. Nevertheless, their light absorbing material thickness is up to 350 µm, and they require expensive fabrication technology. Therefore, the need of another alternative technology for reducing the material used in fabrication as well as the cost led to the onset of thin film technology.

Thin-film solar cells with absorber thickness in the order of one μm such as cadmium telluride, amorphous silicon, and Cu (In, Ga) (Se, S)$_2$ (CIGS) are called second-generation technologies. They showed to be highly competitive with Si first-generation technology, as they have a comparable efficiency and a relatively lower cost [7]. The highest efficiency among thin film solar cells is 23.4% reported for CIGS in 2019 [8]. One of the main advantages of this technology is its stability over long time without a significant degradation [9]. Finally, the third-generation photovoltaics such as perovskite, quantum dot and dye-synthesized are known to be promising for the future energy development. However, their degradation of efficiency over time is a certain concern and therefore these are not yet commercially present [10], [11]. The focus of this thesis will be only on the second-generation CIGS technology.

1.1.1 CIGS solar cell technology review

In 1953, Hahn *et al*. [12] reported the synthesis of CuInSe$_2$ for the first time. In 1976, Kazmerski *et al*. implemented the first thin film CIGS with conversion efficiency 4.5%. Few years later, they improved the efficiency by 1.2% [13], using indium fingered contact as a front electrode. The increase in the efficiency was attributed to enhancement of the radiation transmission, which render the window layer's absorption to increase. Additionally, the adequate lattice match between InP and CISe$_2$ mitigated the interfacial defects.

An efficiency of 10.6% was recorded by Mikkelsen and Chen [14], who incorporated Zn in the CdS buffer, that results in a perfect crystallinity between Buffer and absorber. Consequently, the open circuit voltage (V_{oc}) and short circuit current density (J_{sc}) improved due to the reduction of grain boundaries. In 1994, Gabor *et al*. [15], increased the efficiency of CIGS to 15.9%, by using (In$_x$Ga$_{1-x}$)Se$_3$ and graded Ga content with the absorber depth. In 2013, the Swiss Federal laboratories for materials science and technology (EMPA) achieved efficiency of 20.4 % [16] for CIGS on a flexible polymer substrate, and it was the first time that the efficiency of CIGS on polymer substrate exceeded the glass based CIGS, this was attributed to the post deposition treatment of potassium (K PDT). This accomplishment was following the center for solar energy and hydrogen research, ZSW in Germany, where an efficiency of 20.3% was recorded as breaking the 20% barrier for CIGS based on glass at that time. This achievement included metal contacts, and a K PDT was carried out [17]. The most recent and highest record efficiency in 2020, was achieved by Solar frontier, 23.5% with Cd-free CIGS on a glass substrate. The success was referred to the implementation of double buffer layers

$Zn(O,S,OH)_x/Zn_{0.8}Mg_{0.2}O$ [18], which reflects on a considerable decrease of the open circuit voltage deficit (V_{oc},def)**,** and increase of carrier lifetime.

CIGS are used for a wide range of applications due to their high absorption coefficient in the visible spectrum [19], lightweight and flexibility [20], ease of fabrication [21], and the optoelectronic tunability of their band gap between 1.0 and 2.4 eV [22].

As a result of extensive research, it has been concluded that the absorber' s material properties and hence, the layers' interfaces quality play a significant role in solar cell recombination losses [23], [24]. The microscopic argument is mainly attributed to the carriers' mobilities, the density of carriers and defects [25]. Consequently, adverse fabrication techniques have been performed in order to diminish those losses. For instance, the V_{oc},def, an indicator of recombination losses, can be enhanced with an appropriate absorber tuning of the Ga/(Ga+In) (GGI) and/or S/(S+Se) (SSSe) ratios [26]. Alkali metal post deposition treatment has showed an improvement in the performance due to the increase in carrier life time [27].

1.1.2 Temperature coefficient overview

PV installed modules perform differently under climate conditions subjected to the geographical location. For instance, thin film technologies are more suitable to work in sunbelt countries, where the temperature is relatively higher, owing to the fact that they have lower temperature sensitivity compared to crystalline Si [28]–[30]. Such conditions like temperature and low light intensities promote industrial customization of solar cell technology at different atmospheric conditions, since under real operating conditions the main solar cell parameters deviate significantly from the STC values [31], [32]. Optimizing the module power at STC (25°C, 1000 W/m², AM1.5 spectrum) is no longer the only aimed benchmark [33]. Therefore, it is essential to appropriately account for the installation site before designing the PV system [6]. To be able to describe the temperature dependence of solar cell parameters, a parameter called temperature coefficient is desired. This term can be approximately considered to be independent of temperature [34]. Different analytical expressions for solar cell parameters' temperature coefficients (β_X, with X being the parameter of interest, ie. V_{oc}, Fill Factor FF or J_{sc}) have been derived from the ideal diode theory [35]. In 2012, Singh and Ravindra realized that the temperature behavior of the main solar cells parameters like the V_{oc}, power at maximum power point (P_{mpp}) and FF of different technologies like Si, GaAs, InP, CdTe and CdS are linearly decreasing with increasing temperature, while the J_{sc} increases slightly with increasing temperature [36]. Similarly for CIGS solar cells, the previously mentioned linear behavior was

observed [6], [37]. In 2015, Dupré *et al.* [38], discussed the physics ruling the solar cell parameters' temperature coefficients. It was argued that the physics of β_{Voc} can be explained by the temperature dependence of the detailed balance. Furthermore, β_{FF}, in an ideal case, is neatly related to the V_{oc}, but in a non-ideal case it also depends on transport properties like the contact resistance of the PV technology. Additionally, β_{Jsc} of indirect band gap semiconductors is dependent on the incident photon's collection fraction. It was also mentioned that the uncommon positive band gap behavior of perovskite such as $CH_3NH_3PbI_{3-x}Cl_x$ and $CsSnI_3$ with temperature, explains these materials' negative β_{Jsc} [34], [39]. One year after, they reported the investigation of Si solar cells' β_X, and it was concluded that external radiative efficiency of PV cells influence the β_{Voc} substantially [35].

Most of the studies reported in literature have focused on the temperature dependence of V_{oc} [35], [36], [40], since they attributed the decrease in the solar cell parameters with increasing T to the decrease in V_{oc}. In 2012, Löper *et al.* [41] observed that in crystalline Si solar cells the T dependence of the band gap (E_g) significantly impacts $V_{oc}(T)$, whereas, the T dependences of doping density and effective masses do not play a big role. In 2014, Schubbert *et al.* [42] concluded from their simulation studies that an increase in the minimum band gap from a variation in Ga content enhances the V_{oc} and in turn also $\beta_{Voc,rel}$. In 2019, the effect of V_{oc} on β_{Voc} was also shown by Kata *et al.* [43]. Also, in 2015, Grover *et al.* [44] showed the importance of the interface quality on β_{Voc}. To estimate the precise β_X output power of PV, it is required to evaluate it under real irradiance conditions [45]. Dash *et al.* have evaluated the β_X dependence on different irradiations levels for different PV modules' type. Their results elaborated the dependency of β_X on irradiance [46]. Makrdies *et al.* and Fanney *et al.* showed that the β_X vary with irradiation intensities specially at low levels [47], [48]. For CIGS solar cells, studies on the role of different solar cells layer configurations on the $\beta_{X,rel}$ has not been addressed in detail. This topic will be further discussed in Chapter 5.

1.1.3 Metastability studies overview

It is also known that temperature and illumination changes induce metastable changes in CIGS electrical performance. Such changes influence the certainty of the power estimates [49]. The illumination exposure time is an important factor to reach a stable condition before solar cells' actual characterization takes place [50]. For any change in the net doping density in the bulk or the junction of the absorber, a change in the defect distribution can be inferred [51]. Several models were proposed to explain the phenomena. One of the most extensive is the one proposed

by Lany and Zunger [52], where a complex defect forms consisting of Se and Cu vacancies (V_{Cu}-V_{Se}). This model implies that the metastable change depends on the charge state associated with the defects. The defect can transform from shallow donor to shallow acceptor by capturing two electrons. After electron-hole pairs generate upon light, the complex can then transform from shallow acceptor to deep acceptor after capturing another electron. This process depends on the temperature of the sample, as well as the position of Fermi level and the availability of electrons or holes being captured by the defect. Consequently, the net acceptor density can rise in the absorber. The known complex defects responsible of metastability effects can be enhanced by the layer structure of the solar cell. This will be further discussed in Chapter 6. A p^+ layer model is proposed describing the metastable defects to be accumulated in the CIGS front surface in acceptor configuration, creating a photo-barrier, this barrier height depends on the charge density. This model was justified by Lany and Zunger, and it describes the *FF* metastability in particular [53], [54]. Other model describing metastability effects is a defect center DX state that changes from shallow donor to deep neutral (or acceptor) depending on the occupation state, neighboring Cu vacancies, and the Fermi level. For more information about its dynamics, the reader can refer to [52], [55], [56].

Despite numerous research literature on CIGS solar cells' metastability, it is considered to be a puzzling phenomenon, because it can be attributed to multiple factors individually or together. Also, some defect types involved in this metastable behavior show very similar properties and energetical levels. Examples on those defects can be V_{Se}-V_{Cu} and DX complexes, which were mentioned before, and selenium vacancies (V_{Se}), referred in [57]. It was proposed that the V_{Se}-V_{Cu} defect is rather probable to exist in Cu poor material [51]. Nowadays, microscopically visualizing those defects in the laboratory is still a very challenging task. Particularly, when tracing the source location of this phenomenon as whether it is in the absorber bulk or in any of the interfaces [58]. Recently, it was even shown that the phenomena can be modeled by defects that are only present in the buffer layer [49]. Nevertheless, this study stated that a p^+ layer at CIGS surface, that has been proposed by another model, was not disproven nor corroborated. In this work, these inquiries will be assessed as a function of the layer structures of the used CIGS solar cells, especially regarding the metastable behavior of temperature coefficients, which have not been investigated deeply before.

1.1.4 Low light behavior overview

The light intensity influence on solar cell performance is of similar importance as the temperature effect. At a constant temperature, there is often a linear relation of the J_{sc}, photocurrent, and the maximum power versus the intensity of incident light on solar cells, while the logarithmic increase of V_{oc} is proportional to the intensity increase. The *FF*, the efficiency and the shunt resistance behave differently according to the illumination range provided. The series resistance is inversely proportional to the intensity [59]. The low light performance of photovoltaic devices also depends strongly on their shunt resistance [60].

Previous literature have showed the importance of the dominant recombination location on the solar cell's parameters and temperature coefficients [61], even though most of these studies were only limited to high illumination intensities. Moreover, Scheer *et al*. defined the activation energy (E_A) only for non-graded absorbers [62]. Furthermore, Kata *et al*., showed that the temperature sensitivity of solar cells can change under different illuminations conditions, and also according to the dominant recombination location [43]. Under low light conditions, solar cell parameters tend to deteriorate [63]. For CIGS solar cells, studies on the role of illumination intensities on the $\beta_{X,rel}$ for different solar cells layer configurations, are rather scarce. This point will be discussed in detail in Chapter 7.

Therefore, a deep understanding of the solar cell physics is necessary to improve their performance at different climate conditions, as well as for obtaining reliable results. Information about diverse losses could be obtained by different characterization techniques. In previous literature, losses reducing efficiency in solar cells could be mitigated by studying different fabrication parameters, for instance, thickness, post deposition treatments, and band gap profiles. To my knowledge, the study of CIGS solar cells temperature sensitivity relative to the cell structures' elemental layer composition has not been directly addressed in literature, particularly at low light conditions. Therefore, the aim of this work is studying the main physics governing the temperature sensitivity of different CIGS structures by applying different opto-electrical characterization techniques. Additionally, analysis of the metastability of temperature coefficients depending on the compositional layer modifications is also performed. Finally, investigation of the solar cell performance and temperature sensitivity under low light conditions was realized.

Chapter 2 CIGS solar cell layer structures

Ideally, the structure of a solar cell would consist of two electrodes and a *p-n* junction. Nevertheless, for CIGS solar cells, more material layers are incorporated between the absorber and the front contact. The most common CIGS solar cell layer arrangement consists of a back contact/CIGS absorber layer/buffer layer/*i*-layer/window layer configuration, as shown in Figure 1. Due to the different nature of each layer material, band discontinuities can emerge at the heterojunctions between each consecutive pair of layers. Therefore, a proper selection of these materials is essential to improve the characteristics of each junction. In the following, a description of each of the composing layers in a CIGS solar cell is presented.
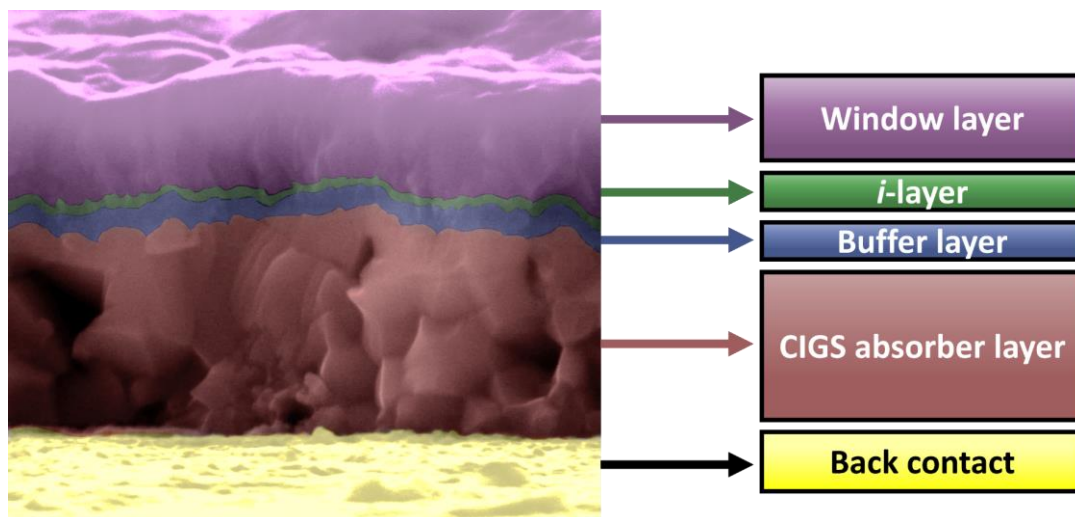
Figure 1: Layer structure of a CIGS solar cell.

2.1 Substrate

The substrate is used as a mechanical support for CIGS solar cells or modules. In the past, ceramic was used as the conventional substrate, but nowadays Soda lime glass (SLG) is typically used due to its adequate thermomechanical properties, its match in thermal expansion with CIGS [64], and cheaper cost. It also provides the beneficial effect of sodium diffusion into CIGS absorber during the deposition process of absorber [65]. This benefit is owed to the fact that Na reduces the impact of order vacancy compounds (2 V_{Cu}^{-} + In_{Cu}^{2+}) by occupying the Cu vacancies instead of In [66]. Apart, it was reported that the solar cells' parameters are improved when the substrate used is SLG, as it was suggested that the CIGS grew with a higher degree of orientation [67]. Nevertheless, Na diffusion from SLG cannot be properly controlled. To assess this issue, Si_xN_y barriers can be implemented over SLG to avoid diffusion of Na to the absorber. This way, Na diffusion through other means can be better controlled [68]. There are

also alternatives to SLG like polyimide and steel foil, which allows for lightweight modules or roll-to-roll deposition systems of flexible substrates [64], [69].

2.2 Back contact

The back contact serves as the collector of majority carriers that are generated in the p-side of the *p-n* junction. Molybdenum is used traditionally as a rear contact. It is deposited on SLG by direct current (DC) sputtering as it showed high conductivity and low cost of manufacturing [62]. Another advantage is that a $Mo(Se,S)_2$ layer tends to form in the interface between CIGS and Mo back contact during selenization process, as a result of chemical reaction between Mo and CIGS. This layer serves as an adhesion layer and it helps in decreasing the Schottky barrier effect through tunneling transport of holes [70]–[73]. If the $Mo(Se,S)_2$ layer is too thick then it becomes rather detrimental for the transport properties [74]. The $Mo(Se,S)_2$ layer's band gap and electron affinity match with CIGS layer's corresponding values. The features that are desired in a back contact are: no degradation during CIGS deposition, high conductivity, proper band alignment with CIGS to form an ohmic junction, good adhesion to glass [75], lattice match with CIGS and chemical stability to avoid undesired phases formation with the elements in CIGS [76]. It is also required that the back contact enable the diffusion of Na or K from the glass substrate to the absorber layer, which can be achieved during fabrication by decreasing the DC power used [77].

2.3 Absorber layer Cu (In,Ga) (S,Se)$_2$

The pentenary compound $Cu (In_{1-x},Ga_x) (S_y,Se_{1-y})_2$ absorber material used in the studied solar cells is a I-III-VI$_2$ semiconductor. It crystallizes in the ternary chalcopyrite structure, which can be represented as sphalerite structure (zinc blende) where the group II atoms (Zn or Fe in zinc blende) are replaced by group I (Cu) and group III (In, Ga) atoms. The crystal positions for group VI atoms are occupied by both S and Se, each of them tetrahedrally coordinated with atoms from groups I and III. A chalcopyrite unit cell is shown in Figure 2.
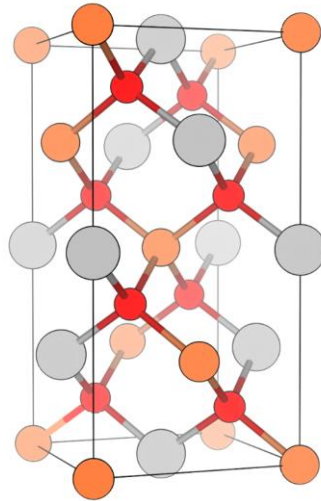
Figure 2: CIGS unit cell. Orange: Cu positions. Grey: In/Ga positions. Red: S/Se positions (drawn with VESTA software).

One of the main advantages of using a thin film absorber in PV is their direct band gap, as it presents a larger absorption coefficient than an indirect band gap absorber. Due to this improved optoelectronic property, the absorber's thickness can be in the order of the carrier's diffusion length. Consequently, less raw material is used during fabrication, as well as a lower cost is involved. These characteristics give thin film solar cells an advantage over Si solar cells, which, due to their indirect absorber band gap nature, require larger absorber thickness in range of hundreds of micrometers to achieve adequate optical absorption. Therefore, a larger diffusion length and higher purity material is needed for proper carrier extraction [78].

Shockley and Queisser showed in their investigation, that the maximum achievable conversion efficiency for a single *p-n* junction solar cell could be reached with an absorber with a band gap between 1.1-1.5 eV [79]. Among the available thin film absorber materials, CIGS stands out for its tunable band gap in the range between 1.0 eV and 2.43 eV [80], which makes it an ideal candidate for achieving high efficiency thin film solar cells. It is known that the macroscopic ratios of GGI and SSSe affect multiple CIGS parameters, like band energy positions or electron affinity values. This opens the possibility to grade the band gap and electron affinity of the absorber. CIGS chemical grading depth profile manufactured by stacked elemental layer has been studied before [42]. The study showed the advantages of incorporating double grading profiles in the absorber layer on the efficiency of solar cells, being the first grading towards the absorber's back side from Ga-rich phases, which establish a back-surface field for the minority carriers that leads to diminish back interface recombination velocity [42], and the second grading profile with S replacing Se in the heterojunction region, which helps to reduce interface recombination due to the increment of band gap energy in the front of the absorber.

2.3.1 Thickness variation

One of the key parameters behind the improvement of solar cell performance is the optimization of the absorber thickness, as it has been established to be beneficial for mass and speed of solar cells production, as well as for cost reduction. Therefore, during last decades the focus towards the production of thinner absorbers was highly remarkable [68], [81], [82]. Several numerical and experimental investigations have been performed for optimizing the absorber' thickness [83]–[86]. CIGS thickness is typically in the range between 1-2 µm. However, for cheaper industrial mass fabrication, there is a great heading towards thinner CIGS absorbers. Park *et al*. have achieved 22.6% record efficiency with an absorber thickness of less than 1 µm [87]. An efficiency of 21.4% was previously achieved by Mostefaoui *et al*. with absorber thickness 1.5 µm [88]. Absorbers with 0.5 µm thickness have already reached efficiencies of 10.3% without anti reflection coating or light trapping through surface texturing [83], [89] and with little or almost no reduction in *FF* and V_{oc}, whereas the J_{sc} always showed a significant reduction in cells with thin absorber down to 0.5 µm due to the reduced absorption. The aid of MgF_2 reflective layer helped to reach an efficiency of 25% for 1 µm absorber. The application of ultrathin absorbers is vastly involved in tandem cell devices [81]. Recently, for improving light trapping in the absorber, nanostructured back mirror such as Ag, Cu and Au was used instead of Mo back contact. Using Ag nanostructured back mirror, a high J_{sc} (35.02 mA/cm^2) is obtained for 0.5 µm -thick cells and an efficiency of 21.74% [85].

2.3.2 Band gap grading

Band gap grading is the process of varying Ga/(Ga+In) (GGI) ratio and/or S/(S+Se) (SSSe) through a depth profile to tune the absorber band gap. It is well known that grading the band gap of a solar cell is decisive for highly efficient solar cells. Double graded band gap (front and back) of the absorber is employed by varying the GGI and SSSe ratios. The absorber GGI back grading enhance the back surface field and hence enhance carrier collection [90]. It has been concluded before that the back grading will not have a significant influence on thick absorbers, where most of the carrier generation occur far from the back contact [91]. Front absorber SSSe grading is aimed to increase the band gap in the space charge region (SCR), to avoid recombination and to increase V_{oc} [92].

Several simulation studies [93], [94], have been applied to investigate the impact of GGI and SSSe on solar cell performance. Some conclusions have been drawn regarding the role of Ga and S in increasing the band gap. It has been reported that GGI mainly shifts up the conduction

band by 90% of the band gap increment, while the valence band is shifted down by the remaining 10%. SSSe grading, on the other hand, shifts the conduction band up and the valence band down in a proportion of 40% and 60% of the band gap increase, respectively. It has also been shown that increased GGI leads to smaller grain sizes [95]. Additionally, the efficiency can increase considerably if the absorber band-gap is around 1.48 eV, which properly matches the solar spectrum and yields efficiencies of about 22.95% [93]. The influence of a linear Ga profile on the temperature behavior of solar cells have been studied [42].

2.3.3 Post deposition treatment

Post deposition treatment (PDT) of the absorber surface by heavy (Cs [96], Rb, K [16]), and light alkali metals (Li, and Na [97]–[99]) was introduced in 2013. Heavy alkali materials showed to be quite beneficial for the improvement of solar cells' electrical parameters and led to a great achievement in boosting the device efficiency. This was attributed to a reduced band bending at grain boundaries, which reduces tail states and nonradiative recombination [100], minimizing conversion losses.

2.4 Buffer layer

The buffer layer is an intermediate layer between absorber and window layers that forms the *p-n* heterojunction with the absorber, aiming for electrical conduction, transmission of photons, and enhancement of the lattice mismatch between the neighboring layers. This layer also provides stability to the device, and establish the electrostatic conditions inside the absorber film for the photovoltaic conversion [101].

Conventionally, CdS has been used as the buffer material with a fixed band gap, as it showed a good performance and high efficiency. In the last decade the use of Cd- free buffer materials like $Zn(O, S)$, In_xS_y or SnS_2 were intended to avoid toxic waste. The $Zn(O, S)$ has been previously used as a buffer layer due to its higher transmission and better collection of short-wavelength photons compared to CdS [102]. Its band gap can be tuned to optimize the buffer/absorber interface barrier for better transport properties and band alignment [103], [104]. Increasing carrier concentration, and optimizing the oxygen amount of $Zn(O, S)$ can control the properties of conduction band offset (CBO) barrier which then reflects on the improvement of *FF* parameter [105].

The In_xS_y buffer doped with Na has been used due to its promising characteristics on achieving comparable efficiencies of 16.4% [106]. In addition, elemental diffusion to In_xS_y buffer could

be beneficial or detrimental depending on the segregated element. For example, Cu diffusion from CIGS to In_xS_y is known to degrade the electrical conductivity, and reduce the band gap of the In_xS_y buffer [107]. On the other hand, Na diffusion from soda lime glass substrate to In_xS_y buffer layer showed an increase in its band gap [108], [109].

2.5 Intrinsic (*i*)- layer

This layer is commonly implemented to prevent damage to the absorber and buffer layers during the deposition of the front contact. Another purpose is to avoid current leakage through shunts due to its high resistivity. It has been reported that the implementation of intrinsic (*i*)-layer between the buffer and front contact is difficult to characterize, as it could be controlled by other process variables, some reported that omitting *i*-layer results in the reduction of V_{oc} [110], hence reduction in the efficiency. Other reported no significance influence on the V_{oc} unless the *i*-layer thickness is above 100 nm [111]. Often, *i*-ZnO is used as it showed to reduce the influence of shunts and the current leakage [111]–[113], although production with RF sputtering is costly. Another common alternative candidate that can be used is (Zn, Mg)O, it has a 3.3 eV band gap, which is wider band gap than *i*-ZnO (3.2 eV) and can reduce the losses due to parasitic absorption [113].

2.6 Window layer

The solar cell structure is terminated by the window layer. It is used to minimize the surface recombination velocity by reducing density of defects on the surface [105], [114], and to transport the current to an external circuit. The uncommonly achieved simultaneous characteristics of this layer is the coexistence of high electrical conductivity and optical transparency due to the reason that conductivity is proportional to mobility that can lead to free carrier absorption as a result of high charge density [115]. The most used front contacts are transparent conductive oxides (TCO) like Aluminum (Al)-doped ZnO with a band gap of 3.2 eV [62] or indium-tin oxide (ITO) [116].

Chapter 3 Physical Background

3.1 Semiconductor physics

Semiconductors are materials that need an external energy equal or greater than its band gap to start conducting electricity. Their conductivity properties are classified to be in between insulator and conductor. They are the building block of electronic devices such as light emitting diodes, transistors, cameras, lasers, detectors, solar cells, etc.

The main difference between different materials' properties lies in their band gap values and crystal structures, which results from the diverse arrangement of atoms and elemental composition, that all reflect on the material optical properties and are governed by the band structure. For instance, metals have no bandgap, while for energy gap larger than 3 eV materials are often considered as insulators [117].

A semiconductor can absorb a photon if its energy is greater than or equal to the bandgap. When this occurs, an electron with $-q$ charge can be excited from valence band to move freely in the conduction band. The electron leaves a vacancy in the valence band with an opposite charge $+q$ called a hole. This behaves as a quasi-particle that can be re-occupied by another electron either from a neighboring atom or due to recombination process.

3.1.1 Effects of temperature on semiconductors

At 0 K temperature, all electrons in a semiconductor are bonded tightly by their atoms and the valence band is thereby filled completely with electrons, whereas the conduction band is entirely empty. At this temperature, semiconductor will act as insulator, unless enough external energy, i.e. heat, is supplied to the semiconductor. Only then electrons can be excited to the conduction band and become free. At room temperature, a considerable number of electrons will be indeed excited from the highest occupied level in the valence band to the lowest unoccupied level in the conduction band. Therefore, it exhibits weak conductivity. Raising the temperature further will lead to a reduction in the bandgap energy of a semiconductor, this is ascribed to the larger interatomic spacing resulting from the increment of atomic vibrations due to rise of thermal energy by the intense thermal motion at high temperature. Since electrons must be excited by the energy difference between the conduction and valence band to be free [118], at higher T this energy will be easier to gain because the band gap shrinks. The bandgap energy as well as doping determine the electrical conductivity of semiconductor devices [119].

Chapter 3 Physical Background

A semi-empirical relation for the semiconductor bandgap variation with temperature was proposed by Varshni [120]

$$E_g(T) = E_{g0} - \frac{\alpha T^2}{\beta + T} \qquad (3.1)$$

where E_{g0} represents the bandgap of the material at 0 K, α and β are fitting parameters of the equation. The carrier density in the conduction band depends strongly on temperature and the band gap of the semiconductor. Under thermal equilibrium the intrinsic carrier concentration is given by equation (3.2)

$$n_i^2 = N_c N_v * e^{-\frac{E_g}{kT}} \qquad (3.2)$$

with $N_{c/v} = 2\left(\frac{2\pi m_{e/h}^* kT}{h^2}\right)^{\frac{3}{2}}$ as the effective densities of states in the conduction and valence band, respectively, k is the Boltzmann constant, m_e^* and m_h^* are the corresponding effective masses of electrons and holes. Some studies revealed that those effective masses are temperature dependent [121]. The carrier concentration and their mobility are temperature dependent.

Different intervals of temperature impact discernibly the free carrier concentration in a semiconductor. At temperatures below 100 K, the acceptors and donor's dopant atoms do not have enough thermal energy to be fully ionized, this region is called the freeze-out or incomplete ionization regime. This is only true for a low doped non-degenerate semiconductor, where the occupation probability of states is determined by Fermi-Dirac distribution function

$$f(E) = \frac{1}{e^{\left(\frac{E-E_F}{kT}\right)} + 1} \qquad (3.3)$$

At 0 K, for energy levels located below the Fermi level (E_F), the probability of occupation would be 100%. Therefore, the valence band would be fully occupied by electrons. The contrary applies for energy levels above the E_F, in the conduction band, the probability of an electron to occupy an energy level there is 0. At any temperature, the electron has a 50% probability to occupy a state with energy equal to the Fermi level energy.

For a degenerate semiconductor, the Fermi level is inside the energy band level, not in the bandgap as is the case for a non-degenerate semiconductor. Depending on the type of dopants the Fermi level can then be inside the conduction band for *n* type, or inside the valence band for *p* type. Therefore, the semiconductor behaves in intermediate manner between a

semiconductor and a metal, because still the semiconductor has significantly less charge carriers than a metal. The fact that the Fermi level lies in the conduction band is owed to the merged levels of impurity atoms in close proximity. The interference of the impurities leads to the transformation from discrete energy levels to an energy band, which cancel the freeze out effect. At high doping density, the resulting broadening growth of the impurity's bands would add a downwards or upwards shift towards the free main bands. At this point, there is no longer tangible cut between the free bands and the localized defects bands. Subsequently, the conductivity in a degenerate semiconductor is high at all temperatures and the freeze-out effect is not considered. Therefore, the type of semiconductor plays an important role in the conductivity's temperature dependence.

When the temperature range is higher than or equal to 100 K and less than 500 K, the semiconductor is in the so-called extrinsic regime. Surely, at this temperature most of the donors/acceptors have been already ionized and carriers can move freely in the corresponding bands. This region is also called saturation region where the density of dopants is similar as the density of ionized impurities, whereas for temperatures higher than 500 K the intrinsic carrier concentration exceeds the dopants concentration.

The carrier mobility is an important parameter that describes the speed of carriers under an applied electric field, it indicates the performance of different semiconductor devices and hence the suitability for its applications. The mobility of a semiconductor is not only dependent on the applied electric field but also on the temperature. There are two types of scattering that influence the mobility significantly. The first type is scattering by lattice waves; it is a result of the increase in number of phonons with temperature. Consequently, the scattering time will decrease and thus the mobility decreases with higher temperature. The other scattering type is caused by the ionized impurities. It is created due to the electrostatic force between the ionized impurities and the carriers. Here, it also depends on the density of ionized impurities, which can enhance the scattering and thereby lower the mobility. Their effect is explained by the carriers' thermal velocity: the higher the velocity the lower the interaction time with impurities it becomes. In turn, the scattering is reduced and the mobility increases.

It is worth noting that the difference between a compensated and uncompensated semiconductor would also affect the mobility individually. For the case where there is an equal concentration of shallow donors and shallow acceptors in a compensated semiconductor, the shallow acceptor would capture the ionized donor's electron instead of producing this electron to be free in the conduction band. This would ionize the existing shallow acceptor simultaneous to the ionization

of shallow donor. The resultant is a larger number of charged impurities, which as explained before, will reduce the mobility. Therefore, the mobility in an uncompensated semiconductor is higher than in a compensated semiconductor. Additionally, in an uncompensated semiconductor the mobility is temperature dependent because the change in shallow defects density with temperature will also reflect on scattering. On the other hand, for a compensated semiconductor where the opposite ionized charges of equal amount for both shallow defects will lead to neutral net charge that will not induce an electrostatic scattering force. Thus, the temperature dependence of mobility based on dopants scattering is strongly dependent whether it is a compensated or uncompensated semiconductor. In overall, the mobility changes with temperature in such way that the dominant mechanism would control its behavior. The resultant mobility is then a balance between the two counteracting mechanisms [122].

3.1.2 Recombination

The radiative recombination determines the solar cell open circuit voltage and hence it can give an estimation about the maximum reachable conversion efficiency. Non-radiative recombination, on the other hand, is considered as a non-desired process that deteriorates the solar cell efficiency. In CIGS particularly, losses via recombination centers dominate the recombination processes, which have led to device efficiencies of around 20% [123]. The recombination depends strongly on the diffusion length of carriers. It is described as the average distance that carriers can travel before recombining. Likewise, the carrier's lifetime is expressed by the average time taken to cover this distance. Since the mobility (μ) is related to the diffusion length (L) through Einstein relation as $L = \sqrt{\frac{\tau_0 \mu k T}{q}}$, where τ_0 is the minority carrier lifetime, the diffusion length is also temperature dependent.

The recombination mechanisms that can take place in semiconductors are, (i) band to band recombination (radiative), (ii) Shockley, Read and Hall (SRH) trap assisted recombination (non-radiative) and (iii) Auger recombination (non-radiative) and (iv) Surface recombination (non-radiative). These can be visualized in Figure 3. The first mechanism emits the energy of a recombined electron in form of a photon, that is why it is called radiative recombination. This mechanism in direct band gap semiconductors like CIGS emits all the energy in the form of photons. The second mechanism releases the recombination's energy in form of phonons that are responsible of increasing the device's absorber temperature. For Auger recombination, the excess energy of recombination is transferred to another carrier in form of kinetic energy that serves as an accelerator for a third carrier, thus it thermalizes and emits phonons as well. Lastly,

Surface recombination can occur at the boundaries of the semiconductor, where atoms have dangling bonds due to missing bonding partners. These dangling bonds are very abundant and act as defect states through which minority carriers can recombine. It must be noted that even for high quality absorbers like in monocrystalline Si solar cells, the Auger recombination as well as surface recombination govern the electrical properties [76].
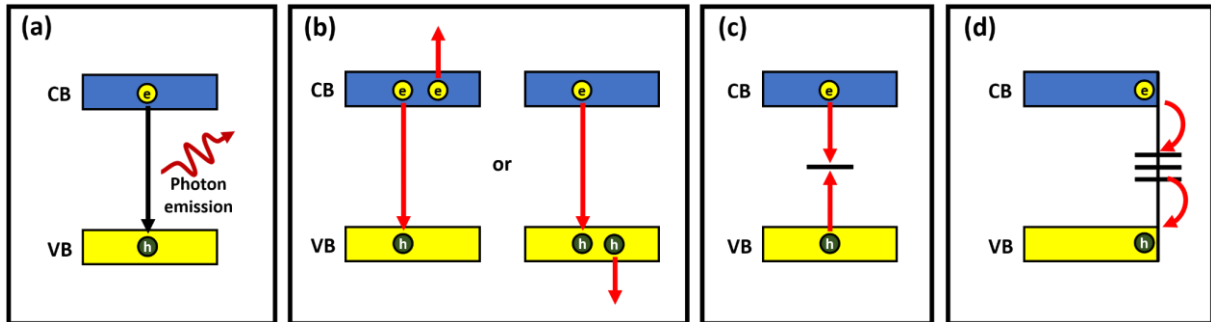
Figure 3: Recombination mechanisms present in semiconductors. (a) Band to band recombination, (b) Auger recombination, (c) Shockley, Read Hall recombination, and (d) Surface recombination.

3.1.3 Working principle of solar cells

In dark conditions, when a *p*-doped semiconductor and *n*-doped semiconductor get in contact, the difference in chemical potential due to the difference in carrier concentration will drive a diffusion current. This current is a result of majority charge carrier's diffusion in both types of semiconductors in opposite directions. Due to diffusion of electrons from *n* type side to the *p* type side, an accumulation of static positive charge in the *n* type side will be present. As well, the *p* type side will accumulate a static negative charge. The vicinity of the junction will be depleted from charge carriers. This region is known as the space charge region. Due to the difference in static charges between the two sides, an electric field will be induced inside the SCR, whereas the regions outside the depletion region where the electric field is almost zero are referred as quasi neutral regions. This electric field will push electrons in a direction opposite to diffusion current, from *p* side to the *n* side. This current is called drift current or minority carriers current, which counteracts the diffusion current in the opposite direction. This process will equilibrate at some point (the diffusion current is counterbalanced with the drift current). This state of the *p n* junction is called thermal equilibrium condition. At this condition, the Fermi level is completely flat through the whole device (Figure 4a).
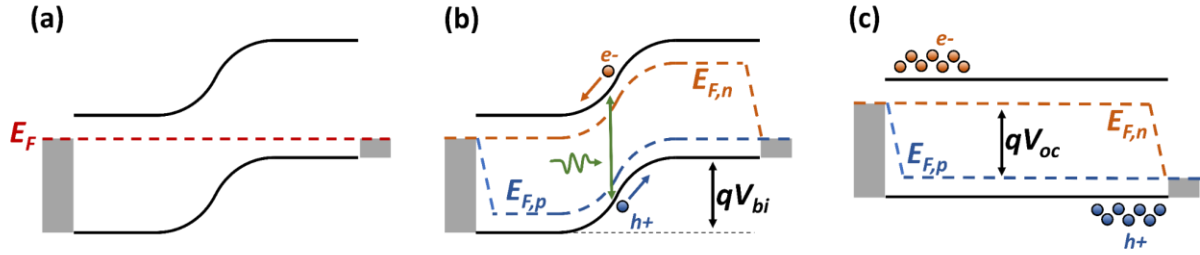
Figure 4: Simplified band diagram of a p-n junction (a) at dark, (b) at short circuit conditions, and (c) at open circuit conditions.

Under illumination conditions, this equilibrium condition is disrupted, and the Fermi level will split due to the generation of electrons in the *p* side, similarly for holes in *n* side. Therefore, each carrier type concentration will no longer be described by a single Fermi level as in thermal equilibrium. Instead, a quasi-Fermi level is employed to describe the carrier statistics for each energy band as

$$n = N_c * e^{-\left(\frac{E_c - E_{F,n}}{kT}\right)} \tag{3.4}$$

$$p = N_v * e^{-\left(\frac{E_{F,p} - E_v}{kT}\right)} \tag{3.5}$$

The *p* and *n* product therefore is

$$pn = n_i^2 * e^{\frac{E_{F,n} - E_{F,p}}{kT}} \tag{3.6}$$

After the generation of electrons in the *p* side, if the electron has a sufficient diffusion length to reach the SCR, it will be driven by the electric field towards the *n* side, and similarly holes generated in the *n* side will be drifted to the *p* side. Consequently, a gradient in electrochemical potential at both *p* and *n* terminals will be induced due to the opposite charge accumulation in both semiconductors.

In open circuit conditions, the voltage obtained from this gradient in chemical potential is the maximum voltage that a solar cell can provide when there is no more current flow (Figure 4c). If the circuit is not open and is connected with a wire with no load, this current generated will recombine through the external circuit and no electrochemical potential is present. This state is called short circuit condition, where the maximum current of the cell is measured at zero voltage (Figure 4b). If the cell is connected to an external load, the separation of charge by the electric field will contribute to the current, here the role of the back and front metal contact come into play to extract different carriers correspondingly. Holes extracted from the back contact and electrons from the front contact, resulting in a net flow of current in the external load. Hence, the load is fed and can generate power under illumination.

3.2 Diode models and solar cell equivalent circuits

The dark JV characteristics of a solar cell are typically described with the ideal diode model, expressed as

$$J(V) = J_{0,1}(e^{\frac{qV}{kT}} - 1) \tag{3.7}$$

where q is the elemental charge, V is the applied voltage and J_0 is referred as the diffusive dark saturation current, which is expressed as

$$J_{0,1} = q \left(\frac{D_e}{L_e N_A} + \frac{D_h}{L_h N_D} \right) n_i^2 \tag{3.8}$$

where D_e and D_h are the electron and hole diffusion constants, respectively, L_e and L_h are the mean diffusion lengths for electrons and holes, respectively, N_A is the acceptor density, and N_D is the donor density. This model assumes that the space-charge region is sharply separated from the quasi-neutral region, as well as neglecting the current contribution from carriers generated in the SCR. Only carries diffusing from the quasi-neutral region are considered to contribute to the current.

Under illumination conditions, the ideal one diode model reads

$$J(V) = J_{diode,1}(V) - J_{ph} = J_{0,1} \left(e^{\frac{qV}{kT}} - 1 \right) - J_{ph} \tag{3.9}$$

where J_{ph} is the photogenerated current. An equivalent circuit of an ideal solar cell is shown in Figure 5.
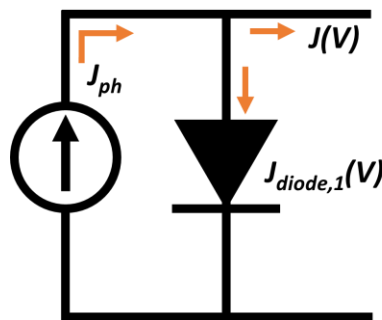
Figure 5: Equivalent circuit for an ideal single junction solar cell

At low light intensities, the dark saturation current density can be dominated by recombination in the SCR. In this case, the dark saturation current density can be expressed as [124]

$$J_{0,2} = \frac{n_i W_{SCR} kT}{2(V_{bi} - V)\tau_0} \tag{3.10}$$

where τ_0 is the carrier lifetime, V_{bi} is the built- in voltage, and W_{SCR} is the SCR width. The diode equation under illumination conditions would then read

$$J(V) = J_{0,2} \left(e^{\frac{qV}{2kT}} - 1 \right) - J_{ph} \qquad (3.11)$$

In a solar cell where both bulk and SCR recombination mechanisms can be present at the same time. Then, the expression for the current of the illuminated solar cell would be

$$J(V) = J_{0,1} \left(e^{\frac{qV}{kT}} - 1 \right) + J_{0,2} \left(e^{\frac{qV}{2kT}} - 1 \right) - J_{ph} \qquad (3.12)$$

This can be represented as two diodes in parallel with a current source, as seen in Figure 6.
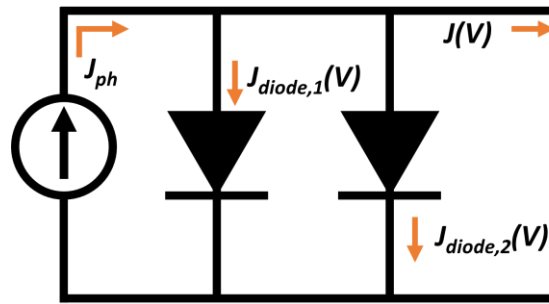
Figure 6: Equivalent circuit for a single junction solar cell with two recombination mechanisms.

This model is commonly expressed as a single diode with an added factor in the exponential term as

$$J(V) = J_0 \left(e^{\frac{qV}{mkT}} - 1 \right) - J_{ph} \qquad (3.13)$$

This model is insufficient for less efficient cells, where multiple recombination mechanisms and the effects of parasitic series and shunt resistances are relevant. In this case, a more realistic diode model can be represented as

$$J(V) = J_0 \left(e^{\frac{q(V - JR_s)}{mkT}} - 1 \right) + \frac{q(V - JR_s)}{R_{sh}} - J_{ph} \qquad (3.14)$$

where R_s and R_{sh} are the series and shunt resistances, respectively. The parameter m is referred as the "ideality factor". It can have values between 1 and 2, as well as it can provide information of the dominant recombination mechanism present in the solar cell: $m=1$ is observed for recombination occurring in the quasi-neutral region or the interface of the p-n junction, while $m=2$ indicates a dominant recombination in the space-charge region. Values in between are indication of a mixture of the recombination mechanisms mentioned previously. J_0 is given by

$$J_0 = J_{00} e^{-\frac{E_A}{mkT}} \qquad (3.15)$$

with activation energy E_A, and a prefactor J_{00} dependent on the recombination mechanism dominating J_0 [62]. The equivalent circuit is shown in Figure 7.
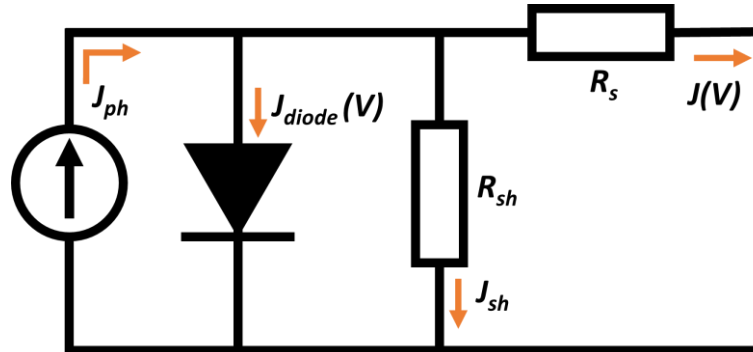
Figure 7: Equivalent circuit for a non-ideal solar cell, where effects of shunt and series resistances are present.

An example of dark and an illuminated JV curves are shown in Figure 8a. It is known that in CIGS solar cells, the superposition principle does not hold, and the dark and illuminated JV curves often cross together, which happens when the photocurrent is voltage dependent. A detailed explanation on the superposition failure can be found in reference [125].

Another common artifact seen on CIGS JV curves, is the so-called rollover effect, which consists of an increase of resistance at forward bias larger than V_{oc}. This happens due to the presence of transport barriers for majority carriers. This effect becomes more evident at low temperatures, where the thermionic emission current cannot overcome the interface potentials between layers in the cell's structure (see Figure 8b).

The red kink or double diode effect is also a commonly observed effect on IV curves of CIGS solar cells when illuminated with high wavelength light (as seen in Figure 8b). Under such illumination conditions, photons can only be absorbed in the absorber layer. If a high barrier at the buffer/absorber interface is present, minority carriers will not be efficiently collected under forward bias conditions. This is evident in generally low *FF* values. Another cause of this effect is due to the presence of a p^+ layer in the front near-interface region of the absorber, where the accumulation of a large density of negative charge leads to the formation of a conduction band barrier in this region of the absorber, which consequently, also affects the carrier collection efficiency.
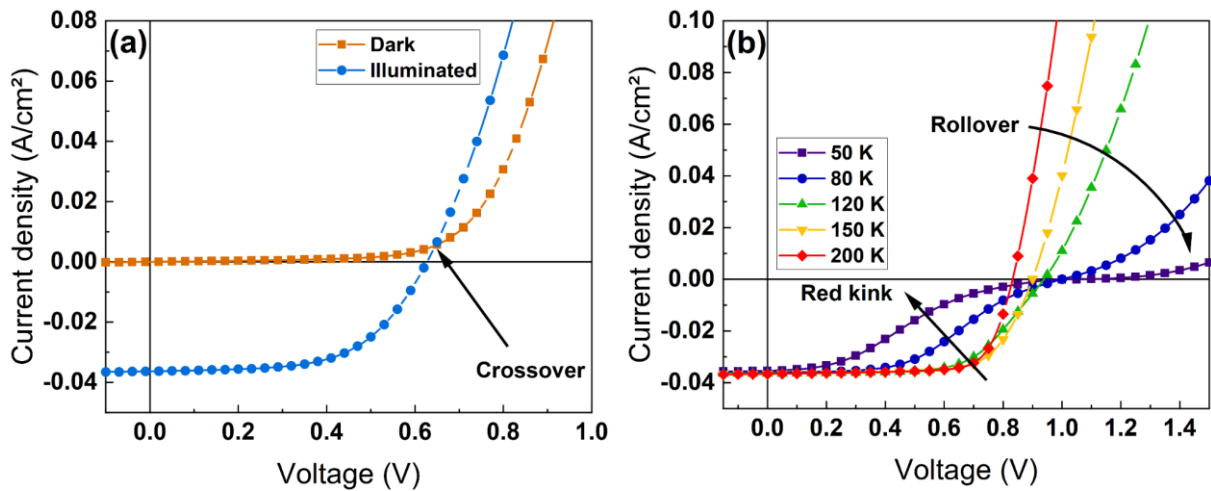
Figure 8: (a) Dark and illuminated JV curves of a CIGS sample, showing a crossover effect. (b) JV curves of a CIGS sample at different temperatures, where the effects of a red kink and the rollover of the curves are present.

3.3 Efficiency losses

In principle, a solar cell can be described as an energy converter of the sun´s thermal energy and transform it into electrical energy. Therefore, as any heat engine, it is subject and limited by the laws of Thermodynamics. Nevertheless, it differs from a Carnot engine in the sense that the incoming energy from the sun is through photons and not heat.

In a single junction solar cell, efficiency conversion losses can be categorized in extrinsic and intrinsic loses. Extrinsic losses include series/shunt resistances, parasitic recombination, and grid shadowing, just to name a few. In theory, these could be avoided by improving the fabrication approaches. Intrinsic losses, on the other hand, cannot be avoided even in an idealized solar cell. Five types of intrinsic losses can be considered: **(1)** Incoming photons with energy smaller than the energy band gap of the solar cell will not be absorbed, and therefore will not contribute to the generation of carriers ($< E_g$ loss). **(2)** For absorbed photons with energies larger than E_g, a further loss is observed in the form of thermalization of excited carriers, where their excess of energy is transmitted to the crystal lattice in the form of phonons (thermalization loss). **(3)** According to Kirchhoff's law, any light absorber semiconductor also behaves as a light emitter. As voltage is built in the solar cell, this expected emission rate is increased, resulting in energy lost in the form of photon emission (emission loss). **(4)** According to the second law of thermodynamics, any engine that converts energy into work (or into another type of energy), requires to lose some of the input energy in the form of heat. For a solar cell, this is seen as a voltage loss during carrier separation (Carnot loss). **(5)** Finally, another energy loss is present due to the angle mismatch between absorption and emission of

photons in the solar cell, resulting in an increase of entropy due to the increased number of photon modes (Boltzmann loss). In Figure 9, these losses are represented in a solar cell band diagram. There, it is possible to differentiate the impact of each loss either on the current or the voltage of the cell.
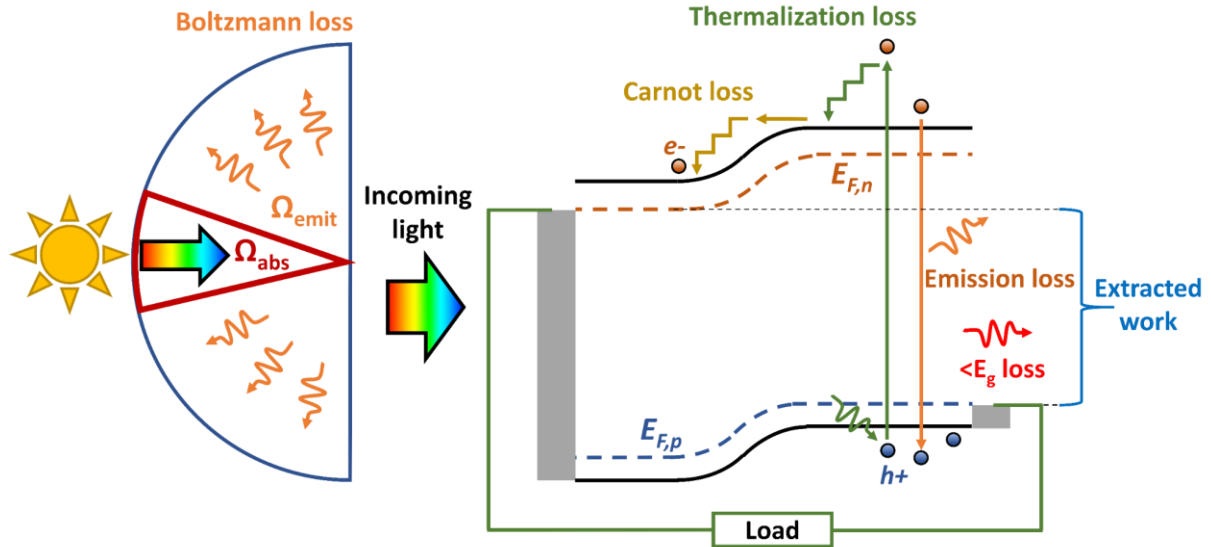
Figure 9: Intrinsic loss mechanisms present in a single junction solar cell.

As described above, a solar cell can be considered an energy converter device, where the energy source is the sun. Here, the sun can be modelled as a blackbody, emitting its characteristic ~6000 K spectrum. Due to the large distance between the sun and the earth, the solid angle of absorption of the solar cell will be very small. Furthermore, as a voltage is built in the solar cell, its light emission will increase, but with a larger solid angle. Both light absorption and emission on the solar cell can be described by the total photon emission flux $n(E, T_{em}, \mu, \Omega)$ with the generalized Planck equation

$$n(E, T_{em}, \mu, \Omega) = \frac{2\Omega}{c^2 h^3} \frac{E^2}{e^{\frac{E-\mu}{kT_{em}}} - 1} \qquad (3.16)$$

where E is the photon energy, T_{em} is the emitting body's temperature, c is the speed of light in vacuum, h is Planck's constant, Ω is the solid angle, and μ is the chemical potential of the source.

From a detailed balance perspective, under optimum power generation conditions, assuming transmission of all photons with sub bandgap energies, and no other parasitic recombination losses, the generated photocurrent in a solar cell can be expressed as the difference between the absorbed and emitted photons [126]

$$J_{mpp} = q \int_{E_g}^{\infty} n_{abs}(E, T_{sun}, 0, \Omega_{abs}) dE - q \int_{E_g}^{\infty} n_{emit}(E, T, V_{mpp}, \Omega_{emit}) dE \qquad (3.17)$$

where Ω_{abs} and Ω_{emit} are the solid angles of absorption and emission, respectively. T_{sun} and T are the temperatures of the sun and the solar cell, respectively. $\mu_{cell}=V_{mpp}$ is the voltage of the cell under maximum power conditions. For the sun, $\mu_{sun}=0$ as it is modelled as a blackbody. Ultimately, J_{mpp} ends up being a function of E_g and V.

The efficiency η of the solar cell is calculated as

$$\eta = \frac{P_{mpp}}{P_{in}} = \frac{J_{mpp} V_{mpp}}{P_{in}} \qquad (3.18)$$

with P_{in} being the total incident light power. J_{mpp} is a function of E_g and V, both being independent variables. Therefore, there is an ideal efficiency reachable under optimized E_g and V, that can be found by solving two partial differential equations:

$$\left(\frac{\partial \eta}{\partial V} \right)_{E_g} = 0 \qquad (3.19)$$

$$\left(\frac{\partial \eta}{\partial E_g} \right)_V = 0 \qquad (3.20)$$

The first condition gives information about the ideal E_g in a solar cell. The second condition can be solved analytically by using the Boltzmann approximation in the denominator of Planck's generalized equation, yielding [127]

$$qV_{mpp} = E_g \left(1 - \frac{T}{T_{sun}} \right) - kT \ln \left(\frac{\Omega_{emit}}{\Omega_{abs}} \right) \qquad (3.21)$$

This relation gives two of the intrinsic voltage losses present in a solar cell. The first term in the right side of the equation refers to the Carnot loss due to energy transformation, while the second term refers to the Boltzmann loss due to different angles of incoming and emitting light on the cell [127].

Table 1 shows an overview of all five intrinsic energy losses in a single junction solar cell. There, it is evident that only the losses coming from the detailed balance analysis (3-5) are sensible to T, where increasing cell temperatures generate larger losses. This is the fundamental reason of why solar cells become less efficient as their temperature increases. Furthermore, Carnot and Boltzmann losses increase linearly with temperature. In fact, also Emission losses vary approximately linearly with temperature, if while solving its integral using Boltzmann's

approximation, neglecting the -1 in the denominator and simplifying depreciable terms during integration by parts [38], results in

$$Emission\ loss \approx T\left(\frac{2\Omega_{emit}}{c^2h^3}k\ E_g^3\ e^{-\frac{E_g}{kT_{sun}}-\ln\left(\frac{\Omega_{emit}}{\Omega_{abs}}\right)}\right) \qquad (3.22)$$

being clearly linear with *T*. This explains why solar cell efficiency decreases linearly with temperature, on the temperature range of common operation.

Table 1. Mathematical description of intrinsic energy losses in a single junction solar cell.

(1)	$<E_g$ loss	$\frac{2\Omega_{abs}}{c^2h^3}\int_0^{E_g}\frac{E^2}{e^{\frac{E}{kT_{sun}}}-1}E\ dE$
(2)	Thermalization loss	$\frac{2\Omega_{abs}}{c^2h^3}\int_{E_g}^{\infty}\frac{E^2}{e^{\frac{E}{kT_{sun}}}-1}(E-E_g)\ dE$
(3)	Emission loss	$\frac{2\Omega_{emit}}{c^2h^3}E_g\int_{E_g}^{\infty}\frac{E^2}{e^{\frac{E-qV_{mpp}}{kT}}-1}\ dE$
(4)	Carnot loss	$E_g\left(\frac{T}{T_{sun}}\right)J_{mpp}$
(5)	Boltzmann loss	$kT\ln\left(\frac{\Omega_{emit}}{\Omega_{abs}}\right)J_{mpp}$

3.4 Metastabilities in CIGS

3.4.1 Light soaking

The photovoltaic device performance exhibit alteration during illumination, such as reversible metastability. The magnitude of these light induced effects depends on the device technology [50], for instance multijunction solar cells have less sensitivity towards light induced changes than single junction devices. Therefore, it is necessary to characterize devices under short, and long-term light exposure to have an adequate performance characterization and that is known as light soaking (LS). Apart, from IV curve stabilization, it is known to improve the performance of some solar cells depending on the fabrication and structures [128]–[130], it is commonly observed that p-doping increases in CIGS absorbers upon LS [131], thereby, its carrier concentrations also change and results in V_{oc} change. In CIGS modules, it has been reported that the metastability occurred due to light exposure results from the charging and

discharging of defects in the buffer absorber interface, additionally, due to the persistent photoconductivity effect in the bulk [132].

3.4.2 Buffer photoconductivity effect

The photoconductivity effect in thin film solar cells results from the buffer layer, when it is compensated by mid gap trap states and generated electron-hole pairs are involved in secondary effects. Under illumination, the buffer free minority carrier concentration increase based on the change of trap occupation, and the *n*-type conductivity increase under blue light illumination. Consequently, the Fermi level in the buffer shifts closer to the conduction band, which will reduce the barrier in the buffer/absorber interface. This will cause the carrier collection to increase significantly [133].
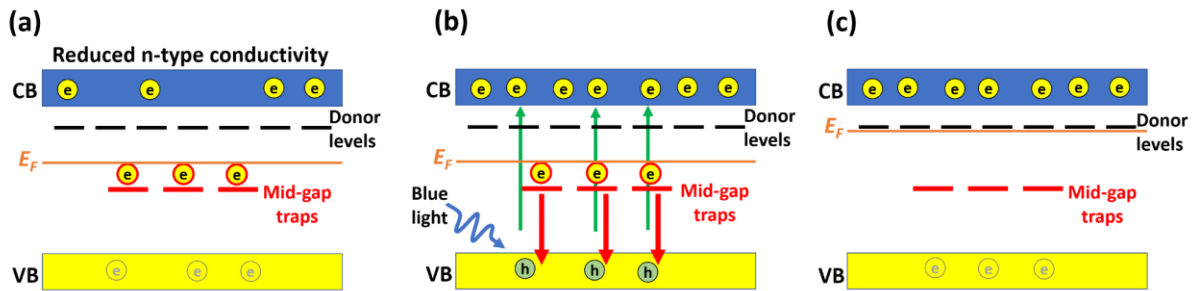
Figure 10: Buffer photoconductivity mechanism activated with blue light. (a) Buffer with reduced donor concentration due to trapped electron in deep traps. (b) hole-electron pairs generated due to blue light absorption, where trapped electrons recombine with photogenerated holes. (c) Overall resulting in the recovery of the donor concentration and consequent raise of the Fermi level, leading to an improved built-in electric field in the p-n junction.

Chapter 4 Experimental and characterization techniques

In this section, an overview on optical and electrical characterization techniques and methods specified for extracting physical parameters will be introduced briefly. The main aim of characterization methods is to determine the loss mechanisms in solar cells along with the influence of modified fabrication strategies on the device parameters and efficiency. Therefore, establishing series of reasonable experiments are significant for modelling different behaviors of the parameters at different realistic conditions. This leads to the basic development of further optimization regarding fabrications. Additionally, it would be possible to correlate crucial loss mechanisms to the corresponding cell modification and conclude on methods to prevent such deficiency in the output power.

4.1 Characterization methods
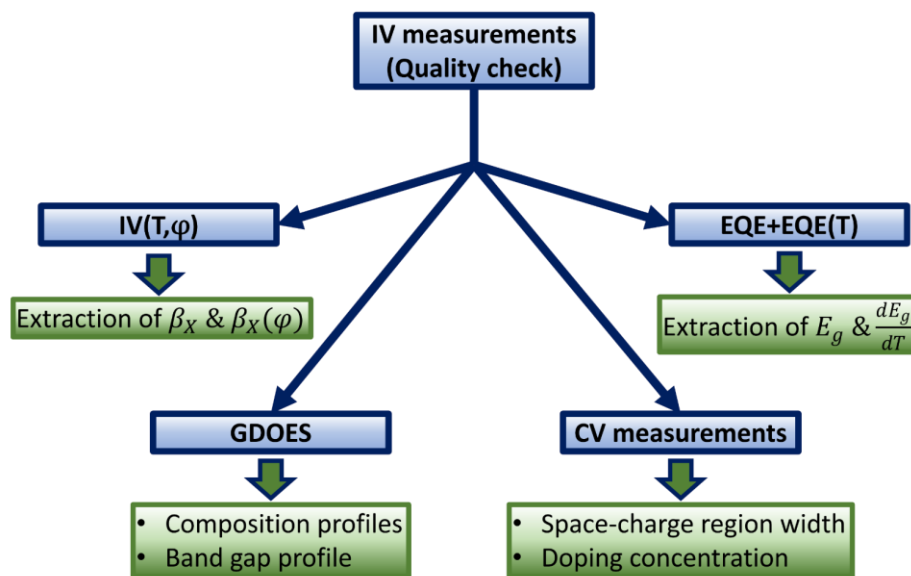
Figure 11: Schematic of general characterizations realized on all studied CIGS solar cells.

4.1.1 Standard IV measurements and solar cell parameters

The IV set-up comprises a halogen lamp light source (Photo Emission Tech SS100AAA), to mimic the standard condition spectrum (AM1.5g). The solar simulator was left on for about two hours to properly stabilize it. After that, its light intensity was adjusted using a Si solar cell reference with calibrated J_{sc} value at 1000 W/m^2 and 25 °C conditions. In addition, a height

adjustable sample stage was used to compensate for the thickness mismatch between the reference cell and the cell under investigation. The stage is adapted to a temperature water cooler to set the cell's temperature to 25°C, which was monitored by a sensor coupled to a dummy CIGS cell. Light intensity variations were realized by using diverse optical density filters with multiple transmittance values, ranging from ~95% to ~18% transmission on light with wavelengths over 300 nm. Solar cells' active areas were measured in a Ritzroboter setup, using the software Dino Capture.

The voltage source and the current measurement units are combined in a Keithley 2400 device. To avoid parasitic resistances between the solar cell and the metallic probes, four-point measurements were carried out. Two probes were used to apply the voltage between the cell's contacts and two more were used in parallel to measure the output current. The voltage range applied on the solar cell was from -0.2V to 1V, and a compliance current of 0.1A to protect the solar cell.

IV measurements are a fundamental characterization technique for solar cells. With them, conversion efficiencies and other solar cells parameters can be obtained. In Figure 12, an overview of all solar cell parameters obtained from a typical IV measurement are shown. Under illumination and no bias, the solar cell produces current that is dependent on the illuminated area and the illumination intensity. This current normalized to the active cell area value is called short-circuit current density J_{sc}, which is known to be the maximum current density that flows through the cell at zero load conditions. The voltage under open-circuit conditions (no current flow) is called open-circuit voltage (V_{oc}). The power at maximum power point (P_{mpp}) is the highest value of power a solar cell can produce.
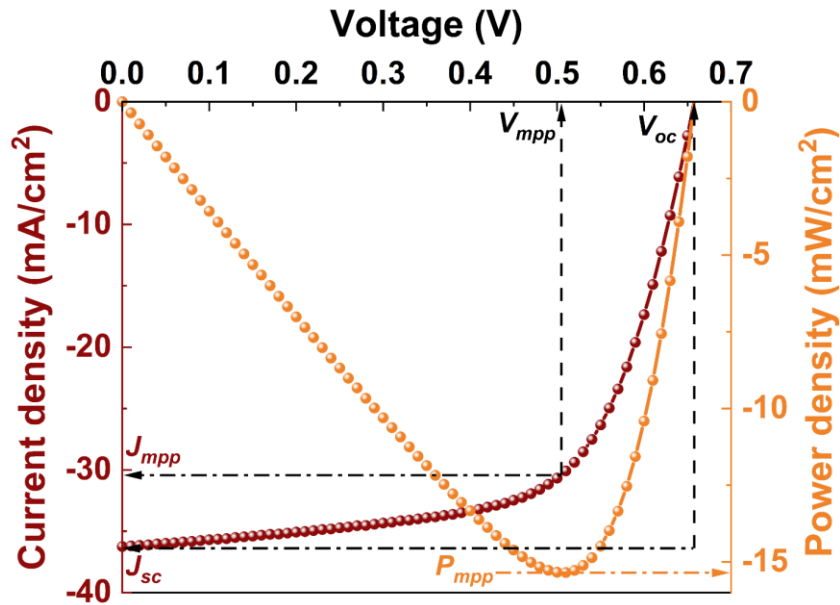
Figure 12: Representative example of an JV curve of an illuminated solar cell (red) and the corresponding P-V curve.

The fill factor (*FF*) is calculated as

$$FF = \frac{P_{mpp}}{V_{oc} * J_{sc}}$$

(4.1)

It is a measure of the squareness of the JV curve. It can be reduced by parasitic series/shunt resistive losses. The shunt resistance R_{sh} is the slope of the IV curve around 0V. It is required to have high R_{sh} value to avoid current losses in shunt paths. Conversely, a low series resistance R_s is desired to avoid voltage losses. The ideality factor determines the junction quality as well as the type of recombination in a solar cell. It typically takes values from 1 to 2 but it can be higher than 2 in case of high defect densities [134] , which will reflect negatively on the V_{oc} and *FF* (see Chapter 7). The extraction of the series and shunt resistances R_s and R_{sh}, diode ideality factor *m* and the saturation current density J_0 are realized by following the procedure proposed by Hegedus *et al*. [135].

4.1.2 Parameter's extraction. Hegedus method

Although basic solar cell parameters V_{oc}, J_{sc}, *FF*, P_{mpp} and efficiency (*η*) are good indicators of its performance, there is plenty of information regarding parasitic losses that can be obtained if the whole JV curve is analyzed. For this, four different plots are necessary, where comparisons between dark and white light illuminations are made. These are:

    (a) Standard JV curve. Where sufficient data from the first and third quadrant is present, in order to observe non-idealities, as described in equation (3.14).

(b) Plot of dJ/dV vs V near J_{sc} and reverse bias. As the diode current is negligible in this bias region, the shunt resistance can be extracted, assuming it has an ohmic behavior.

(c) Plot of dV/dJ vs $(J+J_{sc})^{-1}$. From equation (3.14) it yields

$$\frac{dV}{dJ} = R_s + \frac{mkT}{q}(J+J_{sc})^{-1} \qquad (4.2)$$

considering $R_s/R_{sh} \ll 1$. This plot will give a straight line, whose intercept with the Y-axis is R_s and its slope is mkT/q, from where m can be obtained. If the effect of R_{sh} is not negligible, the X-axis can be $(J+J_{sc}-V/R_{sh})^{-1}$ instead.

(d) Plot of $\ln(J+J_{sc})$ vs $(V-R_sJ)$ after having acquired the value of R_s from plot (c). Rearranging equation (3.14), results in

$$\ln(J+J_{sc}) = \ln(J_0) + \frac{V - R_sJ}{mkT} \qquad (4.3)$$

Here, a linear region would indicate a proper fit to the diode equation (3.14), where the intercept with the Y-axis indicates J_0, and the slope is q/mkT, so m can be calculated again and compared with the value obtained from plot (c) [135]. If R_{sh} is not large enough, the Y-axis can be represented by $\ln(J+J_{sc}-V/R_{sh})$ instead.

4.2 Light soaking treatment

To account for the stability of all solar cells under white light conditions, IV measurements under different illumination times were performed. For all measured cells, it was shown that their parameters changed with illumination time and stabilized after ca. 2 hours of white light exposure. In Figure 13, graphs show the evolution of V_{oc}, and FF for representative examples of the studied cells.
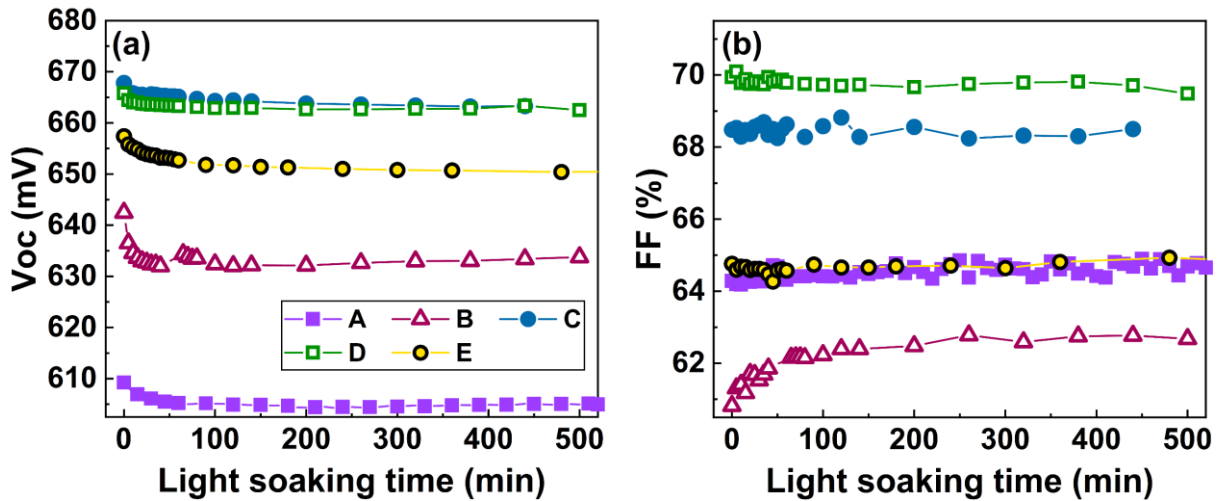
Figure 13: Light soaking studies for cells A-E. As light exposure passes, solar cell parameters stabilize.

4.3 IV-temperature dependent measurements

IV measurements were further taken at different temperatures. These measurements provide information about the solar cell's recombination mechanisms, as well as solar cell parameters' sensitivity towards temperature variations. Also, it can give information about the existing heterostructure interface barriers.

Characterization was performed inside a closed-cycle helium cryostat using a xenon lamp spectrally adjusted by a water filter as light source. IV measurements were taken in a temperature interval of 293 to 323K, in steps of 5K. The cell temperature was controlled by a Lake Shore 336 unit and monitored by a Si-diode sensor mounted directly on top of the cell, near the active area. IV recordings were realized with a Keithley 2400 in a four-point probe arrangement to avoid parasitic resistances between contacts. The applied voltage interval was from -0.2 to 1V and a compliance current of 0.1A was used. A revolver between the lamp and the sample allows to select between multiple density filters (1, 0.5, 0.2 suns), and a red-light filter (>600 nm) for illumination measurements.

To account for error in the measurements, a test cell was measured five times under the conditions mentioned above. The position of the solar cell on the sample holder was kept exactly the same in each of the measurements to assure identical illumination area (see Supplementary information Table S. 1).

Solar cell temperature coefficients

As described in Section 3.3, solar cell efficiencies tend to decrease linearly with temperature. This linear trend is also similar to the rest of solar cell parameters. For this reason, it is practical

*Light soaking measurements made in collaboration with Dr. Hippolyte Hirwa.

to express the temperature sensitivity of solar cell parameters with a single temperature coefficient ($\beta_{X,\ rel}$) value, normalized to the corresponding parameter value at 298K (X_{298K}), as

$$\beta_{X,rel} = 100 \frac{1}{X_{298K}} \beta_{X,abs} = 100 \frac{1}{X_{298K}} \frac{X(T_2) - X(T_1)}{T_2 - T_1} \qquad (4.4)$$

where X is the parameter of interest, $\beta_{X,abs}$ is the absolute temperature coefficient, and the *100* factor is included to express $\beta_{X,\ rel}$ in %/K units.

Considering a linear decrease of V_{oc}, J_{sc}, FF and P_{mpp} with temperature, a relation between the temperature coefficients of all these four parameters can be assessed. Recovering the expression of P_{mpp}

$$P_{mpp}(T) = V_{oc}(T) * J_{sc}(T) * FF(T) \qquad (4.5)$$

By differentiating equation (4.5) with respect to temperature, and dividing the result by equation (4.5), it yields

$$\beta_{P_{mpp},rel} = \beta_{V_{oc},rel} + \beta_{J_{sc},rel} + \beta_{FF,rel} \qquad (4.6)$$

It has been reported that, for high quality solar cells, the contribution of $\beta_{V_{oc},rel}$ to $\beta_{P_{mpp},rel}$ can be of up to 90% of its value [34]. Therefore, it is worth describing the behavior of the temperature coefficient of V_{oc}.

Green proposed a dark saturation current in the form of

$$J_0 = AT^{\gamma'} e^{-\frac{E_{g0}}{mkT}} \qquad (4.7)$$

where A is a parameter independent of temperature, E_{g0} is the absorber band gap at 0K, and γ' accounts for the temperature dependence of a range of microscopic processes, like diffusion lengths, carrier mobilities or effective densities of states [136].

By using equation (3.14) and assuming $R_s=0$ and $R_{sh} \rightarrow \infty$, and combining it with equation (4.7), the open circuit voltage can be expressed as

$$V_{oc} = \frac{E_{g0}}{q} - \frac{mkT}{q} \ln \left(\frac{AT^{\gamma'}}{J_{sc}} \right) \qquad (4.8)$$

By taking its derivative respect to temperature, it gives

$$\beta_{Voc,abs} = \frac{dV_{oc}}{dT} = -\frac{1}{q} \frac{(E_{g0} - qV_{oc}) + \gamma kT}{T} \qquad (4.9)$$

where γ represents the product ($m\ \gamma'$).

4.4 External Quantum efficiency

The photovoltaic external quantum efficiency (EQE) is defined as the ratio of incident photons to extracted electrons, it is equivalent to a solar cell's spectral response (SR), which is determined by the amount of current density produced by the incident power radiation.

$$SR = \frac{J_{out}(\lambda)}{P_{in}(\lambda)} \qquad (4.10)$$

The EQE can then be obtained as

$$EQE(\lambda) = SR\,\frac{hc}{q\lambda} \qquad (4.11)$$

The short circuit current density can be obtained by the multiplication of SR with the illumination spectrum and integrating over the wavelength range as

$$J_{sc} = \int_0^\infty P_{AM1.5g}(\lambda) * SR(\lambda)d\lambda = q \int_0^\infty P_{AM1.5g}(\lambda) * \frac{\lambda}{hc} * EQE(\lambda)d\lambda \qquad (4.12)$$

where $P_{AM1.5g}$ is the incident spectral power density (in W/cm^2 nm). Ideally, the J_{sc} obtained from IV and EQE measurements should be similar, however this is not always the case, as the spectral mismatch between lamps and the actual solar spectrum can occur [135]. This measurement gives information on density of electrons that are extracted from a solar cell device corresponding to a specific wavelength of incident photons.

Ideally, the ratio between extracted minority carriers to incident photons should be equal unity, whereas the quantum efficiency is zero when the incident photons have an energy below the band gap, since they are not being absorbed. In such ideal case, the EQE spectrum is represented as a squared shape. In a more realistic case, the EQE is less than one due to the associated loss mechanisms [137].

Minimum band gap energy determination

The common approach to determine the band gap of thin film solar cells rely on the study of the low-energy wing of EQE measurements. There are multiple methods used to extract the band gap from this region, each of them with their limitations. Two of the most commonly used ones are stated below:

- $\left(E_{ph} * \ln(1 - EQE)\right)^2 vs\ E_{ph}$ plot: For the case of direct band gap absorbers, this method assumes an absorption coefficient α through the absorber of the form $\alpha \propto$

$\sqrt{E_{ph} - E_{g,min}}$. In this case, the plot gives a straight line in the low-energy values and its intersection with the X-axis gives the $E_{g,min}$ value. Although this method gives reliable results in non-graded high-quality absorber solar cells, it fails when used to obtain the $E_{g,min}$ of a graded absorber, as in the case of most CIGS solar cells. The failure in this method is due to inappropriate linear fitting intervals, which is user dependent, and the non-square root behavior of α on these absorbers [138].

- Peak of *d(EQE)/dλ*: Multiple works interpret the peak position of the EQE derivative in the high wavelength region as $E_{g,min}$ [139], [140]. This method appeared to be more robust since it is not affected by subjective linear fitting regions, as in the previous case[141]. Although this method has been criticized as "unphysical"[142], further studies have proposed it as an "external" property of the solar cell, instead of an "internal" one (like the previous method) [140]. The derivative method has served to consistently study solar cells' V_{oc} losses, by using only externally measured properties [140].

In Figure 14, a comparison of both extraction methods is shown. Clearly, the linear extrapolation method differs from the derivative method by about 25 meV. For the solar cells used in this work, band gaps were extracted with the derivative method.
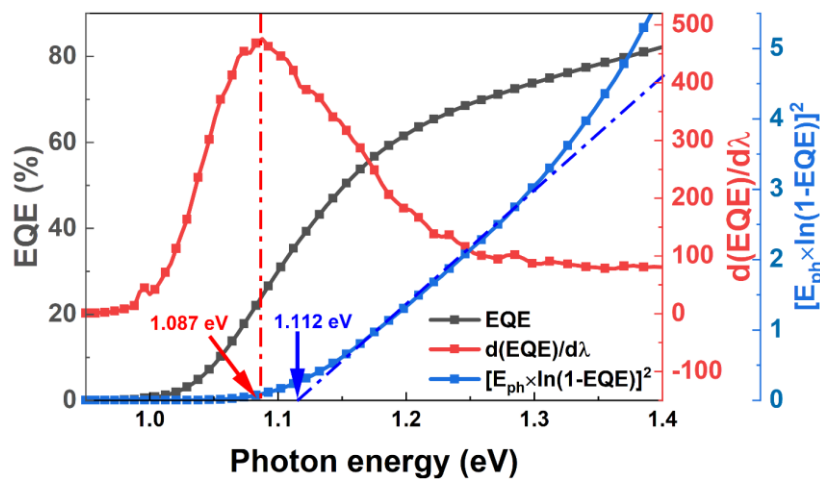
Figure 14: $E_{g,min}$ extraction approaches from EQE measurements.

4.5 CV measurements

Capacitance-voltage (CV) measurements are a widely used method to obtain the doping density of CIGS solar cells as well as the width of the space charge region (SCR). This is achieved by applying a small AC signal offset with a varying DC voltage. The former allows to obtain the capacitance of the junction, and the latter gives information about the SCR width (W_{SCR}). The

capacitive characteristics of a single junction solar cell can be approximated by a resistor in parallel with a capacitor. Some assumptions are generally taken into account when analyzing the solar cell capacitance. The depletion approximation considers an abrupt end of the SCR, and that it is totally emptied of free carriers. In this condition, an applied bias will change the W_{SCR}. Furthermore, the charge density inside the SCR is estimated to stay constant. In order to avoid the contribution of defect states to the capacitance, a high enough AC frequency must be used. The capacitance of the solar cell can then be approximated to a parallel plate capacitor as

$$C = \varepsilon \frac{A}{W_{SCR}(V)}$$

(4.13)

where ε is the permittivity of the junction and A is its cross-sectional area.

CIGS solar cells' *p-n* junctions are typically one sided, which means that the doping densities on each side of the junction vary by some orders of magnitude. In this case, the W_{SCR} extends along the least doped side and can be expressed as

$$W_{SCR} = \left[\frac{2\varepsilon}{qN_A} \left(V_{bi} + V - \frac{kT}{q} \right) \right]^{1/2}$$

(4.14)

The CV analysis via the Mott-Schottky evaluation can be used to infer the doping density of the CIGS absorber. Assuming a constant acceptor density through the whole absorber, the Mott-Schottky equation reads

$$\frac{1}{C^2} = \frac{2}{qA^2\varepsilon N_A} \left(V_{bi} + V - \frac{kT}{q} \right)$$

(4.15)

By plotting $1/C^2$ vs V, the acceptor density can be obtained from the slope, followed by the V_{bi} from the intersection with the Y-axis.

4.6 Glow discharge optical emission spectroscopy

Glow discharge optical emission spectroscopy (GDOES) is an extensively used characterization technique to analyze quantitively and qualitatively the chemical composition of the materials under investigation as a function of their gradient profile depth. The device consists of a small glow discharge chamber with an aperture where a sample is mounted facing to the inside. The glow discharge chamber is filled with argon gas, which will then be ionized by an applied potential between electrodes. This will lead to the creation of the argon plasma. This argon plasma, due to electrical attraction, will be accelerated towards the cathode where

the sample rests. Upon the impact of argon ions with the sample, atoms from the latter will be ablated and diffused into the plasma.

The measurement technique is based on analyzing the photons emitted from the plasma relaxation of the ablated sample, by calibrated Paschen-Runge spectrometer. The exact depth of the detected material is referred by other techniques like ellipsometry or scanning electron microscopy. Since this technique requires the subsequent sputtering of the sample. It becomes not suitable for in situ characterization tool. For more details on the accuracy and calibration of the experiment, the reader can refer [143].

4.7 Cells Preparation

The CIGS samples were acquired in a pilot line by Avancis (Munich) by the following layer arrangement: glass substrate, back electrode, absorber, buffer, i-layer, ZnO window. The fabrication process is briefly addressed here (for more details on the process the reader is referred to the work of Dalibor *et al*. [144]). CIGS absorbers were prepared by stacked elemental layer (SEL) precursors that were deposited by sputtering, and subsequently reacted by a rapid thermal process (RTP) with S-containing atmosphere and Se evaporation. The band gap grading with the elemental depth distribution in the absorber layer were achieved by changing the Ga/In and S/Se ratios, employing a variation of the precursor composition or a variation in the RTP process. The window layer consisting of (Zn,Mg)O i-layer, ZnO:Al front contact and the Zn(O,S) buffer layer were deposited by sputtering. The InS:Na buffer layer was prepared by thermal evaporation. Two back contact types were implemented on a Mo-based or a Cu-Mo-based back electrode, respectively. A silicon nitride barrier between substrate and the back-contact was incorporated for preventing alkali diffusion from the glass into the absorber layer in order to have control over this process. All cells used in this work were not laminated at the end step of the fabrication process.
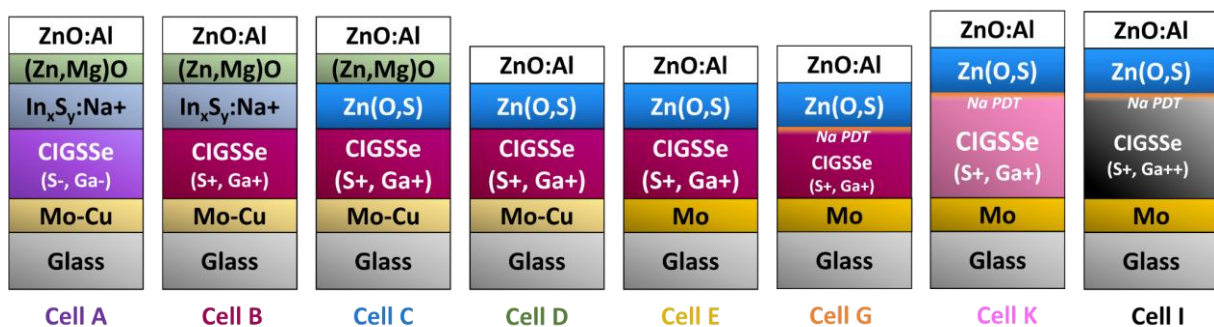
Figure 15: Layer structures of all non-laminated CIGS solar cells used in this work.

For clarity, each two neighboring sample types from Figure 15 only differ in one layer or treatment, so that each modification' influence can be investigated solely.

Chapter 5 CIGS solar cells' temperature coefficients

In this section, the influence of temperature variation on solar cell parameters are shown and discussed in terms of different layer structures. The temperature sensitivities are extracted for each structure and expressed as temperature coefficient. To further improve and to tailor CIGS temperature behavior for different environments, it is important to gain a detailed understanding of the microscopic mechanisms involved. Therefore, physical parameters that drive the temperature coefficient are discussed, and an empirical correlation is presented.

5.1 Methods

First, the characterization started by two hours of light soaking on all cells at STC to stabilize the IV curves [145]. The temperature hysteresis check was performed for all cells by going up and down in the temperature range 293 to 323 K. Afterwards, IVT measurements were performed for two cells of each variation type at 1 sun light intensity, starting from 293 to 323 K (20-50°C) with 5 K steps. At 298 K, the STC parameters were extracted. The external quantum efficiency (EQE) measurements* were performed to obtain the minimum band gap energy ($E_{g,min}$) values, which were extracted by the first order derivative of the EQE ($dEQE/d\lambda$) [23], where λ is the wavelength. The band gaps at 0K were obtained by operating EQE at room temperature and ramping 5 K steps up to ~55°C, then by T-dependence linear extrapolation of the band gap to 0 K [23]. The band gap profiles were attained from GDOES measurements. All results were obtained from the measurements and analysis of two cells from the same type. Absolute temperature coefficients $\beta_{X,abs}$ and relative temperature coefficients $\beta_{X,rel}$ were calculated as described in Section 4.3.

---

*EQE(T) measurements made by Dr. Hippolyte Hirwa and Dr. Jörg Ohland.

5.2 Results

A representative example of IV(T) for cell K is shown in Figure 16.
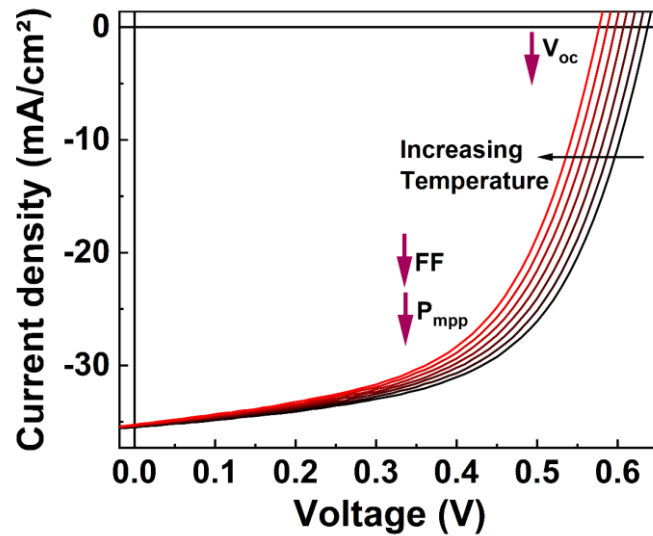
Figure 16: Behavior of a current-voltage curve at different temperatures. As temperature increases, V_{oc}, FF and P_{mpp} and η parameters deteriorate.

The V_{oc}, FF and P_{mpp} parameters were extracted at the previously mentioned range of temperatures. In Figure 17, it can be observed that V_{oc}, FF and P_{mpp} decrease linearly with increasing temperature, and J_{sc} change slightly with temperature.

For all samples, the extracted solar cell parameters at STC were in the following ranges: V_{oc} = 590-695 mV, J_{sc} = 32.2-37.2 mA/cm^2, FF = 54-70%, P_{mpp} = 13.1-16.7 mW/cm^2. Only one cell type, B, showed a metastable behavior for the $FF(T)$. This will be discussed in more detail in the next chapter.
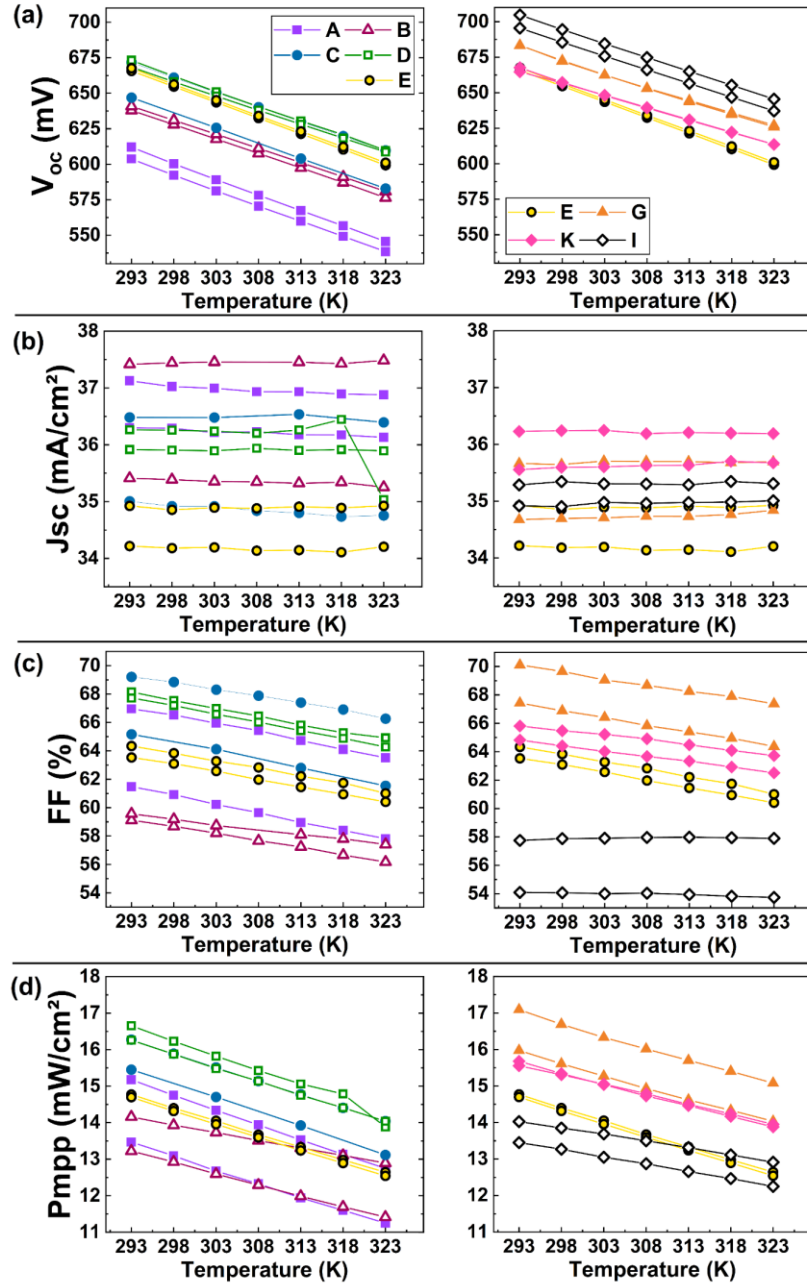
Figure 17: Behavior of (a) V_{oc}, (b) J_{sc}, (c) FF and (d) P_{mpp} parameters between 293 to 323 K at a constant illumination intensity of 1 sun*. For clarity, behaviors from cell A-E and cells E to I were separated in the left and right columns, respectively. Legend labels indicate the cell type.

The following results show the contribution of $\beta_{X,rel}$ to the total $\beta_{Pmpp,rel}$ using equation (4.6), from methodology section. In average, the $\beta_{Voc,rel}$ contributes with around 65± 5.5% to the $\beta_{Pmpp,rel}$ value, followed by 35±3.5% of $\beta_{FF,rel}$ contribution for the presented CIGS cells. Therefore, the relative temperature coefficients $\beta_{Pmpp,rel}$ and $\beta_{Voc,rel}$ were used to compare different solar cell's temperature sensitivity. The resulting relative temperature coefficients $\beta_{Pmpp,rel}$ and $\beta_{voc,rel}$ are shown in Figure 18a and b, respectively. It is noted that the experimentally observed differences in $\beta_{Voc,rel}$ between samples follows partially the general

*IV(T) measurements made in collaboration with Mohamed Elshabasi.

behavior of V_{oc} under STC, while the rest of the contribution comes from the $\beta_{Voc,abs}$ (see supplementary information, Figure S 1).
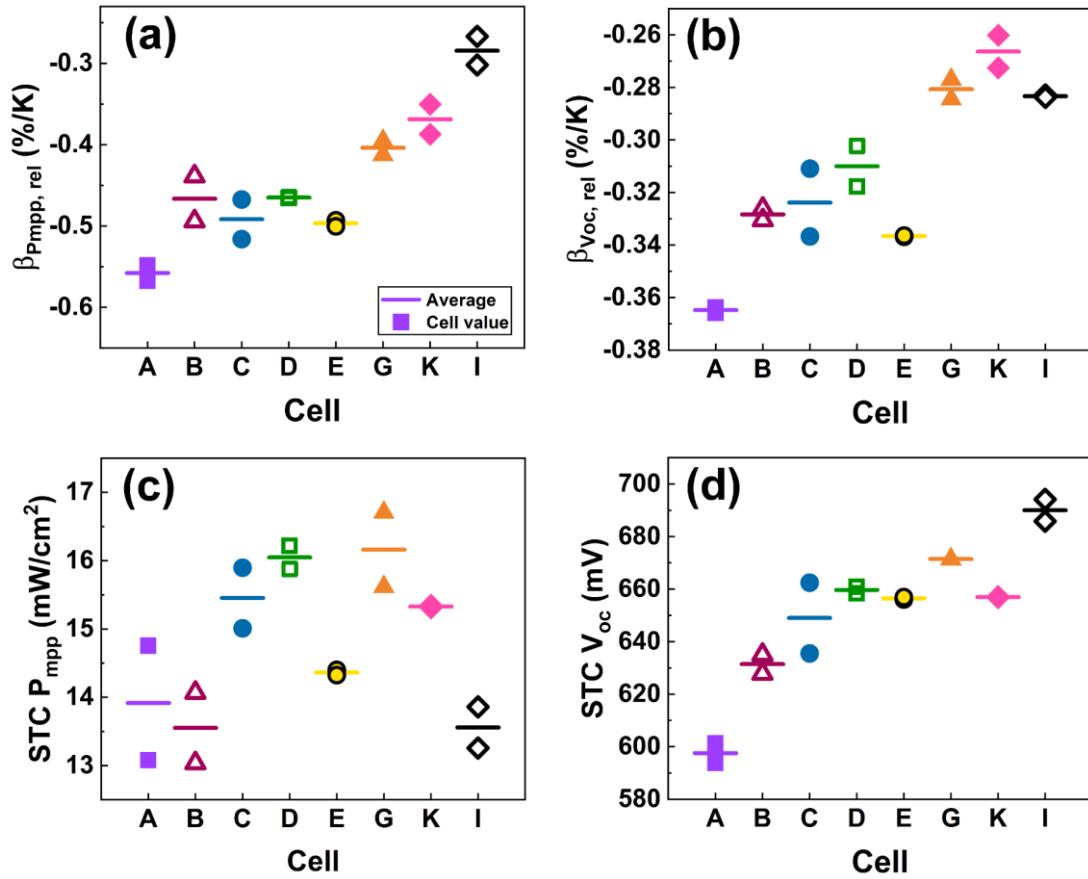
Figure 18:(a) $\boldsymbol{\beta_{Pmpp,rel}}$ (b) and $\boldsymbol{\beta_{Voc,rel}}$ temperature coefficients for all studied CIGS solar cells. The (c) P$_{mpp}$ and (d) V$_{oc}$ behaviors between each cell layer modification is also shown.

Table 2. E$_{g,min}$, band gap temperature coefficient, and 0 K-extrapolated band gap (E$_{g_0}$) for all studied CIGS solar cells.

Cell	$E_{g,min}$ [eV]	E_{g_0} [eV]	dE_g/dT [eV/K]
■ **A1**	1.048	1.076	-9.36E-05
■ **A2**	1.048	1.076	-9.36E-05
■ **B1**	1.085	1.120	-1.18E-04
■ **B2**	1.076	1.111	-1.18E-04

■	**C1**	1.095	1.120	-8.19E-05
■	**C2**	1.099	1.123	-8.19E-05
■	**D1**	1.113	1.140	-9.24E-05
■	**D2**	1.093	1.121	-9.24E-05
■	**E1**	1.133	1.155	-7.24E-05
■	**E2**	1.135	1.156	-7.07E-05
■	**G1**	1.088	1.108	-6.57E-05
■	**G2**	1.092	1.121	-9.93E-05
■	**K1**	1.085	1.109	-8.19E-05
■	**K2**	1.085	1.113	-9.29E-05
■	**I1**	1.164	1.185	-7.07E-05
■	**I2**	1.163	1.185	-7.40E-05

From the V_{oc} absolute temperature coefficient ($\beta_{Voc,abs}$) expression deduced in equation (4.9), the term $\frac{E_{g0}}{q} - V_{oc}$ can make reference to the V_{oc},def, which indicates the quality of solar cells [146]. The γ term is the dark saturation current dependence on temperature. This term accounts for the carrier diffusion lengths, the electron and hole mobilities as well as the doping densities and the effective densities of states [147], [148]. For studying the influence of both parameters on the $\beta_{Voc,abs}$, the γ values and V_{oc},def were extracted for all cells and plotted versus $\beta_{Voc,abs}$(Figure 19). A stronger direct correlation is observed between $\beta_{Voc,abs}$ and γ with a correlation coefficient ρ = –0.90, whereas the correlation between $\beta_{Voc,abs}$ and the V_{oc},def is weakly negative ρ = –0.63. It is worth noting that using E_g or E_{g0} does not make a tangible difference, as can be seen from Table 2, because both values are similar.
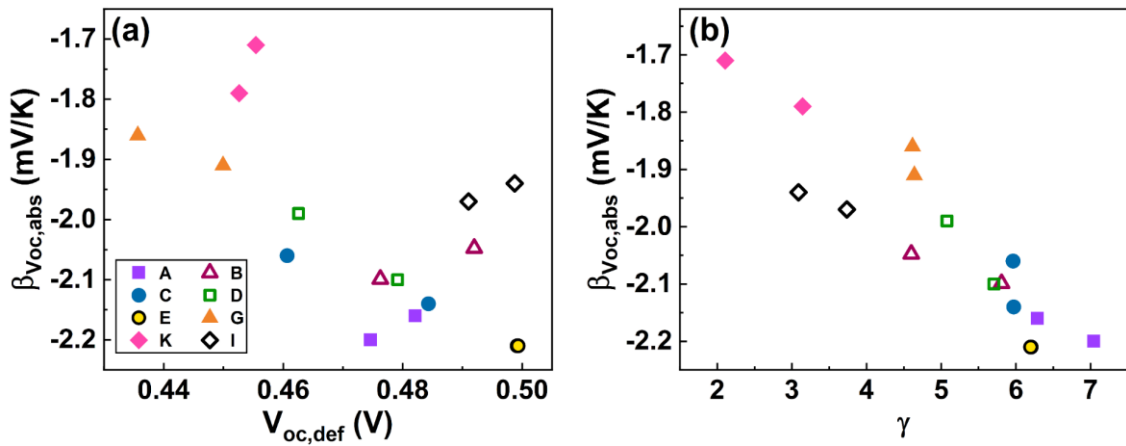
Figure 19: (a) Comparison between $\beta_{Voc,abs}$ and (a) V_{oc}, def and (b) γ. Legend labels indicate the cell type.

In order to have deeper insights on the individual corresponding impact of both γ and V_{oc},def terms to the total $\beta_{Voc,abs}$, a comparison of the contribution of each term to the total $\beta_{Voc,abs}$ was made. In Figure 20, it can be seen that V_{oc},def has a larger contribution to the $\beta_{Voc,abs}$ compared to γ parameter. Nevertheless, the γ term has a larger variation through all cells.
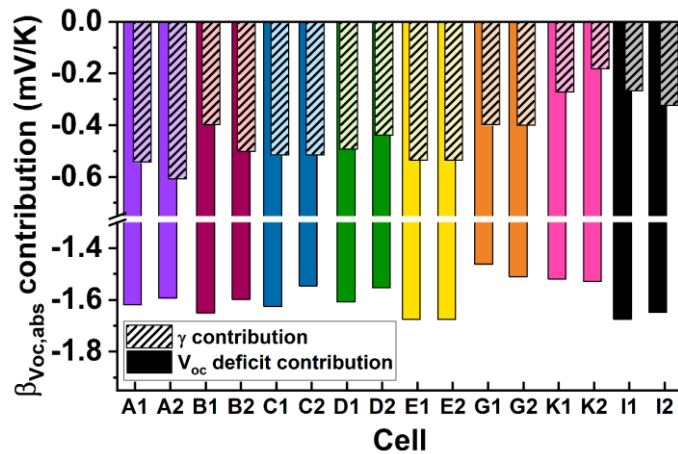
Figure 20: Contribution of γ and V_{oc},def terms to the total $\beta_{Voc,abs}$. Larger contributions come from V_{oc},def, while larger variations come from γ.

5.3 Discussion

The $\beta_{Voc,rel}$ correlation with V_{oc} at STC partially results from the basic definition of the relative temperature coefficient, that depends on the V_{oc} at STC, and the remaining contribution to $\beta_{Voc,rel}$ comes from $\beta_{Voc,abs}$. (see Supplementary information, Figure S 1). It was found that $\beta_{Pmpp,rel}$ was mainly driven by $\beta_{Voc,rel}$.

In Figure 20 is shown that although the V_{oc},def term has a larger overall contribution, the variations in $\beta_{Voc,abs}$ in these samples are strongly determined by the variation in the γ

parameter. It is interpreted as the reason why γ is the main parameter causing changes in $\beta_{Voc,abs}$. In particular, cells A and K, which show the worst and best $\beta_{Voc,abs}$, respectively, differ mainly in the γ-contribution to $\beta_{Voc,abs}$. It can be seen for cells K, which have the lowest contribution of γ, that also have the smallest $\beta_{Voc,abs}$. On the other hand, cells A have the highest contribution of γ, as well as the worst $\beta_{Voc,abs}$ (cf. Figure 19b).

From an empirical study of the V_{oc},def , it can be seen that the distribution of $\beta_{Voc,rel}$ can be grouped in three main zones, being the principal zone the one following a linear correlation with V_{oc},def. This zone includes cells B, C, D, E and G, all of them sharing an absorber with nominally similar Ga profiles and thickness confirmed from GDOES. As heterointerfaces' quality of cells in this zone improve, so does their $\beta_{Voc,rel}$, which can be indicated by the value of V_{oc},def. This is further confirmed by looking at the remaining two zones being outside of this linear trend. For example, for cells A, a Ga profile with reduced GGI ratios is used, and their $\beta_{Voc,rel}$ and V_{oc},def. do not fall on this linear trend. On the other side, cells K and I, have an increased thickness and Ga profile, respectively. It becomes evident, that increasing the GGI ratios of the Ga profile enhances the $\beta_{Voc,rel}$ considerably. On the following, a direct comparison between neighboring cells appearing on the first zone will be discussed.
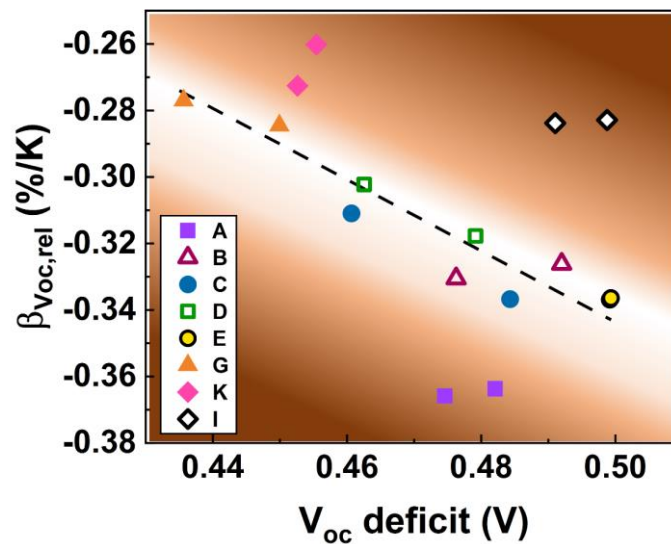
Figure 21: Empirical correlation between $\beta_{Voc,rel}$ and V_{oc},def. A linear trend is found for solar cells with nominally similar Ga grading.

By keeping the fabrication inhomogeneities low for cells C, as in the rest of cells, it can be concluded that a small enhancement is observed for both $\beta_{Voc,rel}$ and V_{oc},def when a Zn(O,S) buffer layer is used instead of an In_xS_y buffer layer (as in cells B). Furthermore, a perceivable improvement on V_{oc} is observed (cf. Figure 18d). Comparing cells C to D, it can be noticed no

considerable improvement of $\beta_{Voc,rel}$ and $V_{oc},def,$ owing to the fact that removing the i-layer doesn't directly affect the absorber's interfaces' quality.

As studied before, the Cu rich in the back part of the absorber and Cu poor in the front part leads to an enhancement in the V_{oc} [149], and hence, a higher $\beta_{Voc,rel}$. By comparing cells D and E, a detrimental effect is observed when the pure Mo-based back contact is used instead of the Cu-Mo-based back contact. GDOES analysis showed a relatively lower Cu concentration on cells E in the back side of the absorber, as well as a Cu gradient towards the back contact. This effect is not seen in cells D, which suggests that a proper amount of Cu in the back contact could function as a Cu diffusion semi-barrier or Cu compensator for the absorber, preventing the back side of the absorber of becoming Cu poor. According to the V_{oc},def values for both D and E cells, it is evident that the interfaces surrounding the absorbers of cells E are of lower quality than of cells D.

An outstanding effect is evident when cells E and G are compared, which show the effect of a Na post deposition treatment (PDT), known to passivate heterointerface defects [150]. Although cell E shows one of the most detrimental $\beta_{Voc,rel}$ values, this treatment enhanced the quality of the heterointerface remarkably, noticeably improving V_{oc},def.

Taking into account the individual effect of each studied layer modification, it seems plausible to consider that a solar cell with improved temperature sensitivity would consist of a Mo-Cu-based back contact. A CIGS absorber with the Ga profile of cells of zone 1 (cf. Figure 21) would also be necessary. As buffer layer, the Zn(O,S) material appeared to yield the best results and avoid metastable behavior. Although the effect of the i-layer appeared to be negligible under the used illumination conditions, it is encouraged to be included as it can prove to be beneficial when using the final solar cell under lower illuminations (further discussed in the low light chapter). Finally, a PDT is encouraged to be implemented, as it proved to be one of the most remarkable modifications regarding temperature stability.

5.4 Summary

Different characterization methods were used on the eight different CIGS samples variations, in order to investigate the relation between the layer variation and the cells β_X. From the one diode model, γ showed to be the key parameter behind the enhancement of $\beta_{Voc,abs}$. It was found that the most influencing layer on the cells' β_X is the absorber layer, as the rest layer variations did not show a significant difference. In order to enhance $\beta_{Pmpp,rel}$, $\beta_{Voc,rel}$ has to

be improved as it contributes with more than 65% of the $\beta_{Pmpp,rel}$ value for CIGS, followed by $\beta_{FF,rel}$ which also provided with 30% of it, approximately. There is a quite interesting clear linear correlation between $V_{oc,def}$ and $\beta_{Voc,rel}$ for the same absorber thickness and GGI profile, which could shade an initial approach to optimize the $\beta_{Voc,rel}$ through the absorber fabrication stage.

Chapter 6 Experimental assessment of metastable behavior of *FF* temperature coefficients in CIGS solar cells

In this chapter, metastable effects seen on four samples of cell B, which were mentioned briefly in Chapter 5 are discussed in more detail. To deepen in the understanding of this phenomena, the presence of metastable states is studied for different buffer/absorber heterojunction structures, i.e., for cells A, B and C, which present subsequent modifications on this interface. The location of the source of the metastability is determined. Additionally, the origin of metastability in the corresponding structure is suggested. The buffer photoconductivity effect and its relevance to the metastability effect is also inspected.

6.1 Methods

The IV and IV(*T*) spectral dependence measurements were implemented and carried out in the short and long wavelength range. For IV(*T*) measurements, high temperature (298 to 323K) as well as low temperature ranges (100 to 150K) were used. Samples were preconditioned by light soaking treatment with the corresponding wavelength of interest for two hours.

IV measurements were carried out under $\lambda > 600$nm ("red light") and λ between. ~300 to ~600 nm ("blue light"). This is a basic method to identify characteristics that are known to distort IV curves. As described in Section 3.2, such IV distortions can be, among others, the so-called red kink, perceived in the fourth quadrant, and/or rollover effect, perceived in the first quadrant.

EQE measurements were performed under red and blue light bias light to account for the photodoping effect described before in Section 3.4.2.

CV measurements have been applied in low temperature conditions before and after red light soaking and before the measurement a reverse bias was applied for 20 minutes (ROB) to accounts for the change in acceptor density in each cell.

Cross-sectional EDX measurements were performed on a JEOL 2100F Schottky field emission transmission electron microscope. For this elemental characterization, a cell B lamella of ~200 nm thickness was prepared in a FEI Helios Nanolab 600i SEM-FIB setup.

6.2 Results

As a first approach, IV(*T*) hysteresis measurements were taken for cells A, B and C in the temperature range of 293 to 323 K. The hysteresis cycle (HC) started with a ramping-up in temperature and ended with the ramping down. The corresponding behavior is shown in Figure 22. It can be seen that for cells A and C, V_{oc}, *FF* and P_{mpp} parameter's trend remain unchanged during ramping-up and down in temperature (cf. Figure 22a-c). On the other hand, cell B, shows a significant difference in its *FF*(*T*) characteristics, and to a lesser extent in P_{mpp}(*T*) as well (cf. Figure 22d-f).
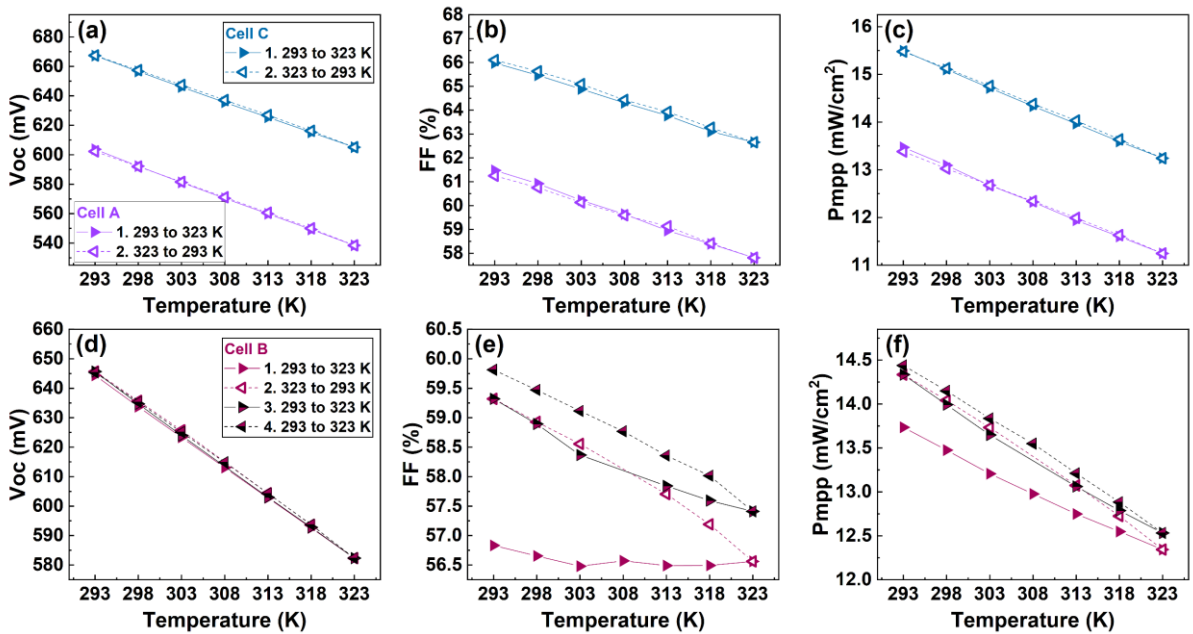
Figure 22: (a) V_{oc}, (b) FF and (c) P_{mpp} behaviors of cells A and C through one temperature hysteresis cycle. (d) V_{oc}, (e) FF and (f) P_{mpp} behaviors of cell B through two temperature hysteresis cycle. For all cases, one sun white light illumination was used.

$\beta_{FF,rel}$ were extracted for all four temperature runs, shown in Figure 23. At a first glance, it seems that when measurements are taken from low to high *T*, there is a better temperature coefficient, in comparison to the ones taken from high to low *T*. As all three cells were white light-soaked for two hours, it is then evident that cell B presents a different stability response.
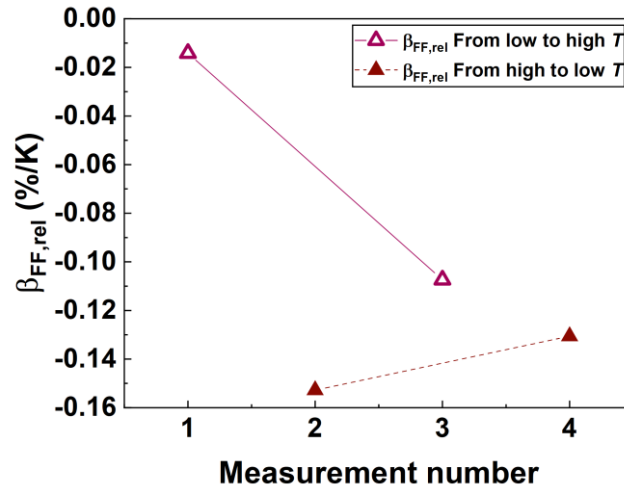
Figure 23: $\beta_{FF,rel}$ for cell B under white light.

To account for the spectral effect of light on the studied cells, IV-curves under red and blue illumination IV(λ) were performed and shown in Figure 24. It is noted that cell B shows a higher *FF* under blue light as compared to red light. (Figure 24b). Whereas cells C and A did not show a difference of comparable magnitude under same wavelength conditions. The effect of red light on cell B is seen as an increase in series resistance and a decrease in shunt resistance, which directly affect *FF*. This detrimental effect is not seen in cell A and relatively slightly in cell C, suggesting that the presence of red photons during measurement is the primary source of metastability in cell B. On the following, particular attention will be given to the overall behavior of cell B.
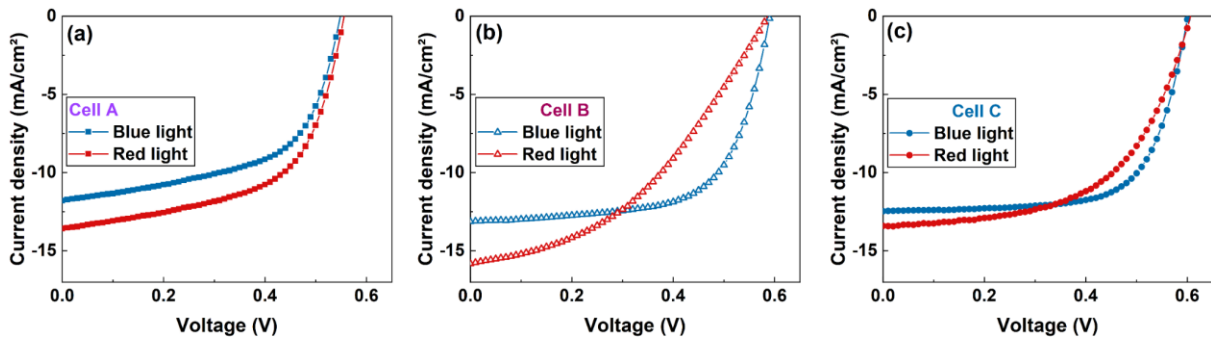
Figure 24: JV curves* under red and blue light illumination for (a) cell A, (b) cell B and (c) cell C.

To deepen in the impact of spectral wavelength and temperature behavior of cell B's *FF*, IV(T) measurements were carried out under red and blue light separately, followed by subsequent IV measurements at the highest temperature of the interval of interest (323 K). Behaviors can be seen in Figure 25. Under blue light exposure, *FF* values followed the expected decaying trend with temperature, and stayed similar over the subsequent high temperature IV measurements. On the other hand, measurements taken under red light showed an increasing *FF* with

*IV(λ) measurements made by Ndoukoue Kader.

49

increasing temperature, and after the subsequent IV measurements taken at high temperature, *FF* values kept increasing after more than one and a half hours of red-light exposure. It must be noted that *FF* values under red light were always lower than under blue light. This suggest that blue light has a beneficial effect that enhances *FF* overall and makes the cell stable, while red light shows a rather detrimental effect on *FF* but with a constant enhancement over time. This indicates that, under red light, the solar cell is under the influence of a transport barrier for carriers that is strongly affected by temperature and slightly minimizes its effect over time, although always present, as can be seen in the corresponding resistance vs voltage plots under blue and red-light conditions (Figure 25c-f).
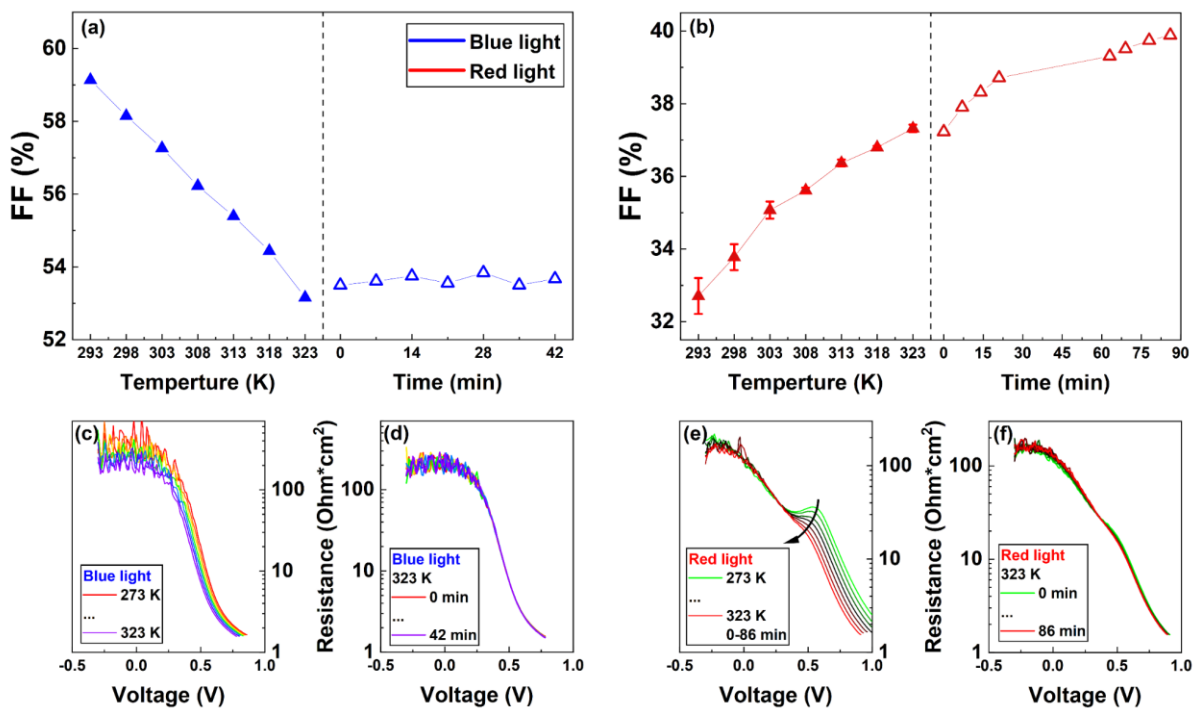
Figure 25: FF(T) behaviors for cell B under (a) blue and (b) red light illuminations. After reaching the highest temperature of the interval, subsequent IV measurements were taken at that constant temperature. Resistance vs voltage plots under blue light at different temperatures (c) and at 323 K through different times (d), and under red light at different temperatures (e) and at 323 K through different times (f).

Further IV(T) hysteresis measurements with red light for cell B were performed. Now, a larger number of cycles were implemented to look for a stability condition. Results are shown in Figure 26. It can be seen that V_{oc}, *FF* and P_{mpp} show consistent improvement as cycles pass. Nevertheless, parameters still show way lower values than if measured with blue light. This suggests that red light soaking solely would not reach a stable condition that compares with the state that blue light produces.

Figure 26: (a) V_oc, (b) FF and (c) P_mpp behaviors of cell B through five temperature hysteresis cycles. Measurements were taken under red light illumination. Arrows indicate the direction of the first cycle.

$\beta_{FF,rel}$ were calculated for all temperature runs and shown in Figure 27. Here, a trend appears for $\beta_{FF,rel}$ obtained from measurements taken in each *T* change direction. When measuring from low to high *T*, $\beta_{FF,rel}$ is generally better but worsens as cycles pass. On the other hand, $\beta_{FF,rel}$ obtained from high to low *T* shows worse values but remain relatively constant. Since red light is exclusively absorbed in the absorber layer, this indicates that the stable state caused by blue photons is produced due to their absorption in any of the front layers (buffer, *i*-layer and/or window).
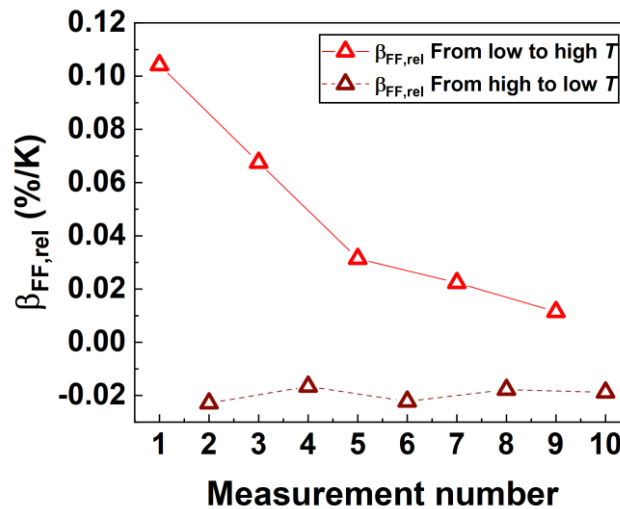
Figure 27: $\beta_{FF,rel}$ for cell B under red light.

Following the previous hint regarding absorption of blue photons in the front side of the solar cell, EQE measurements were performed under red and blue light bias for all three cells to account for their effect on carrier collection. Results are shown in Figure 28. It becomes remarkably evident, that cells A and C behave essentially the same under both light biases. On the contrary, cell B presents a carrier collection enhancement under constant red-light illumination, showing EQE values over 100% at wavelengths bellow 600 nm. Under blue light bias, cell B again shows a stable behavior in the collection efficiency, comparable to the other

two cells. Since samples were not light soaked prior to the measurements, results support the claim that the stable state in the solar cell is achieved by blue light absorbed in the large band gap layers of the solar cell and that this effect occurs very rapidly. Therefore, the absorption of blue photons in the front layers appear to have a double effect: one fast, as seen here, and another much slower while being part of white light, as seen in IV(*T*) hysteresis measurements from Figure 22.
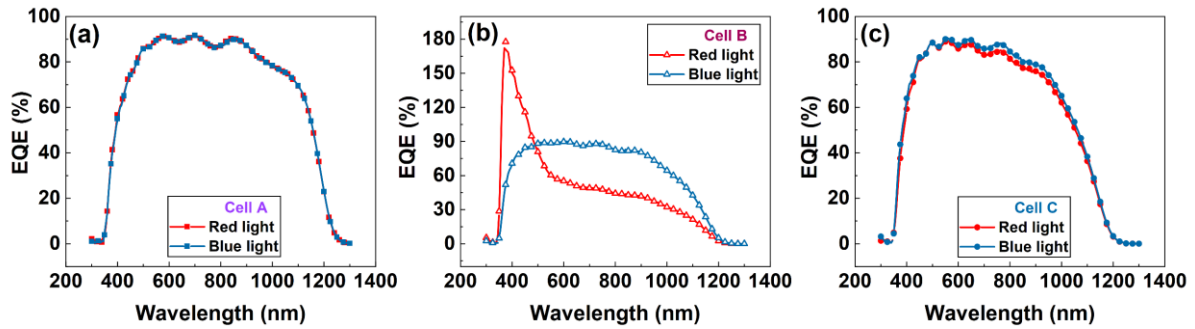
Figure 28: EQE measurements* taken under red and blue bias light for (a) cell A, (b) cell B and (c) cell C.

To further examine the metastability effect at lower temperature, IV(*T*)-hysteresis measurements under red light were also performed in a lower temperature range (i.e from 100 to 150 K with steps of 5 K). From Figure 29, it can be seen that the enhancement in the change of V_{oc}, *FF*, P_{mpp} parameters over multiple temperature cycles indeed is no longer present, leaving only a small hysteresis effect that becomes almost negligible after each cycle. It can be infered that not only red light but also temperature is fundamental to activate the metastable behavior in the solar cell.
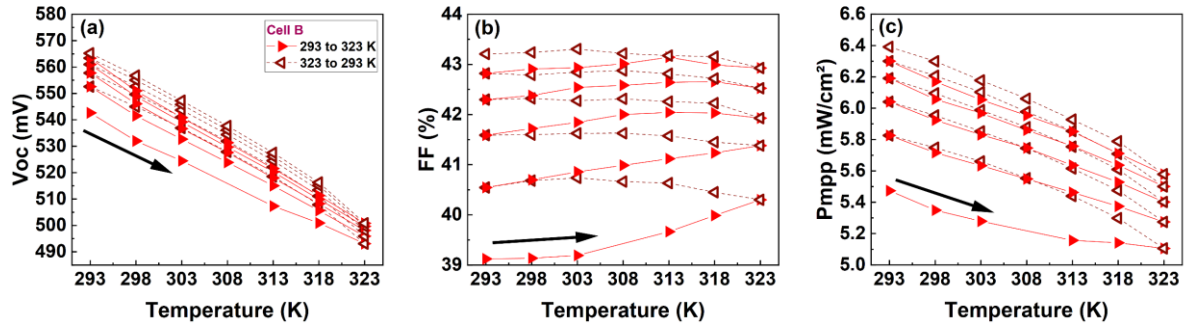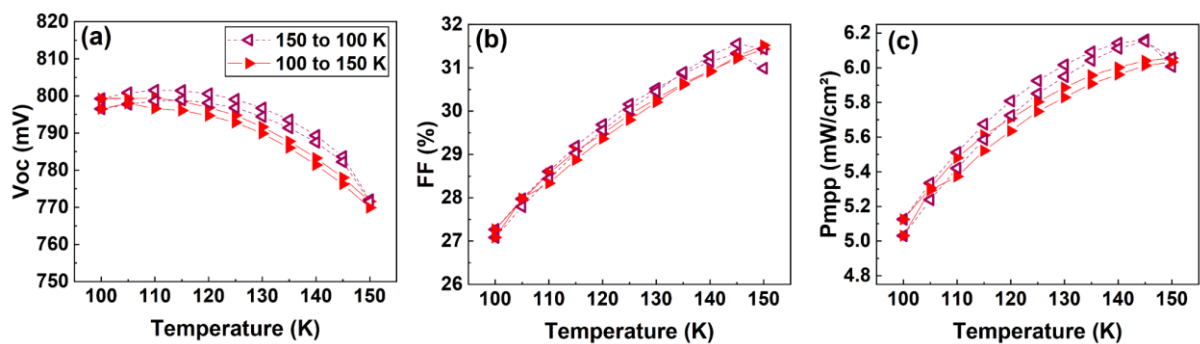

Figure 29: (a) V_{oc}, (b) FF and (c) P_{mpp} behaviors of cell B through two low temperature hysteresis cycles. Measurements were taken under red light illumination.

CV measurements were further performed at 120 K on all three samples to account for the change in N_A after different light-bias treatments. Samples were initially brought from room temperature to 120 K in dark conditions, then a CV measurement was taken from -0.8 to 0.5 V. After the first measurement, the sample was exposed to red light and a reverse bias of -2 V for

*EQE measurements made by Tash Motsi.

ca. 20 minutes. This treatment is commonly called Red-on-bias (ROB), after which another CV measurement was performed in the dark. Finally, the sample was exposed to white light for ca. one hour, followed by a third CV measurement in the dark. The corresponding Mott Schottky plots are shown in Figure 30, from where N_A values were extracted. N_A values in the front region of the absorber were extracted from the slope between -0.2 and 0 V.
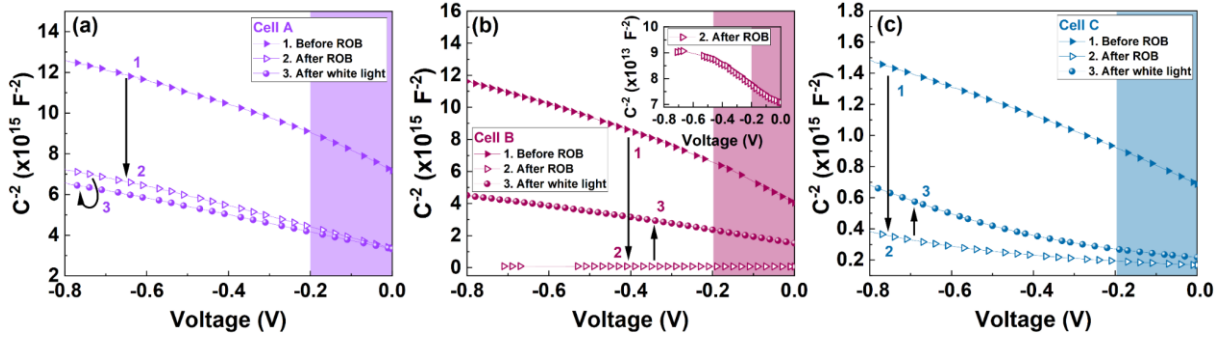
Figure 30: Low temperature CV measurements for (a) cell A, (b) cell B and (c) cell C. Inset in (b): magnification of CV measurement after ROB treatment. Arrows indicate the order in which measurements were taken. Colored rectangles indicate the data region from which N_A in the front region of the absorber was extracted.

In Table 3, the N_A values of all cells are shown for each of the three conditions described previously. For all cells, N_A values increased after ROB treatment, but cell B presented the most remarkable increment, as N_A raised more than two orders of magnitude. This trend is followed by cell C, which showed an N_A increment of one order of magnitude, and lastly by cell A, whose N_A value increased only by a factor of ~2 after ROB treatment. Finally, after exposure to white light, the stronger effect is seen in cell B, which decreased its N_A value by two orders of magnitude. Cell C also decreased its N_A value by a factor of ~2. Finally, cell A showed a slight increase in N_A.

Table 3. N_A values for all three cells for all used treatments. N_A values were extracted from regions close and far from the buffer/absorber heterointerface.

	N_A (cm^{-3})		
	A	**B**	**C**
Before ROB	$1.49*10^{15}$	$1.14*10^{15}$	$1.20*10^{16}$
After ROB	$2.63*10^{15}$	$5.22*10^{17}$	$1.08*10^{17}$
After white light	$3.33*10^{15}$	$3.69*10^{15}$	$5.27*10^{16}$

These results indicate that an increase in N_A can be provoked at low temperatures under the effect of red light and reverse bias conditions and that not in all cases N_A can be recovered by

exposing the cell to white light. This suggests that the nature of the metastable characteristics on each of the cells could stem from similar type of defects, but with different concentrations, and that the only set of concentrations affecting the temperature coefficients at room temperature range is the one seen in cell B.

6.3 Discussion

As already stated in chapter 1, it is quite sophisticated to experimentally determine the origin as well as the type of defects that causes the metastable behavior. The red kink effect observed in the IV(λ) characteristics of cell B results in the deterioration of *FF* under the exposure to photons that are exclusively absorbed in the CIGS layer. It is commonly agreed that this effect is a result of a transport photo-barrier in a solar cell interface [53]. Since the only structure layer that is modified between cell A and cell B is the absorber, and between cell B and cell C is the buffer layer, the logical conclusion is to infer that the photosensitive barrier is present somewhere in the buffer/absorber heterointerface.

From the analysis of the IV(T, λ) measurements taken for cell B (Figure 25), it is clear that blue light makes the cell very stable through the whole set of measurements since *FF* remained constant after continuous measurements at high T, as well as showing overall higher *FF* values. On the other hand, with red light, *FF* improves with subsequent measurements, but they do not appear to reach an equilibrium condition, indicating that the blue component of white light is a cause of the temperature coefficient stability. As temperature hysteresis cycles are measured (Figure 26), the overall performance of the cell improves, although slightly. This could be attributed to an increase of N_A due to red light (discussed later).

EQE measurements under red and blue light bias supported this argument further (Figure 28), as cell B showed EQE values over 100% at wavelengths under 600 nm only with red-light bias. This effect indicates the presence of a photosensitive barrier that impedes carrier collection under the absence of blue light. It is expected that this barrier is found at the buffer/absorber interface, as this is the only modified region in cell B. Commonly, it is described as the effect of the buffer/absorber conduction band offset due to decreased donor density in the buffer, leading to a detrimental built-in electric field in the junction [133]. Red light biased cells would generate carriers exclusively in the absorber layer, but as there is a strong effect of the photosensitive barrier, not all of these photogenerated carriers will be collected. On these measurements, the probe wavelength sweeps from short wavelengths towards long wavelengths. When the probe reaches wavelengths under 600 nm, a large EQE spike is

presented, indicating that the blue light coming from the probe is the responsible of the barrier reduction. This phenomenon is known as buffer photoconductivity and it is observed when the buffer in a solar cell presents deep acceptor levels that trap electrons from the donor levels, thereby decreasing the overall donor doping density, decreasing the built-in electric field, and maximizing the barrier effect in the buffer/absorber conduction band offset [133], [151]. As blue photons are absorbed in the buffer, holes generated are used to detrap the mid-gap electrons, causing a recovery of the donor doping density, enhancing the built-in electric field, and reducing the photobarrier effect. It is then clear, that the buffer of cell B presents a photoconductive effect. Nevertheless, this effect is not enough to explain the overall improvement of solar performance in cell B since the photoconductivity effect showed to be instantaneous, while the overall metastable effect seen did not equilibrate under white light. Therefore, the sole buffer photoconductivity effect is not enough to explain the metastable behavior observed.

Low *T* IV(*T*) hysteresis measurements with red light taken for cell B showed that the metastable behavior shown at high *T* was practically gone, indicating that, apart of red light, high temperatures are also necessary to induce the metastable behavior.

Over the last years, diverse explanations have been given to understand the phenomenology of metastabilities in CIGS solar cells. One of the most recognized, is the so-called V_{Cu}-V_{Se} divacancy model, proposed by Lany and Zunger [52]. This divacancy defect presents amphoteric behavior, i.e. can show properties of donor and acceptor depending on the In-In distance for CuInSe$_2$ (CIS) absorbers and on the Ga-Ga distance for CuGaSe$_2$ (CGS) absorbers. In order for it to transform from its *shallow donor* configuration into the *shallow acceptor* configuration, three requirements must be simultaneously satisfied: (1) The Fermi level must be above E_V+0.19 eV for CIS absorbers, and above E_V+0.32 eV for CGS absorbers. (2) a thermally activated barrier *ΔE₁* of ~0.1 eV (~50 K) must be overcome. (3) Successful capture of *one* electron. This reaction can be expressed as

$$(V_{Se} - V_{Cu})^+ + e \xrightarrow{\Delta E_1} (V_{Se} - V_{Cu})^- + h \qquad (6.1)$$
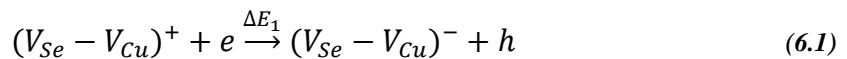
The inverse transformation (from shallow acceptor to shallow donor) also has three requirements that must be simultaneously fulfilled: (1) The Fermi level must be below E_V+0.19 eV for CIS absorbers, and below E_V+0.32 eV for CGS absorbers. (2) A thermally activated barrier *ΔE₂* of ~0.35 eV (~200 K) must be overcome. (3) Successful simultaneous capture of *two* holes. This transformation reads as

$$(V_{Se} - V_{Cu})^- + 2h \xrightarrow{\Delta E_2} (V_{Se} - V_{Cu})^+ \qquad \text{(6.2)}$$

In Figure 31a, a simplified configuration coordinate diagram is shown to describe the transformation behavior of this divacancy complex in CIS absorbers. According to this model, the donor configuration presents the most stable state. Supposing an electron is photogenerated and captured by the complex, this then transforms into an intermediate state $(V_{Cu}\text{-}V_{Se})^0$, which afterwards can overcome a thermally activated energy barrier ΔE_1 to transform and relax into the acceptor configuration. The opposite transformation occurs by overcoming the thermally activated energy barrier ΔE_2 while simultaneously two holes are captured by the complex. If the electron quasi-Fermi level is high enough ($\sim E_v + 1$ eV) the defect in shallow acceptor configuration can further transform into a *deep* acceptor configuration. This is expected to occur in the front surface of the absorber, where $E_{F,n}$ takes the highest value [52].
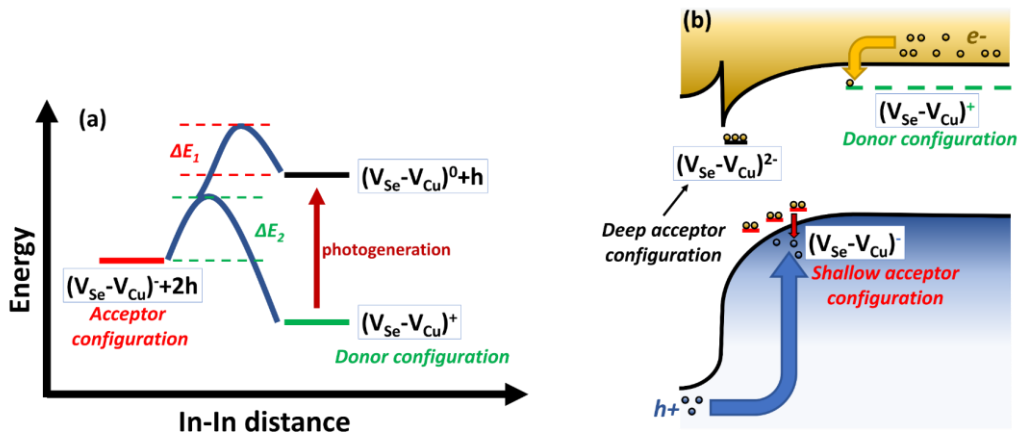
Figure 31: (a) Simplified configuration coordinate diagram for the different relative charge states of the V_{Cu}-V_{Se}. (b) Electron trapping (yellow arrow) and detrapping (blue arrow) under the presence of both red and blue light. The former photogenerates electrons in the absorber, which are captured by the complex. The later photogenerates holes in the buffer, which drift towards the absorber and recombine with previously trapped electrons.

Nevertheless, this model is insufficient to describe the observed changes in N_A values before ROB, after ROB and after white light soaking treatments made during low T CV measurements. At temperatures below 200 K, the V_{Cu}-V_{Se} acceptor-to-donor transformation is inhibited due to insufficient thermal energy to overcome the barrier ΔE_2. Under this condition, white light should not produce a decrement in N_A (as in cell A). Instead, it should increase N_A (as more photogenerated electrons could be further trapped), or if complexes are already saturated, maintain N_A invariant. On the contrary, this is the case observed for cell B (and to a lesser extent on cell C), which shows a decrement of N_A by almost two orders of magnitude after white light exposure at low T. This indicates that there is another mechanism present that does not require high temperatures, i.e., does not have a thermally activated mechanism that outcomes in a

decrease of N_A. This phenomenon is known as ROB metastability, and has been attributed to a different complex, the so-called In_{DX} or Ga_{DX} defects, modeled as well by Lany and Zunger [56]. Similar to the V_{Cu}-V_{Se} divacancy, a DX defect also has the amphoteric property of transforming from a shallow donor configuration to a *deep* charge-neutral configuration. Here, these complexes are modeled as Frenkel pairs, where an interstitial In (or Ga) atom adjacent to a V_{Cu} defect (In_{DX}, deep charge-neutral state) can recombine to form the In_{Cu} antisite (shallow donor configuration), and vice versa. If these defects are surrounded by neighboring V_{Cu}, they can form complexes with them, so that their DX configuration presents acceptor characteristics. For example, a complex consisting of one DX defect and a single V_{Cu} can transform from donor to acceptor configuration $(In_{Cu} - V_{Cu})^+ \leftrightarrow (In_{DX} - V_{Cu})^-$ if the Fermi level is ~1.11 eV above the valence band maximum, which can happen in the front surface of the absorber [56]. This configuration can be found in large quantities, as V_{Cu} defects are abundant [56]. In CIGS absorbers, the In_{Cu} donor configuration would represent an overall decrease of N_A, as it compensates the intrinsic acceptor V_{Cu}, which is the main contributor to the *p*-type conductivity of the material. While in DX configuration, this complex would increase N_A.

The deep charge neutral state-to-shallow donor configuration transformation can occur by either (1) capturing holes and lattice relaxation, expressed as

$$In_{DX}^0 + h \rightarrow In_{DX}^+ \rightarrow In_{Cu}^+ \qquad (6.3)$$

(2) By absorption of light and subsequent relaxation, as

$$In_{DX}^0 \rightarrow In_{DX}^+ + e \rightarrow In_{Cu} \qquad (6.4)$$

(3) By overcoming a thermally activated barrier (~0.32 eV for CIS absorbers) and simultaneously emit an electron to the conduction band.

The first transformation mechanism does not require to overcome any thermally activated energy barrier, and therefore it could occur even at low *T* [56]. Under this premise it is understandable, then, that cell B had shown this effect after being white light soaked during low *T* CV measurements, causing a strong decrement in N_A. Around room temperature conditions, it is expected that the third mechanism of In_{DX} (or the acceptor complex) to In_{Cu} conversion occurs at higher rates due to more available thermal energy. This translates in higher density of DX centers in shallow donor configurations. Consequently, the effective N_A is compensated.

Now, under the consideration of all three (i) photoconductivity effect, (ii) the presence of V_{Cu}-V_{Se} and (iii) (In_{DX}-V_{Cu})⁻ complexes, it appears now possible to describe the metastable behavior of *FF*(*T*) of cell B under red and white light. To illustrate this, band diagrams under different

light and temperature conditions are shown in Figure 32 and Figure 33. The explanation is made under the argument of a conduction band barrier present in the absorber. This type of barrier is commonly created due to a p^+ layer in that region, which can be caused by a large density of $(In_{DX}-V_{Cu})^-$ or $V_{Cu}-V_{Se}$ complexes in acceptor configuration.

After light soaking at room temperature, an induced quasi-equilibrium is reached (Figure 32b and Figure 33b) and both complexes will be present with a corresponding configuration and corresponding densities, according to the system conditions, i.e. electron quasi-Fermi level position, temperature, and carriers density. A modification on these conditions, i.e. temperature, will result in a change in the equilibrium concentrations of each defect configuration, affecting the solar cell *FF*.

First, *FF*(*T*) hysteresis cycles under red light illumination are discussed. A certain initial value for the height of the p^+ layer barrier after red light soaking at room temperature is considered. Through the first half of the first hysteresis cycle (first *T* ramp up), *FF* is observed to slightly increase with temperature (Figure 32a, state *I* to *II*). This is attributed to the result of two beneficial and one detrimental mechanisms: (1) enhanced electron emission from $(In_{DX}-V_{Cu})^-$ states to the conduction band due to higher temperature, which decreases the height of the p^+ layer. (2) Increased transformation of $V_{Cu}-V_{Se}$ complexes to acceptor configuration deeper in the absorber, which raise the conduction band up relative to the p^+ layer, decreasing its barrier effect (Figure 32c). The strongest effect of both mechanisms will be observed at the highest temperature reached (323 K). (3) Electron capture in $(In_{DX}-V_{Cu})^-$ states (detrimental) will counteract the effect of the previous two mechanisms, rising the p^+ layer barrier height. Through the first *T* ramp down (back at 293 K), *FF* values improve due to the decreased barrier effect achieved during the previous half temperature cycle. Nevertheless, in the last two points of the second half hysteresis cycle, *FF* deteriorated (Figure 32a, state *III*). This indicates that the $(In_{DX}-V_{Cu})^-$ electron emission rate reduces when temperature is decreased, but the electron capture in $(In_{DX}-V_{Cu})^-$ complexes continued, slightly recovering p^+ barrier height (Figure 32d). A repeating trend of this behavior can further describe the remaining hysteresis cycles, slowly reaching an equilibrium condition.

Figure 32: (a) FF(T)hysteresis cycles under red light illumination, from Figure 26b. Band diagram of cell B at (b)state (I), (c) state (II), and (d) state (III). Band diagrams represent P_{mpp} condition.

In the following, *FF(T)* hysteresis cycles under white light illumination are discussed. Again, after white light soaking, an initial value for the height of the p^+ layer barrier is expected, as well as improved *FF* values, due to the photoconductivity effect of the buffer. Under white light, three beneficial and two detrimental mechanisms are involved: (1) electron emission from $(In_{DX}-V_{Cu})^-$ states to the conduction band, decreasing p^+ layer barrier height, (2) bulk acceptor increase due to $V_{Cu}-V_{Se}$ complexes transforming to acceptor configuration, (3) buffer photogenerated hole capture in $(In_{DX}-V_{Cu})^-$ states, further decreasing the p^+ layer barrier height. (4) electron capture in $(In_{DX}-V_{Cu})^-$ states (detrimental), increasing the p^+ barrier, and (5) hole capture in bulk $V_{Cu}-V_{Se}$ complexes (detrimental), lowering the conduction band relative to the p^+ barrier, increasing its effect (Figure 33c). Through the first *T* ramp up, *FF* decreases with a smaller rate compared to the following *T* ramps (Figure 33a, state *I* to *II*). This is attributed to enhanced $(In_{DX}-V_{Cu})^-$ electron emission, formation of $V_{Cu}-V_{Se}$ in acceptor configuration, both increasing with temperature, and photogenerated holes captured by $(In_{DX}-V_{Cu})^-$ states, further decreasing the p^+ layer barrier height. Through the first *T* ramp down, *FF* values increase as temperature decreases, closely resembling the expected behavior. During the second *T* ramp up, *FF* values match with the previous ramp down values until ~308 K, where the trend splits

towards higher *FF* values (Figure 33a, state *IV*). Again, this indicates that higher temperatures can further decrease the present p^+ layer barrier due to the previously described mechanisms. The overlap from 293 K to ~308 K is attributed to the reduced $(In_{DX}-V_{Cu})^-$ electron emission and an equilibrated effect of electron capture and hole capture mechanisms. After 308 K, $(In_{DX}-V_{Cu})^-$ electron emission and $V_{Cu}-V_{Se}$ electron capture rates raises again considerably, enhancing *FF* with increasing temperature.
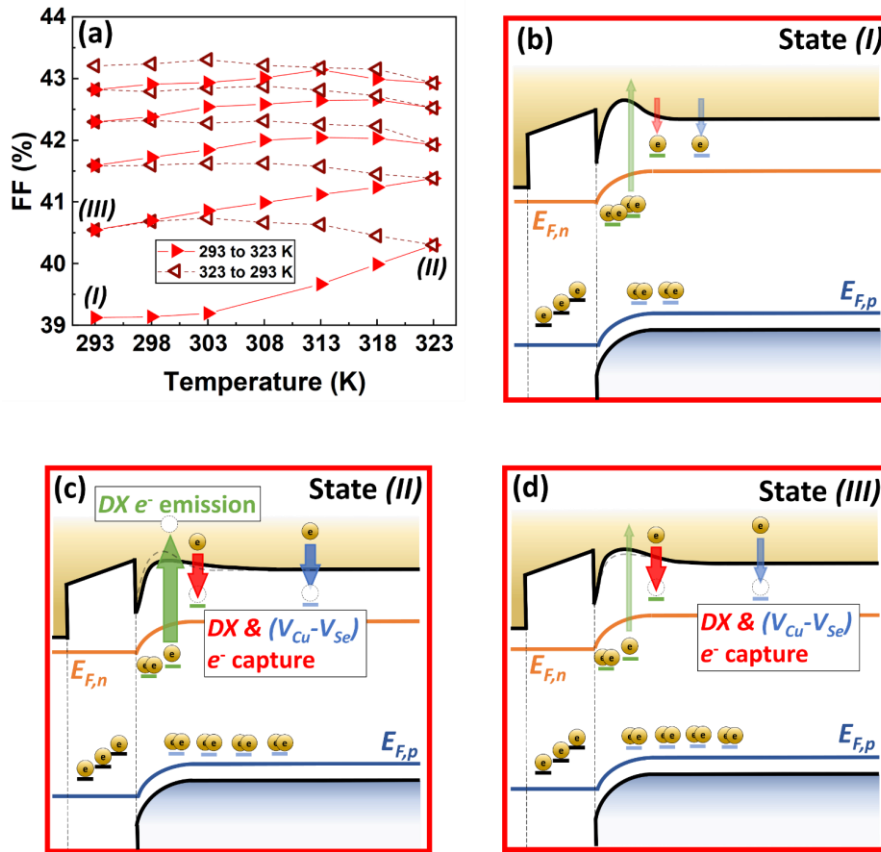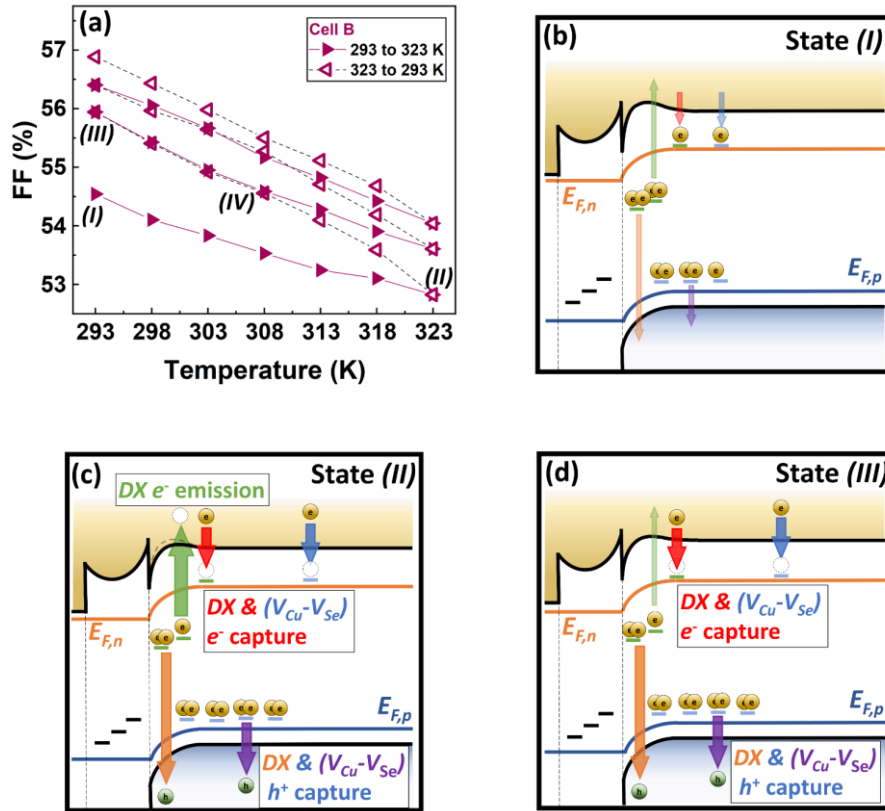

Figure 33: (a) FF(T)hysteresis cycles under white light illumination. Band diagram of cell B at (b)state (I), (c) state (II), and (d) state (III). Band diagrams represent P_{mpp} condition.

Since all CIGS solar cells are expected to present $V_{Cu}-V_{Se}$ divacancy complexes due to the relatively similar abundant nature of both V_{Se} and V_{Cu}, the discussion shifts now towards explaining the source of the particular set of defects present in cell B. As proposed previously, the source of this behavior appears to come from the buffer/absorber interface under these particular sets of buffer and absorber. As cells A and C did not show this metastable behavior, it becomes clear that for cell B it must come from both the In_xS_y buffer, along with the (Ga+) CIGS absorber together. It is known that, in the presence of Ga, the antisite In_{Cu} does not form as easy, since Ga_{Cu} antisites present larger formation energies than In_{Cu} [152]. These observations seem to contradict the fact that cell B presents a large density of In_{DX} complexes.

Nevertheless, it can be expected that diffusion mechanisms could be involved between the two layers that promote the formation of such complexes.

Scanning Electron Microscope (SEM) micrographs for the bare absorbers of cells A and B were taken and shown in Figure 34. It can be seen that for the absorber of cell B (Figure 34b), the surface shows a much rougher texture compared to cell A's absorber (Figure 34a), where the amount of Ga is less. It is proposed that the rougher the surface, the larger the overall contact area between the absorber and the buffer. Consequently, an increase in the overall elemental (inter)diffusion between the absorber and the buffer is expected. It is perceived that the terraces' sizes are bigger for cell A compared to cell B. Therefore, the reason behind the elemental diffusion between absorber and buffer could be attributed to the higher presence of Ga in the absorber. These data are supported by another cell configuration that showed similar behavior for the Ga increase in the absorber (see supplementary information, Figure S 2).
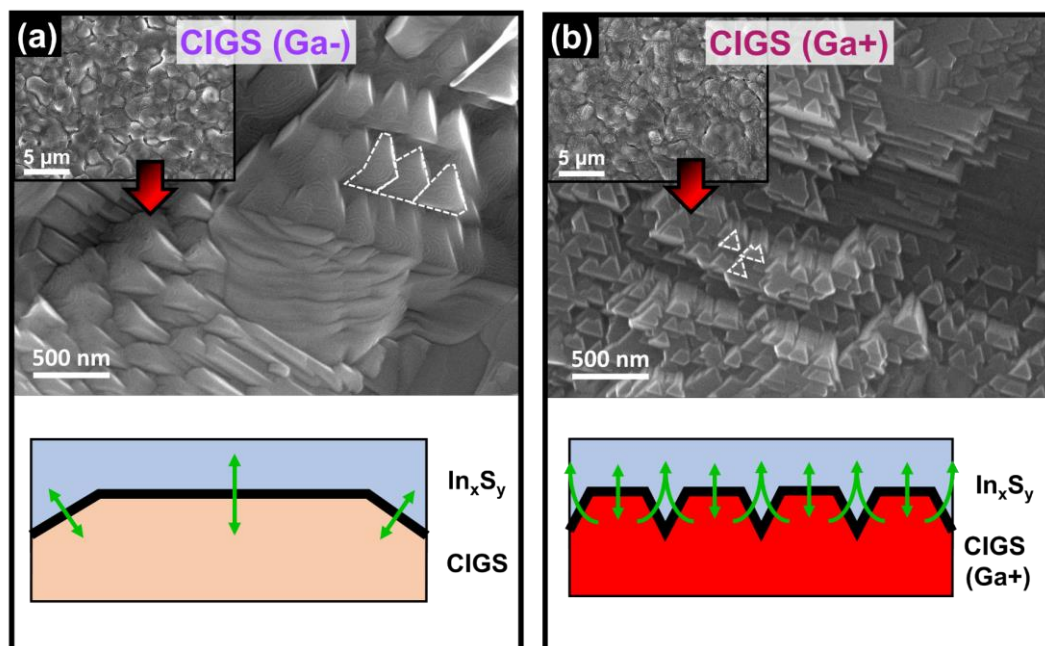
Figure 34: SEM micrographs* of the bare absorber surface of (a) cell A and (b) cell B before buffer deposition. A graphical representation of the overall effective contact area between absorber and buffer illustrates the elemental diffusion capacity in each cell due to differences in surface roughness.

TEM/EDX analysis were performed to infer the elemental diffusion between layers. In Figure 35a, a lamella sample from cell B is shown, along with the profile line region for EDX measurements (Figure 35b). The normalized at% of each element is shown in Figure 35c. Similar measurements were made on a lamella of cell C. Although measurements were made under uncalibrated conditions, they still help to infer the depth through which some elements appear to diffuse. A comparison between Cu and Se atoms show that Cu diffuses towards the

*SEM micrographs taken by Dr. Ulrike Künecke, Dr. Matthias Schster and Dr. Peter Wellemann, Erlangen University

front side of the solar cell. In fact, this diffused atoms can lead to Cu vacancies in the absorber, which can be occupied by another element. Similarly, the Cu diffused to the In_xS_y buffer could occupy In vacancies, forming $Cu_{In.}$antisites, which are expected to behave like compensating mid-gap acceptor levels [107]. This would explain the notorious photoconductivity effect that led to EQE values over 100% under red light bias. This elemental diffusion could be the source of the perceived density of DX states in cell B, as well as the buffer photoconductivity effect. Furthermore, this interdiffusion seems to be catalyzed by the rougher surface seen in cell B. This would explain the fact that cell A is not metastable, but cell B is.
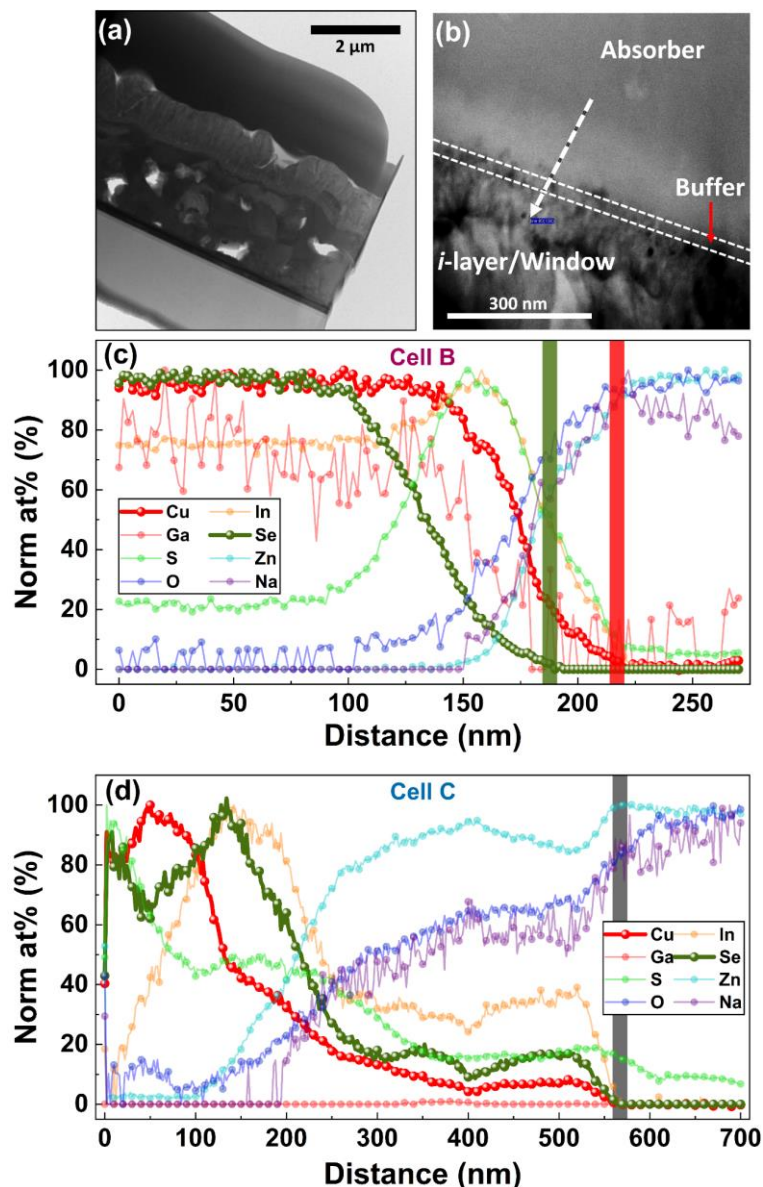
Figure 35: (a) SEM micrograph of the lamella* taken from cell B. (b) TEM micrograph** of the region of the lamella where an EDX line scan was performed. (c) Normalized at% distribution along the scan line of cell B. Green and red bars indicate qualitatively the maximum diffusion position of Se and Cu, respectively. (d) Normalized at% distribution along the scan line for the lamella of cell C. Gray bar shows the limiting position of absorber elements. Atomic percentages are normalized to the highest measured value along the profile.

As Cu is able to diffuse through the In_xS_y due to the absorber roughness, it should be expected that a similar effect occurred in cell C. Since both cells have nominally the same absorber, their surface roughness should also be similar. Nevertheless, the Zn(O,S) buffer of cell C appeared to be more resilient towards Cu interdiffusion, possibly explaining the reason as of why no other cell with Zn(O,S) buffer (cells D to I) with different structure presented buffer photoconductivity in a manner like cell B. In Figure 35d, the EDX elemental profile on a lamella of cell C is shown, where elements present in the absorber are no longer detected at the same position, indicating negligible layer interdiffusion. This interdiffusion resilience of the Zn(O,S) buffer could be due to the presence of the heavier Zn atoms in the lattice, which appear less mobile than Cu atoms. Nevertheless, the actual effect that Cu diffusion would have on Zn(O,S) buffers is expected to not be as detrimental. For In_xS_y buffers, for example, a Cu_{In} antisite, which would behave as a compensating acceptor level, would present two available states to trap electrons. On the contrary, for Zn(O,S) buffers, diffusion of Cu on this layer could produce Cu_{Zn} antisites instead. This defect also acts as a compensating acceptor level but would only contribute a single level for electron trapping, since Cu would be present as Cu^{+1}. Suja *et al*. showed that Cu_{Zn} defect in ZnO films presented a shallow acceptor level at 0.15 eV above the valence band, making this state difficult to act as an electron trap and more as a compensating acceptor [153]. In short, the negative impact of Cu antisites in In_xS_y can be double as detrimental than in Zn(O,S), giving another explanation as to why Zn(O,S) didn't present such metastable behaviors.

6.4 Summary

An intriguing aspect of CIGS solar cells is an improvement and stability in solar cells' parameters with light soaking conditions. The presence of this effect has been ascribed to various mechanisms, for instance, an amphoteric V_{Se}-V_{Cu} divacancy complex, which can transform from shallow donor to shallow acceptor configuration, increasing N_A through the absorber, or to In_{Cu} DX defect centers, which undergo a shallow donor to deep acceptor transition, forming a p^+ layer conduction band barrier close to the absorber front surface.

In this chapter, the effect of $\beta_{FF,rel}$ metastability has been discussed in the frame of different CIGS layer configurations. It was observed from SEM micrographs that increasing the Ga amount in the CIGS absorber layer leads to a rougher absorber surface, thereby enhancing the elemental diffusion from the absorber to the buffer layer due to increased effective surface area. It was found out using TEM/EDX analysis, that indeed Cu diffuses from the CIGS absorber to the In_xS_y buffer, whereas with similar absorbers, Zn(O,S) buffer showed a resilient response

towards Cu diffusion. The diffusion of Cu into the In_xS_y buffer led to the creation of mid-gap acceptor levels that trapped electrons, decreasing the overall buffer doping density. This detrimental outcome causes the buffer photoconductivity effect under blue light, confirmed by red bias EQE values over 100% at wavelengths below 600 nm. This effect changes the conductivity of the buffer upon blue light illumination and yielded an enhanced carrier collection due to the doping density recovery.

The increase in net acceptor density in the absorber bulk of cell B upon red light illumination led to an increment of V_{oc}, *FF* and P_{mpp}. This effect is known as Persistent photoconductivity that can stem from V_{Se}-V_{Cu} complexes. DX states appeared to act as acceptors close to the absorber front surface, counteracting the effect of increasing temperature on V_{Se}-V_{Cu} complexes, which tend to transform to acceptors. Since these two mechanisms, having opposite impacts on the cell performance, are also light and temperature sensitive, light soaking at higher temperatures would be needed to stabilize the cell properly. This double dependence can be the reason as why cell B did not show explicitly the metastable behavior while light soaking it at room temperature (cf. Figure 13). This could also explain the stability of $\beta_{FF,rel}$ over temperature cycles using white and red-light illumination, and sheds light on the influence of these defects on the temperature coefficients stability. It was shown that the metastability of $\beta_{FF,rel}$ disappeared at low *T*, which confirms that the metastable effect caused in the bulk of the absorber is attributed to V_{Se}-V_{Cu}. Finally, it could be observed that the particular selection of absorber and buffer combination play a fundamental role in the metastability of the solar cell $\beta_{FF,rel}$ due to complex microscopic defect distributions along both sides of the heterointerface. In order to avoid this effect, buffer materials with high atomic interdiffusion resilience should be implemented, or in the worst case, materials that minimize the detrimental effect of defects caused from adjacent layer elements.

Chapter 7 Low light behavior of temperature coefficients and parameters of CIGS solar cells

In this chapter, investigations on the performance of different CIGS solar cell structures under low light conditions were made. The dominant recombination location in different CIGS structures was determined at different light intensities. The relation between dominant recombination location within the solar cell and temperature coefficients are discussed. The resilience of low light performance was studied in terms of the corresponding layer modification. A method to identify the dominant recombination location for graded solar cells is presented.

7.1 Methods

The IV and IV(T) measurements* as function of intensity were realized using the previously described setups in the methodology chapter, with the aid of different optical density filters. Using the IV setup, it becomes possible to have insights on the parameters' intensity dependence, in addition to the low light behavior performance of different solar cells' parameters. The light intensity was varied from 1 sun to ~0.2 suns of light intensity, always keeping a constant cell temperature of 25°C. Similarly, the IV(T) measurements were performed at same range of light intensities in order to study the intensity dependence of solar cell parameters' temperature coefficients. IV(T, λ) measurements were performed with light of λ> 600nm ("red light") and λ between. ~300 and ~600 nm ("blue light"). For all IV(T) measurements, the E_A was extracted by extrapolating V_{oc}(T) to zero K.

$E_{g,min}$ values for all cells were obtained from EQE measurements. Using the W_{SCR} obtained from CV measurements along with the band gap profiles extracted from GDOES measurements for each cell, it was possible to locate the $E_{g,min}$ position in the profile. A slight correction was done by subtracting from the GDOES E_g profile the difference between $E_{g,min}$ obtained from GDOES and $E_{g,min}$ of EQE. Afterwards, E_g values at the absorber front interface ($E_{g,IF}$) were inferred from the corrected GDOES profile.

In order to properly extract E_A values unaffected by R_{sh}, the one diode model was implemented. Commonly, the current-voltage characteristics of a solar cell behaves following the one diode model expressed with equation (3.14).

*IV(T,φ).measurements were made in collaboration with Mohamed Elshabasi.

65

Chapter 7 Low light behavior of temperature coefficients and parameters of CIGS solar cells

Under open circuit conditions, and expressing J_0 as $J_0 = J_{00}e^{\frac{-E_A}{mkT}}$ [62], equation (3.14) can be rewritten as

$$V_{oc} = E_A + \frac{mkT}{q} * \ln\left(\frac{J_{sc} - \frac{V_{oc}}{R_{sh}}}{J_{00}}\right) \qquad (7.1)$$

Where J_{00} is a saturation current prefactor, usually independent of temperature. If R_{sh} is not large enough, E_A cannot be simply extracted by extrapolating $V_{oc}(T)$ measurements to 0 K, as commonly seen in literature [23], [154].

By implicitly differentiating equation (7.1) respect to temperature, it gives

$$E_A = V_{oc} - T\frac{dV_{oc}}{dT}\left(1 + \frac{\frac{mkT}{q}}{J_{sc} * R_{sh} - V_{oc}}\right) \qquad (7.2)$$

where R_{sh} is extracted by obtaining the inverse slope of the JV curve at reverse bias [135].

Similarly, the ideality factor m and J_0 are extracted from the one diode model by obtaining the slope of a $\ln\left(J_{sc} - \frac{V_{oc}}{R_{sh}}\right)$ vs V_{oc} and the Y-axis intercept from JV curves taken at different illumination conditions, respectively, following

$$\ln\left(J_{sc} - \frac{V_{oc}}{R_{sh}}\right) = \frac{q}{mkT}V_{oc} + \ln(J_0) \qquad (7.3)$$

7.2 Results

J_0, V_{oc}, FF and η parameters were extracted and normalized to their corresponding STC values for different illuminations. In Figure 36, the behaviors of V_{oc}, FF and η parameters of all studied cells at different light intensities are shown. Among all cells, Cell I presents the strongest FF and η decrease at low illuminations, while cell C shows a rather resilient behavior for those parameters. Also, cell C shows the largest R_{sh} values at different light intensities, while cell I presented the lowest ones, indicating that their light behavior is determined by their R_{sh} values (Figure S 3a). From Figure 36a, the V_{oc} behavior of cell I present a considerable decrease at low illuminations, whereas the rest of the cells seem to decrease with a similar rate. Additionally, J_0 of cell I shows a strong increment at lower illuminations in comparison with the rest of the cells (Figure S 3b). It is worth noting that the solar cells used for this study are not laminated

as mentioned before in the experimental section, which explains the η values range extracted. Normally, encapsulated solar cells show a relatively higher η values.
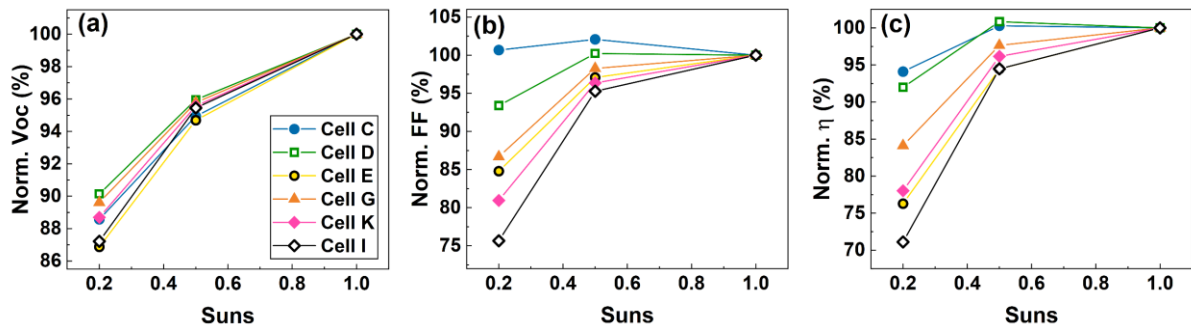
Figure 36: (a) V$_{oc}$, (b) FF, and (c) η behaviors under different light intensities. Parameters were normalized to their respective values at 1 sun illuminations.

In order to have a closer look into the role of *i*-layer on the performance' resilience, IV(*T*) measurements under white, red and blue light were carried out. E_A values under different white light intensities for cells C and D are quite similar (Figure 37a and b). Since window layers are transparent to long wavelengths, under red light conditions, charge carriers are expected to be generated exclusively in the cell's absorber. Under red light, the E_A for cell C (1.092 eV) is almost equal to $E_{g,min}$ (1.095 eV). Cell D shows an E_A (1.144 eV) close to the $E_{g,min}$ (1.113 eV) value as well. Conversely, carriers can be generated in the window layer, including *i*-layer and buffer layers, when exposed to blue light. Under short wavelength illuminations, an E_A larger than the expected buffer/absorber interface E_g is observed for cell D. On the other hand, cell C presents an E_A of similar value as the absorber E_g at the front interface. These can be observed in Figure 37c and d.
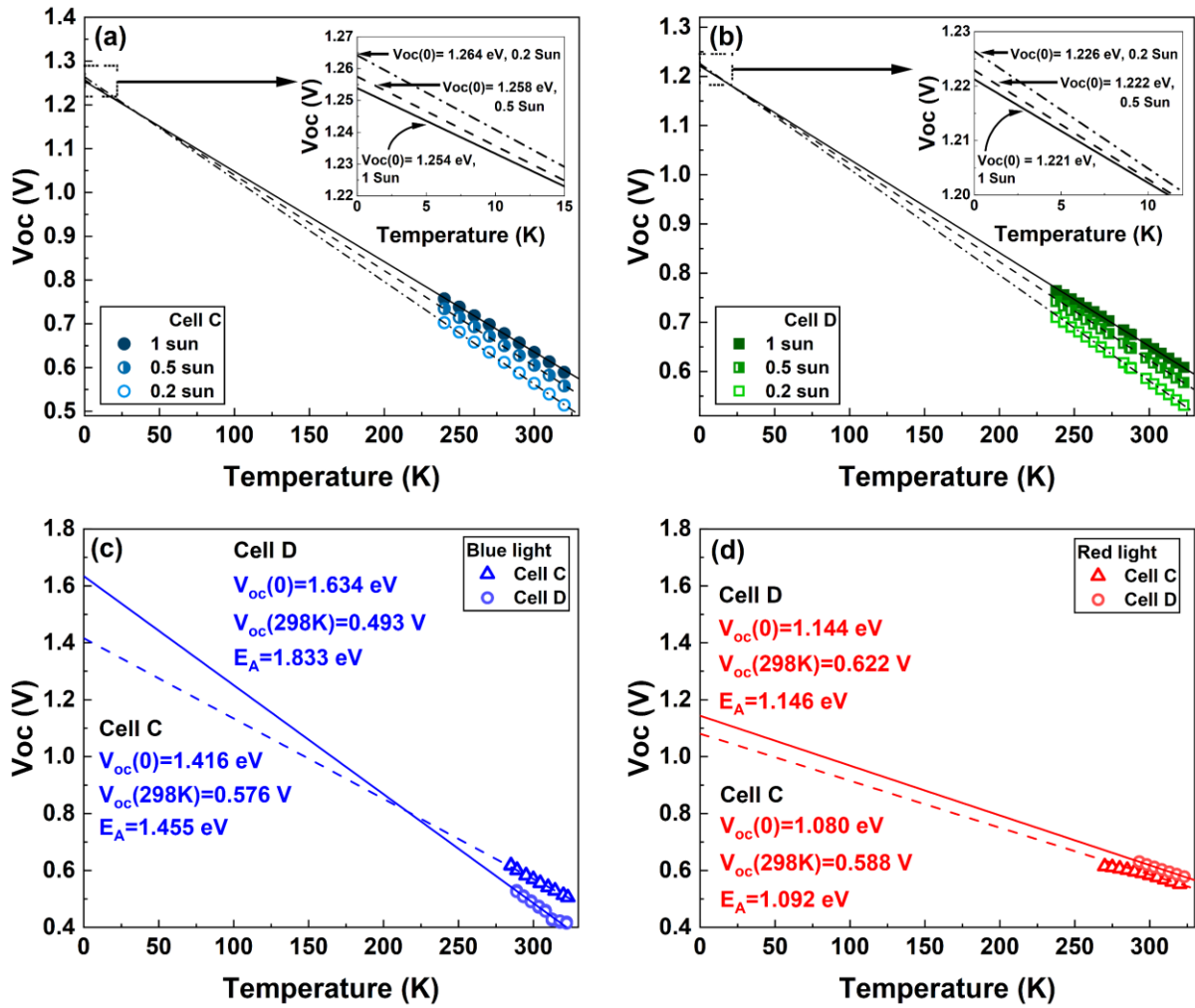
Figure 37: V$_{oc}$(T) plots taken with white light at different illuminations for (a) cell C, and (b) cell D. V$_{oc}$(T) plots taken under (c) blue and (d) red light illuminations for (c) cells C and D. V$_{oc}$ values extrapolated at 0 K, at 298 K, and E$_A$ values extracted from the one diode model are shown for each different light measurement.

It must be noted, that R_{sh} showed low values due to the non-lamination of our studied solar cells. Furthermore, all cells showed a negligible effect of R_{sh} on E_A values and therefore, on their recombination location. This was confirmed by modelling the E_A behavior of the studied solar cells by using the one diode model analysis (equation (7.2)) to account for the R_{sh} effect (see Figure 38). It is observed that, although the implementation of the i-layer led to an increase of R_{sh}, this is not the cause of the dominant recombination location shift discussed previously.
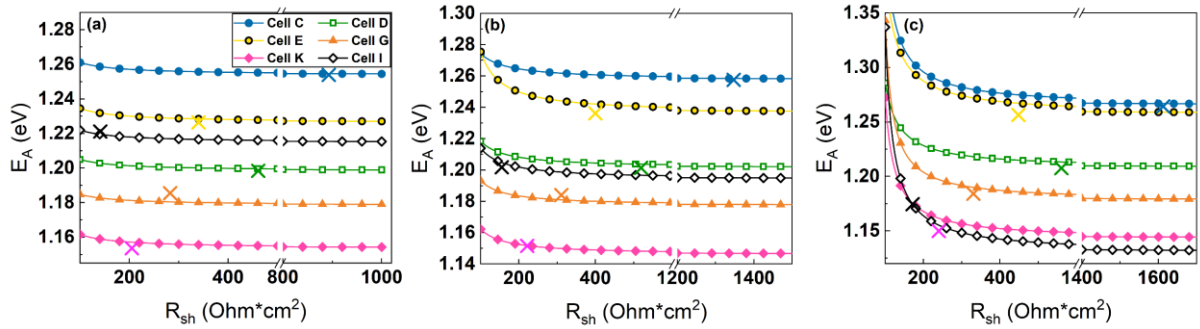
Figure 38: Effect of R_{sh} on E_A of all used solar cells at (a) 1 sun, (b) 0.5 sun, and (c) 0.2 sun light intensities. As illumination decreases, the effect of R_{sh} on E_A values becomes more evident. For our used cells, R_{sh} had a negligible effect on obtained E_A values. Cross symbols indicate the $V_{oc}(0)$ values, extracted from $V_{oc}(T)$ measurements.

To pinpoint the position of the absorbers where $E_{g,min}$ values are found, band gap profiles were extracted from GDOES elemental composition profiles by using the method proposed by Bär [80]. Briefly, it makes use of the GGI and SSSe values along the absorber depth to create an E_g profile obtained by

$$E_g(X, Y) = (1.00 + 0.13X^2 + 0.08X^2Y + 0.13XY + 0.55X + 0.54Y)eV \qquad (7.4)$$

Where X and Y represent the GGI and SSSe ratios, respectively. These band gap profiles are shown in Figure 39 for all studied cells. GDOES sputtering times were normalized to the corresponding absorber thickness. By using the W_{SCR} extracted for each cell from CV measurements (equation (4.14)), the location of the $E_{g,min}$ either in the SCR or bulk of the absorber can be inferred.
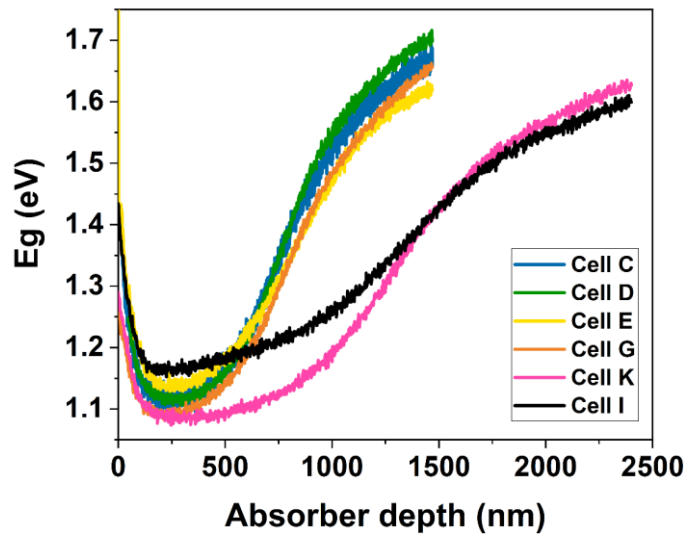
***Figure 39: Band gap profiles extracted from GDOES elemental composition profiles* and implementing Bär method** [80].*

Table 4, W_{SCR}, $E_{g,min}$ and $E_{g,min}$ locations for all studied solar cells

Cell	W_{SCR} (nm)	$E_{g,min}$ position (nm)	$E_{g,min}$ (eV)	$E_{g,IF}$ (eV)
C	266	230	1.095	1.412
D	265	250	1.113	1.362
E	226	230	1.134	1.459
G	283	230	1.092	1.256
K	327	315	1.085	1.281
I	257	230	1.164	1.413

The ideality factors were extracted by taking the derivative of a V_{oc} versus ln (J_{sc}-V_{oc}/R_{sh}) plot, at low light and high light intensities. They are shown in Table 5. It is observed that at high light, the ideality factor values decrease compared to low light values, except for cell K, whose ideality factor slightly increases. In general, the ideality factor values are in the range between 1 and 2, except for cell I, which show an ideality factor larger than 2 at low light conditions.

Table 5. Ideality factors extracted at low light (LL, ca. 0.3 suns) and high light (HL, ca. 1 sun) illuminations, extracted by using: $m = \frac{q}{kT}\frac{dVoc}{d\left(ln\left(Jsc-\frac{V_{oc}}{R_{sh}}\right)\right)}$.

Cell	Ideality factor (low light)	Ideality factor (high light)
C	1.68	1.56
D	1.68	1.42
E	1.92	1.67
G	1.62	1.52
K	1.65	1.70
I	2.23	1.50

Scheer described the meaning of E_A as the band gap through which carriers recombine[62]. Therefore, E_A values are expected in the range between $E_{g,min}$ and $E_{g,max}$ of the absorber of a

solar cell. Since the band gap of all studied CIGS absorbers are graded with a notch-like profile, it appears not so straightforward to assign the recombination region based simply on the strategy proposed by Scheer. A new parameter "*ER*" is proposed and defined as $ER = \frac{E_A}{E_{g,min}}$ to determine the dominant recombination region relative to $E_{g,min}$. Solar cell parameters' values were compared with their corresponding *ER* values at 0.2, 0.5 and 1 sun light intensities, in order to address the influence of the recombination's location shift on the solar cell parameters at different intensities. As can be seen in Figure 40a, only cell I showed an *ER* increment with increasing illuminations. V_{oc}, η, and *FF* were then compared with their corresponding *ER* values at different illuminations, showing for the case of *FF* a clear improvement with increasing *ER* values. Other cell parameters did not show any interesting trend with ER. Lastly, a comparison of the effect of R_{sh} on *FF* was also made, where the effect of R_{sh} on the *FF* resilience in low light conditions is further supported.
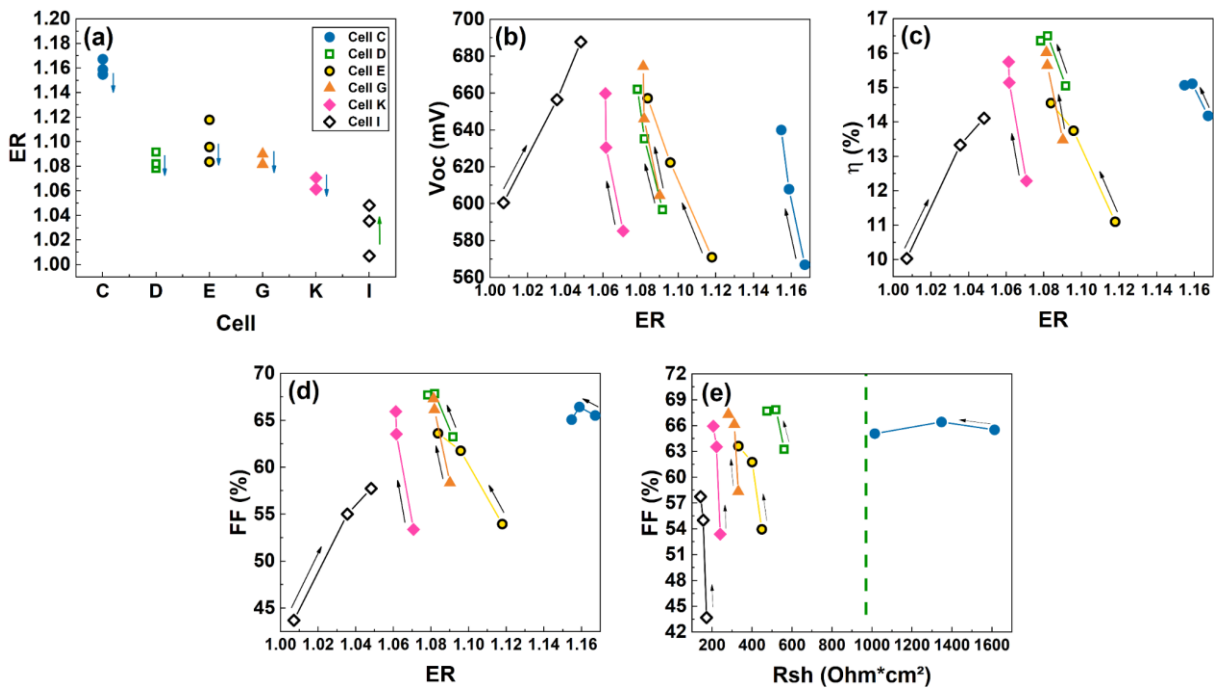
Figure 40: (a) ER values at 0.2, 0.5 and 1 sun illuminations for all studied solar cells. (b) V_{oc}, (c) η, and (d) FF at 0.2, 0.5 and 1 sun illuminations compared with their corresponding ER values. (e) Correlation between FF and R_{sh} for all studied cells. A green line marks the optimized minimum R_{sh} value found for the studied cells. Arrows indicate the direction of increasing illumination, from 0.2 to 1 sun.

Similar to the parameter's investigation, the $\beta_{X,rel}$ of V_{oc}, *FF* and η under different light intensities were extracted and compared with their *ER* values. In Figure 41a, it can be seen that $\beta_{Voc,rel}$ shows a similar trend as V_{oc} with illumination (Figure 40b).

$\beta_{FF,rel}$ shows an inflection point in trend with illumination for thinner and thicker cells (marked with a green line in Figure 41c). Furthermore, since the R_{sh} is an important parameter that

influence the FF, shunt resistance relative temperature coefficients ($\beta_{Rsh,rel}$) were obtained and compared with $\beta_{FF,rel}$. It can be seen that the temperature sensitivity of shunt resistance correlates strongly with $\beta_{FF,rel}$ (Figure 41d). As $\beta_{Rsh,rel}$ becomes smaller, $\beta_{FF,rel}$.is improved.
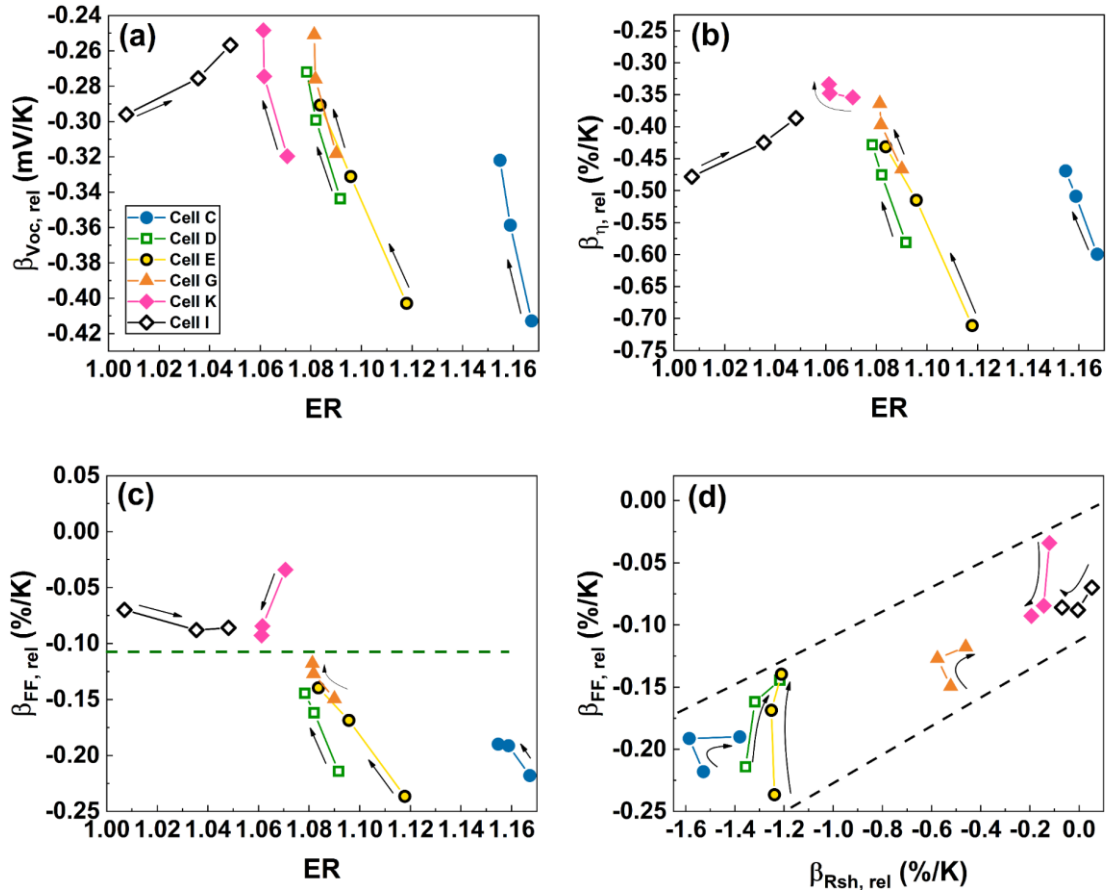
Figure 41: (a) $\beta_{Voc,rel}$, (b) $\beta_{\eta,rel}$, and (c) $\beta_{FF,rel}$ solar cell temperature coefficients at 0.2, 0.5 and 1 sun light intensities, compared with their corresponding ER values. (d) Correlation of $\beta_{FF,rel}$ with $\beta_{Rsh,rel}$ at 0.2, 0.5 and 1 sun illuminations. The direct trend between these two parameter temperature sensitivities is denoted with two dashed lines.

7.3 Discussion

7.3.1 i-layer and shunt resistance impact on the performance resilience

The strong non-resilient effect of Cell I with decreasing illuminations is attributed to an increased density of defects in the front side of the absorber, originating from the incorporating a larger Ga concentration in the absorber for cell I compared to cell K [155], [156]. These defects lead to a stronger recombination of photogenerated carriers. This is further supported by the increasing J_0 at low light (Figure S 3b), and the abnormally high ideality factor seen in Table 5. The stronger J_0 increment seen at lower illuminations explains the fact that recombination defects saturate at high illumination, making their effect more prone at low light

illumination. On the contrary, cell C shows the most resilient performance under different illuminations, as well as the highest R_{sh} value among all cells, which can be explained by the positive impact of *i*-layer implementation on the interface defect states with the buffer layer. Thus, the buffer/*i*-layer interface recombination is mitigated and consequently, holes generated in the buffer or *i*-layer diffuse and recombine in the buffer/absorber interface instead. In cell D, where the *i*-layer is not implemented, a larger density of defects is estimated in the window/buffer interface, which lead to higher recombination in this interface. To illustrate the impact of R_{sh} on the *FF* resilience at low light illuminations, Figure 40f shows *FF* values for all cells and compared with their corresponding R_{sh} values. It was confirmed that, regardless of the layer structure, aiming for a large R_{sh} value is fundamental when working in low light. For the studied cells, a R_{sh} value of ~1000 Ω cm^2 showed to be the minimum value required to maintain the *FF* stable at all illuminations studied.

From Figure 37d, under red light conditions, both cells C and D show E_A values close to their $E_{g,min}$ values, indicating a dominant recombination close to the bulk/SCR interface, since the $E_{g,min}$ was found to be located in the bulk edge with the SCR. For Cell D, the dominant recombination is further complemented with an increased E_A under blue light conditions. This recombination mechanism enhancement seems to increase the E_A value due to the larger band gap present in the buffer/window interface [157]. It is suggested that there is a mixture of recombination paths on the buffer/window interface and the absorber that causes E_A to have values larger than any band gap present in the absorber. On the other hand, Cell C presents a more discrete E_A increase under blue light conditions. This is attributed to the role of *i*-layer in cell C for reducing the recombination in that region [158]. This can further support the interpretation that cell C shows a better performance due to the recombination reduction in buffer/*i*-layer. When the *i*-layer is omitted, a larger density of interface defects is expected in the buffer/window layer interface, leading to an enhanced recombination at all light intensities in that region, and a consequent overall decrease of cell performance. This is further supported by comparing V_{oc} values for both cells under blue light conditions, where cell C shows a V_{oc} value at 298K of ~80 mV larger than in cell D, indicating less recombination losses when light is absorbed in front layers (Figure 37c). On the contrary, under red light conditions, both cells show a lower V_{oc} difference at 298K of ~30 mV (Figure 37d). This highlights the importance of accounting for the recombination occurring in the buffer/window interface to further improve the performance of solar cells under low light intensities.

For all modifications implemented in the studied solar cells, an improvement noticed in their low light performance is accompanied by a large shunt resistance, which emphasize the importance of this parameter for the low light behavior. Therefore, the optimization of this parameter must be carefully controlled during cell fabrication. This highlights the importance of accounting for the recombination occurring in the buffer/window interface in order to further improve the performance of solar cells under low light conditions.

7.3.2 Determining the dominant recombination location shift in graded band gap absorbers

Based on the model from Scheer *et al*. for dominant recombination location in solar cell, it is assumed that different recombination behaviors depend on the region where carriers are being generated. Recalling the definition of E_A as the band gap through which carriers recombine (see Table 6). It should be noted that this description is only considered for a non-graded absorber band gap. For a graded band gap, the E_A would change according to the corresponding band gap through which carriers recombine dominantly. Therefore, the GDOES profile was used to locate the region with $E_{g,min}$, as well as to indicate the direction of recombination shifts.

Table 6. E_A values corresponding for different recombination mechanisms in a solar cell with non-graded and graded absorber band gap.

Recombination region	Condition	E_A (non-graded absorber)	E_A (graded absorber)
SCR		$E_{g,a}$	$E_{g,SCR}$
Bulk		$E_{g,a}$	$E_{g,bulk}$
IF	No-FLP	$E_{g,IF}$	$E_{g,IF}$
	FLP	$\varphi_b{}^0$	$\varphi_b{}^0$

Since the S grading in the front side of absorbers is implemented, the E_g in the surface of the absorber is larger than $E_{g,min}$. Therefore, an E_A values larger than $E_{g,min}$, indicate dominant recombination closer to the buffer/absorber interface. *ER* values closer to one, rather suggests recombination within the SCR or bulk edge, as $E_{g,min}$ is located in this region. To determine the region towards which recombination shifts at different illumination, first the dominant

recombination location must be identified. Since the ideality factors are between 1 and 2 values for all cells at high illumination, it could be interpreted that the dominant recombination location is in SCR. Starting from there, an increase in *ER* value will indicate a shift towards the buffer /absorber interface, while recombination shift towards the bulk region would imply a lower *ER* value. Therefore, it is noteworthy that the $\beta_{X,rel}$ and the cell parameters' behavior at different illuminations can be described by the different recombination region dependencies for each. Parameters improve when the recombination shifts towards the interface rather than bulk, and the opposite trend is seen for the $\beta_{X,rel}$, which improve when the recombination region shifts towards the absorber bulk.

Grover's model describes the recombination contribution from interface, SCR and bulk regions [154]. Nevertheless, this approach is only valid at high light intensities, where *m* is close to 1. This does not apply for the studied case since lower light intensities are used. Nevertheless, it showed relatively similar observed trends between cells, which indicated similar shifts in recombination location. As a guide for the recombination location, an analysis relating interface-to-bulk recombination ratios were made [154], [157], showing comparable behaviors (see Supplementary information, Figure S 4).

7.3.3 Na-PDT influence on the dominant recombination

Figure 40 and Figure 41 show the effect of a PDT implementation when cells E and G are compared. Here, Improvements on V_{oc}, η, *FF*, and their corresponding temperature coefficients become evident. This effect could be attributed to the efficacy of Na in passivating the interface defects that reflects on a reduction of the recombination at grain boundaries [159].

In Figure 41 it is shown that cells G, K and I present better $\beta_{X,rel}$ than cells C, D and E. Furthermore, since it was observed that shifting the recombination towards the bulk improve the $\beta_{X,rel}$, the behavior of cells G, K and I is owed to the passivated absorber surface due to the implementation of a PDT step. Consequently, the relatively smaller *ER* values observed could be attributed to the reduction in buffer/absorber interface recombination, hence the shift towards the bulk region. It is worth mentioning that the dominant recombination region and the magnitude of the recombination are mutually independent. This could be the reason behind the similar *ER* values seen for cells E and G, while they present different $\beta_{X,rel}$, specially at low illuminations. Apart from the influence of the PDT on the low light trend, it is apparent that the absorber thickness's modification also contributes to the illumination trend seen on the $\beta_{FF,rel}$.

7.3.4 Absorber's thickness influence on the $\beta_{FF,rel}$

It is generally discernible, that shifting the recombination towards the bulk region leads to an improvement in $\beta_{FF,rel}$ values. Cells with thicker absorbers could exhibit a longer diffusion path in the bulk, therefore increasing the probability of bulk recombination in comparison to cells with thinner absorbers (Figure 42).

Since the low light $\beta_{FF,rel}$ for cells K and I are smaller than in high light, $FF(T)$ plots were analyzed under 1, 0.5 and 0.2 sun illuminations, in order to further investigate the recombination through defects under low light intensities. In Figure 42a and b, $FF(T)$ for cells G and K are shown, respectively. From these graphs it can be seen that, at the low temperature region, FF increases with increasing temperature, attributed to the effect of a thermionic emission barrier in the direction of carrier collection, most probably present in the buffer/absorber heterointerface. This barrier becomes more prominent and effective as temperature decrease, mainly due insufficient energy present in carriers to overcome said barrier. After electrons overcome the heterointerface barrier at higher temperatures, FF starts to decrease, and at sufficiently high temperatures, it decreases linearly with increasing temperature [42]. After overcoming the transport barrier, both cells show a different behavior under low light conditions. Cell G (with thinner absorber), under 0.2 sun illuminations shows a linear trend through the rest of the temperature interval, while cell K (with thicker absorber) shows two different regions, labeled I and II, where FF decreases at different rates. In region I, cell K shows a fast FF decrease, while in region II, this FF loss rate is decreased. Clearly, a beneficial effect stemming from high temperatures is present in the thicker absorber cell. This speculation is based on the role of electron traps along the absorber that directly affect the transport of minority carriers. Figure 42d and e show the transport mechanism for cells with thin and thick absorbers. In cells with thin absorbers (Figure 42d), light is absorbed (1) and photogenerated carriers then travel towards the buffer/absorber interface, which is reachable within the diffusion length of the carrier (2). In the case of cells with thicker absorbers (~50% thicker), the mean diffusion length could be not sufficient to reach this interface (Figure 42e), therefore increasing the probability of electron trapping (2). At low temperatures, electrons could recombine due to insufficient thermal energy to be re-emitted (3a), promoting the decrease of FF (region I in Figure 42b). On the other hand, when the temperature is high enough, trapped carriers can be re-emitted to the conduction band and diffuse further towards the buffer/absorber interface (3b), which would slow the overall FF decrease rate with increasing temperature (region II in Figure 42b) and consequently, improve $\beta_{FF,rel}$ as well. In Figure 42c, current

densities at maximum power point (J_{mpp}) values correlate with the described $FF(T)$ behavior at 0.2 sun illuminations and temperatures over 200 K, indicating that the enhanced carrier collection under P_{mpp} conditions is the cause of the resilient $FF(T)$ behavior of cell K. As illumination is increased, regions I and II of $FF(T)$ are no longer differentiable, indicating that the available defects become saturated due to an excess of photogenerated electrons, thereby minimizing their effect on the transport characteristics. This detrapping mechanism is not observed in a thin absorber solar cell since the mean diffusion path can already be enough to reach the front interface without the need of trapped carriers' re-emission (Figure 42d). For the case of Cell I, this also suggests the presence of a larger defect density in the bulk region of thicker absorbers, that could result from grain boundaries formed precisely due to thicker absorber implementation [160]. This is further supported by ideality factors larger than 2 found at low illuminations in cell I (Table 5).

It must be noted that this FF behavior on thick absorber cells could not be attributed to the effect of a thermionic barrier, where a thermionic emission current is described as

$$I = A_G T^2 e^{-\frac{\phi}{kT}} \qquad (7.5)$$

Where A_G is a material specific constant in the order of 10^6 with units A m^{-2} K^{-2}, T is the sample's temperature, k is the Boltzmann constant and Φ is the thermionic barrier height. Clearly, an effect of such a barrier would be affected only by the material temperature and the value of Φ.
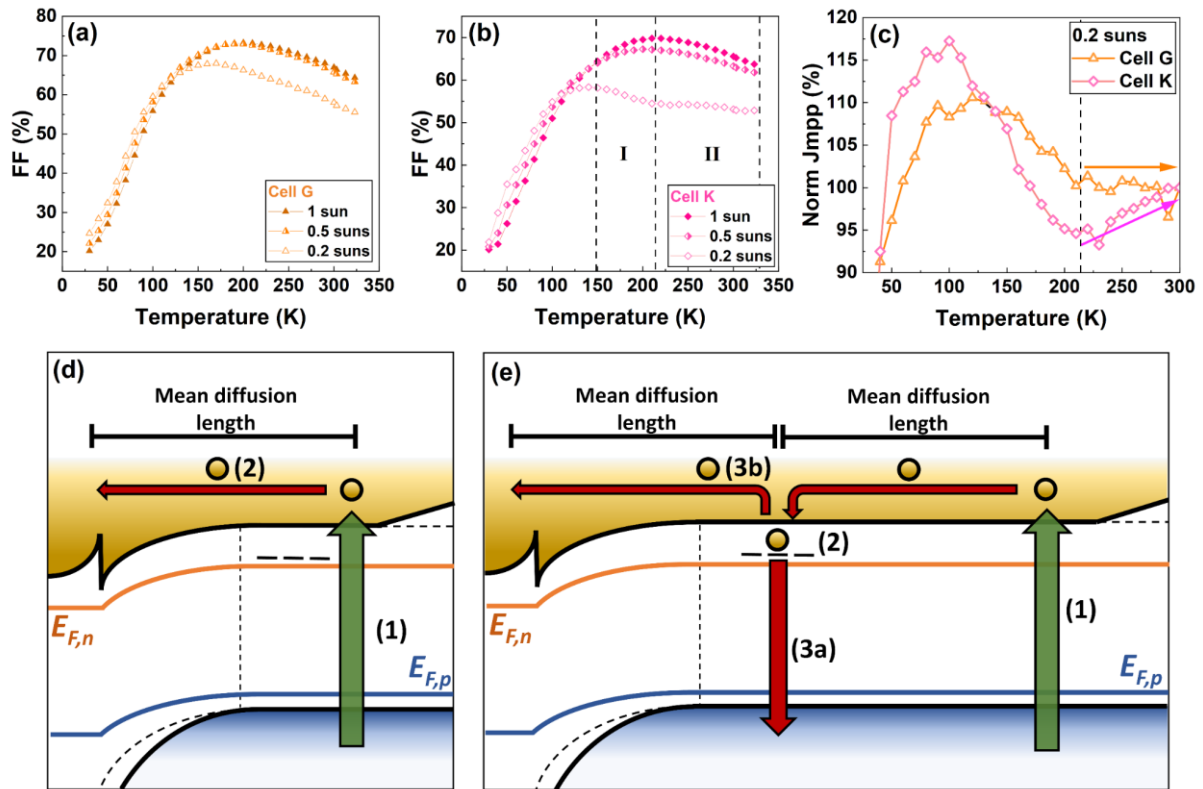
Figure 42: FF(T) plots taken at 0.2, 0.5 and 1 sun illuminations for (a) cell G, and (b) cell K. (c) J_{mpp}(T) values for both cells at 0.2 sun illuminations. (d) and (e) show the proposed mechanism affecting the FF(T) at low illuminations for thin and thick absorber solar cells, respectively.

These differences in diffusion paths between thinner and thicker absorbers can further serve in the explanation of an interesting inflection point in the intensity behavior of $\beta_{FF,rel}$, which is shown with a green dashed line in Figure 41c. Under low light, photogenerated carriers in thicker absorbers (cells K and I) tend to recombine in the bulk, due to the longer diffusion distance needed to reach the interface (Figure 43b). On the other hand, under same light conditions, thin absorber's carriers might recombine easily through the buffer/absorber interface, as the diffusion path is shorter compared to thicker cells (Figure 43a). At high light intensity, thin absorbers' carrier recombination tends to saturate the close-to-interface region and further promote recombination through bulk states (Figure 43c), confirming the obtained lower *ER* values that indicate a recombination shift towards the bulk region with higher illumination. On the other hand, for thick absorbers' cells under high light intensities, generated carriers can first saturate bulk recombination channels and further diffuse to the interface region due to a larger presence of photogenerated carriers, enhancing interface recombination (Figure 43d). As illumination is increased, cells with thicker absorbers showed an increase in *ER* values. It might turn questionable, if this increase is a result of an enhanced recombination towards the back of the absorber, where E_g is also larger than $E_{g,min}$. Nevertheless, it is not expected that

photogenerated carriers will diffuse to the back of the absorber because the implemented back grading is designed to yield a back-surface field, which precisely avoids recombination in the back interface.
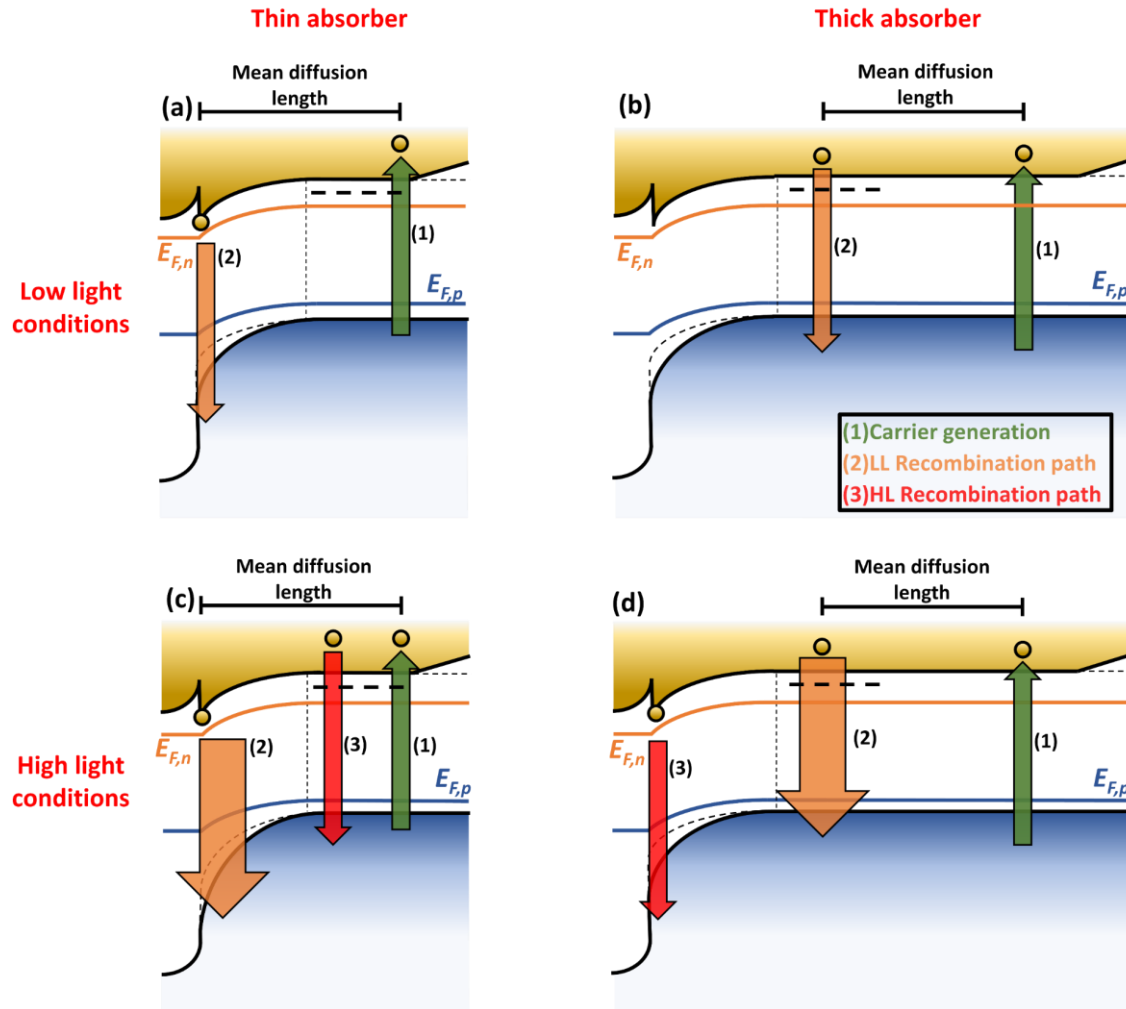
Figure 43. Proposed recombination locations for thin (a) and thick (b) absorber solar cells under low light conditions, respectively. The recombination mechanisms under high light conditions are represented for thin and thick absorber solar cells in (c) and (d), respectively. Orange arrows indicate the dominant recombination channel for all cases, while red arrows indicate the recombination mechanism that is promoted under high illumination conditions.

7.4 Conclusion

Temperature coefficients and parameters of different CIGS solar cell structures were investigated at temperatures between 250-300 K and at light intensities between ∼0.1 to 1 sun. The impact of different solar cell structures on the dominant recombination region at different light intensities were shown. A method to describe the dominant recombination location in CIGS solar cells with graded absorbers was proposed and implemented. It was found out, that decreasing recombination in buffer/window region leads to a considerable *FF* and *η* resilience

in low light conditions. A new parameter ER is defined as the normalized E_A to the $E_{g,min}$ to account for the relative dominant recombination region with respect to the absorber $E_{g,min}$ location. The change in light intensities' effect on the shift of dominant recombination location was also studied. It was observed that solar cells with increased Ga in the absorber (cell I) showed a dominant recombination shift towards the front of the absorber at higher illuminations, while the rest of solar cells showed an opposite trend. Finally, the i-layer showed to have an enhancing effect for the solar cell resilience under different light intensities, which gives insight on the significance of diminishing recombination on the near-window region at low light intensities.

Chapter 8 Final conclusions and outlook

In this work, the characteristics influencing the performance, such as solar cell parameters' temperature coefficients and low light behavior of CIGS solar cells were investigated by means of optoelectronic device characterization and one diode modelling. This study was made for CIGS solar cells with different layer's elemental compositions and designing parameters' variations. At the beginning of this project, it was not yet known if any of the layer change would yield a considerable impact on the temperature sensitivity of the studied solar cells and their low light performance. Additionally, the low light temperature sensitivity and performance was not investigated before in the frame of layer heterostructures and parameters' design. Furthermore, the positive or negative impact of these changes on CIGS solar cells performance has not been investigated previously.

It was concluded that the absorber layer had the major influence on the temperature sensitivity of the solar cell, while the other layers did not show a comparable impact. The sodium post deposition treatment, the absorber thickness' increment up to 2.3 µm and implementing GGI and SSSe values in the front side of the absorber of up to 0.05 and 0.7, respectively, had the most remarkable enhancement on $\beta_{Voc,rel}$, whereas increasing the GGI further and using pure Mo back contacts showed a rather detrimental effect. This was highly attributed to the microscopic physical parameter's temperature dependence such as recombination currents and electron lifetimes rather than to V_{oc},def. Nevertheless, the latter governs the $\beta_{Voc,rel}$ under the condition that the cells exhibit similar band gap grading profile. It was estimated that the total value of $\beta_{Pmpp,rel}$ proved to be dominated by a ~65% contribution of its value from the $\beta_{Voc,rel}$ followed by the ~30% attributed to the $\beta_{FF,rel}$, while the $\beta_{Jsc,rel}$ showed the smallest impact.

The solar cell parameters' temperature coefficients at low light appeared to be improved when the dominant recombination location shifts towards the bulk of the absorber rather than the interface, and the opposite is shown for the parameters of solar cells.

The i-layer implementation is particularly important for improving the low light performance of the solar cell, as it increases the shunt resistance considerably and shifts the recombination towards the absorber/buffer interface. This sheds light on the relevance of the i-layer/buffer interface to improve the resilience of the cell's performance at different light intensities.

Cells with thicker absorbers revealed surprisingly a better $\beta_{FF,rel}$ value at low light compared to high light intensities. This is ascribed to the role of the temperature on the effective diffusion

length of the photogenerated carriers, which can be re-emitted from traps in the absorber. This mechanism is more beneficial under low light conditions, as the ratio of re-emitted carriers to photogenerated carriers is larger. Furthermore, large ideality factors observed under low light conditions for the Ga-richest absorber cells suggested the presence of large defect densities, which could have served as recombination centers at low temperatures, while at higher temperatures behave as traps.

The metastability of $\beta_{FF,rel}$ on cell B was found to be resulting from the choices of the combined elemental layers together. On one hand, solar cells with an arrangement of Ga and S poor CIGS absorbers along with In_xS_y buffers showed a stable performance. On the other hand, an identical buffer combined with a similar absorber that is only different in slightly larger GGI and SSSe values showed a considerable metastable behavior in the temperature coefficients of the device. This highlighted the contribution of the elemental grading of the absorber to the metastability of the solar cell. It was observed that the larger GGI present in the absorber, the rougher the absorber surface becomes. This roughness enhanced the elemental interdiffusion between absorber and buffer layer. This implied the importance of finding a compromise between achieving high parameters' values and causing elemental interdiffusion that could translate to a metastable performance, due to increased Ga in the absorber. The amphoteric defect causing the metastable behavior observed was determined by the analysis of low temperature CV and IV(T, λ). TEM/EDX analysis showed diffusion of Cu into the In_xS_y buffer. This led to the creation of mid-gap acceptor levels in the buffer that are known to induce a photoconductive behavior, seen by EQE(λ). This effect changes the conductivity of the buffer upon blue light illumination and yielded an enhanced carrier collection due to the doping density recovery.

Two counteracting defects, DX states and V_{Se}-V_{Cu} complexes found in the absorber of the metastable structure cell are light and temperature sensitive. These characteristics led to longer light soaking times needed to stabilize the cell properly to overcome the detrimental effects of their amphoteric behavior on the $\beta_{FF,rel}$. It is worth noting that this long time of light soaking needed is only to stabilize the temperature coefficient. For the solar cell parameters, only few hours of white light soaking at constant temperature were enough to stabilize them. In order to prevent the metastability effect on the temperature coefficients, buffer materials with high atomic interdiffusion resilience should be selected such as Zn(O,S), as it showed to minimize the detrimental impact of defects caused from diffused elements from high Ga absorbers.

Future possibilities for improvement could be considering the layers' elemental composition structures as fundamental for enhancing the temperature coefficient, their stability, and the low light performance. It is estimated that if the absorber layer modifications of cells G to I were implemented on Mo-Cu back contact solar cells (cell D), the temperature coefficients would show a considerable enhancement. Additionally, if the applied variations of the absorber were implemented without removing the *i*-layer (on cell C), a resilient performance under different light intensities could have been achieved for all cells. The non-laminated cells investigated in this thesis were of great help to study the intrinsic properties of the cells. Nevertheless, laminated (encapsulated) cells of the same type variations would have been necessary to improve the external shunt resistance effect.

The final influence of the temperature coefficients, the low light, along with the effect of spectral sensitivity on solar cell performance should be estimated at different geographical locations for further decision-making regarding the layer configurations, which could have made the analysis much more complicated. Therefore, this work's aim was first to study the influence of each effect independently as a preliminary step. Nevertheless, it is highly suggested to integrate their influences together to predict the real behavior of the solar cell modules in the future.

In closing, it can be briefly concluded that varying the layer structures was an ideal following strategy for investigating their influence on solar cells temperature coefficients. Particularly, the absorber layer variations were appropriate to achieve a significant enhancement of the temperature coefficients, competing with $\beta_{Pmpp,rel}$ of crystalline Si solar cells, and surpassing them in $\beta_{Voc,rel}$. It also must be noted that, when aiming to improve the temperature coefficient of the output power of CIGS modules, temperature coefficient of open circuit voltage enhancement is a key for the development. Furthermore, studies of dominant recombination location shed light on their impact on temperature coefficients and solar cell parameters. Finally, caring for appropriate buffer/absorber pairs in CIGS solar cells is fundamental to reduce metastable defects, which could affect the temperature coefficients.

Supplementary Information

Table S. 1. Obtained parameters for cell E after four IV(T) hysteresis measurements, showing the accuracy of the used IV(T) device.

Parameter	Value	Std. Error
V_{oc}	658.632 mV	0.567 mV
FF	64.202 %	0.097 %
η	14.390 %	0.037 %
$\beta_{Voc,abs}$	-2.266 mV/K	0.016 mV/K
$\beta_{FF,abs}$	-0.115 %/K	0.002 %/K
$\beta_{\eta,abs}$	-0.076 %/K	0.001 %/K
$\beta_{Voc,rel}$	-0.344 %/K	0.002 %/K
$\beta_{FF,rel}$	-0.179 %/K	0.003 %/K
$\beta_{\eta,rel}$	-0.528 %/K	0.009 %/K
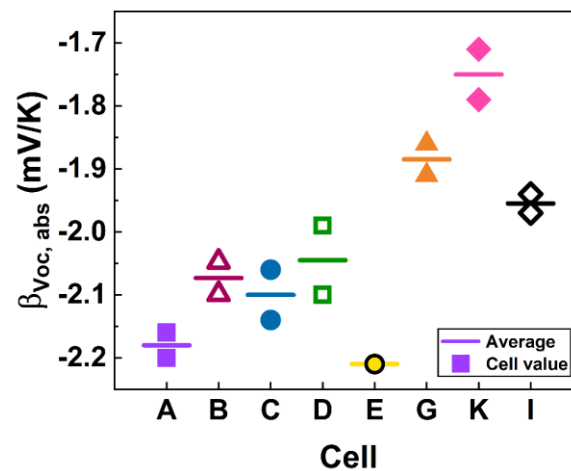
Figure S 1: $\beta_{Voc,abs}$ for all studied solar cells.
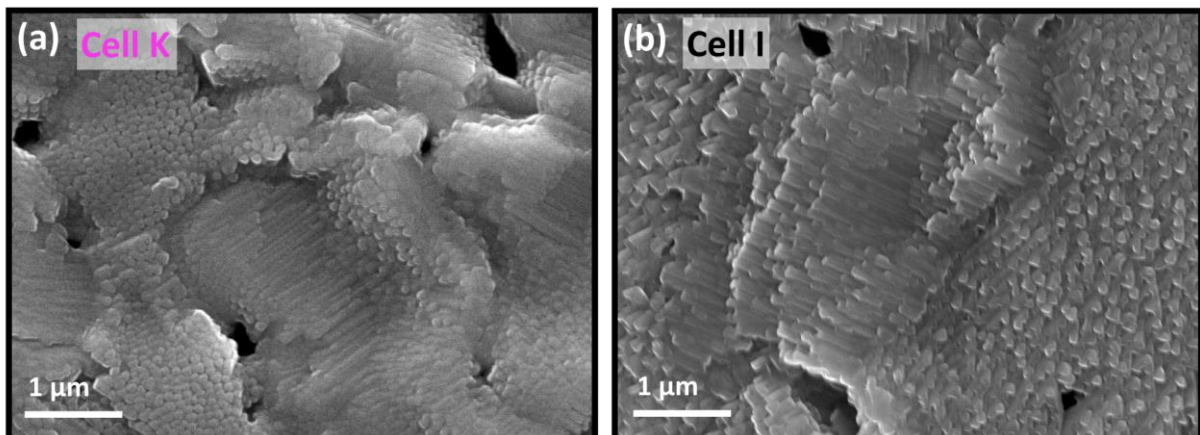
Figure S 2: SEM micrographs* of bare absorbers of cells (a) K and (b) I.
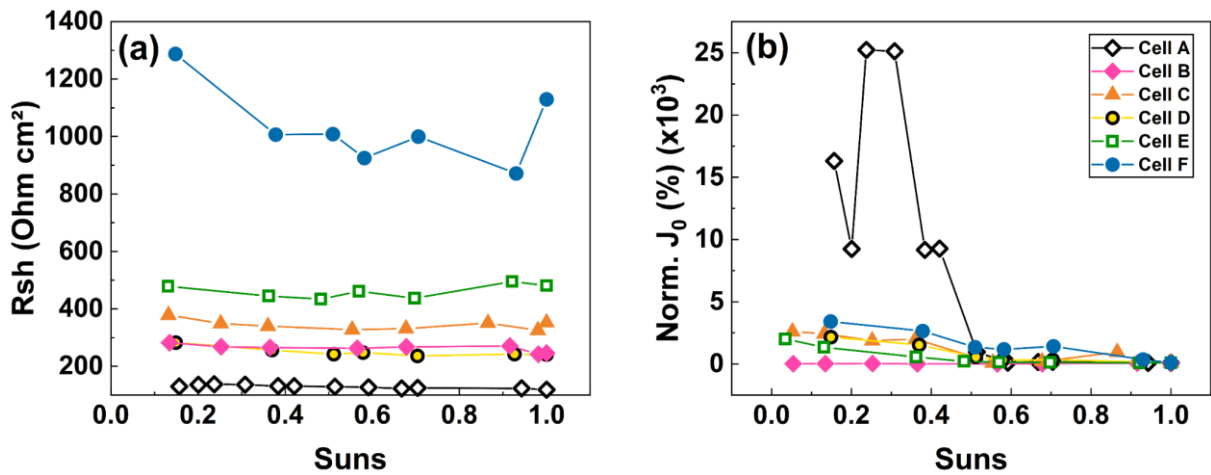
Figure S 3: (a) R_{sh} values and (b) Normalized J_0 values at different illuminations for all studied solar cells.
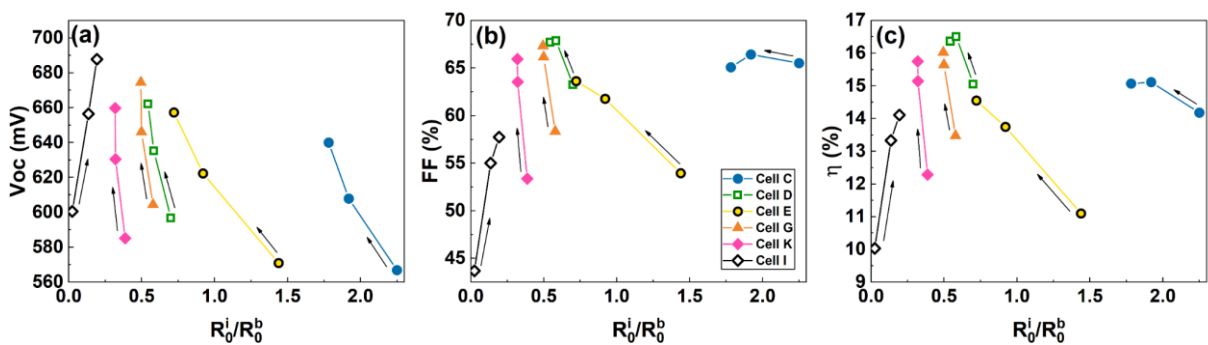
Figure S 4: Correlation of solar cell parameters with their interface-to-bulk recombination rates, according to the model described by Grover and Riley [154], [157] . *Here, R_0^i represents the interface recombination rate, while R_0^b indicates the bulk recombination rate.*

Bibliography

[1] I. - International Energy Agency, "World Energy Outlook EXECUTIVE SUMMARY," 2018.

[2] A. Jäger-Waldau, "Snapshot of photovoltaics-February 2020," *Energies*, vol. 13, no. 4, 2020.

[3] M. S. Michael Schmela, Aurélie Beauvais, Naomi Chevillard, Mariano Guillén Paredes, Máté Heisz, Raffaele Rossi, "Mobilising Investments in Emerging Markets," *Glob. Mark. Outlook*, p. 92, 2019.

[4] M. K. H. Rabaia *et al.*, "Environmental impacts of solar energy systems: A review," *Sci. Total Environ.*, vol. 754, p. 141989, 2021.

[5] D. M. Chapin, C. S. Fuller, and G. L. Pearson, "A new silicon p-n junction photocell for converting solar radiation into electrical power," *J. Appl. Phys.*, vol. 25, no. 5, pp. 676–677, 1954.

[6] T. D. Lee and A. U. Ebong, "A review of thin film solar cell technologies and challenges," *Renew. Sustain. Energy Rev.*, vol. 70, no. September 2015, pp. 1286–1297, 2017.

[7] P. Würfel and U. Würfel, *Physics of Solar Cells: From Basic Principles to Advanced Concepts*, 3rd ed. Wiley VCH, 2016.

[8] M. Green, E. Dunlop, J. Hohl-Ebinger, M. Yoshita, N. Kopidakis, and X. Hao, "Solar cell efficiency tables (version 57)," *Prog. Photovoltaics Res. Appl.*, no. November, pp. 1–13, 2020.

[9] S. Sharma, K. K. Jain, and A. Sharma, "Solar Cells: In Research and Applications—A Review," *Mater. Sci. Appl.*, vol. 06, no. 12, pp. 1145–1155, 2015.

[10] M. A. Green, "Third generation photovoltaics: Solar cells for 2020 and beyond," *Phys. E Low-Dimensional Syst. Nanostructures*, vol. 14, no. 1–2, pp. 65–70, 2002.

[11] J. Yan and B. R. Saunders, "Third-generation solar cells: A review and comparison of polymer:fullerene, hybrid polymer and perovskite solar cells," *RSC Adv.*, vol. 4, no. 82, pp. 43286–43314, 2014.

Bibliography

[12] H. Hahn, "Über einige ternäre Chalkogenide mit Chalkopyritstruktur," *Zeitschrift für Anorg. und Allg. Chemie*, vol. 271, 1953.

[13] L. L. Kazmerski, F. R. White, M. S. Ayyagari, Y. J. Juang, and R. P. Patterson, "Growth and Characterization of Thin-Film Compound Semiconductor Photovoltaic Heterojunctions.," *J Vac Sci Technol*, vol. 14, no. 1, pp. 65–68, 1976.

[14] U. P. Singh and S. P. Patra, "Progress in polycrystalline thin-film Cu(In,Ga) Se2 solar cells," *Int. J. Photoenergy*, vol. 2010, 2010.

[15] A. M. Gabor, J. R. Tuttle, D. S. Albin, M. A. Contreras, R. Noufi, and A. M. Hermann, "High-efficiency CuInxGa1-xSe2 solar cells made from (Inx,Ga1-x)2Se3 precursor films," *Appl. Phys. Lett.*, vol. 65, no. 2, pp. 198–200, 1994.

[16] A. Chirilă *et al.*, "Potassium-induced surface modification of Cu(In,Ga)Se2 thin films for high-efficiency solar cells," *Nat. Mater.*, vol. 12, no. 12, pp. 1107–1111, 2013.

[17] P. et al. Jackson, "New world record efficiency for Cu(In,Ga)Se2 thin-film solar beyond 20%," *Prog. Photovoltaics Res. Appl.*, vol. 19, pp. 894–897, 2011.

[18] M. Nakamura, K. Yamaguchi, Y. Kimoto, Y. Yasaki, T. Kato, and H. Sugimoto, "Cd-Free Cu (In , Ga)(Se , S) 2 Thin-Film Solar Cell With Record Efficiency of 23 . 35 %," *IEEE J. Photovoltaics*, vol. 9, no. 6, pp. 1863–1867, 2019.

[19] L. L. Kazmerski, M. Hallerdt, P. J. Ireland, R. A. Mickelsen, and W. S. Chen, "Optical properties and grain boundary effects in CuInSe2," *J. Vac. Sci. Technol. A Vacuum, Surfaces, Film.*, vol. 1, no. 2, pp. 395–398, 1983.

[20] A. C. Badgujar, K. Madhuri, S. Garner, S. R. Dhage, and S. V. Joshi, "Non-vacuum route for CIGS thin film absorber on flexible glass substrates," *2015 IEEE 42nd Photovolt. Spec. Conf. PVSC 2015*, vol. 2, pp. 2–5, 2015.

[21] J. Ramanujam and U. P. Singh, "Copper indium gallium selenide based solar cells – a review," *Energy Environ. Sci.*, vol. 10, no. 6, pp. 1306–1319, Jun. 2017.

[22] A. Klein, "Energy band alignment in chalcogenide thin film solar cells from photoelectron spectroscopy," *J. Phys. Condens. Matter*, vol. 27, no. 13, p. 134201, Apr. 2015.

[23] J. Chantana, T. Kato, H. Sugimoto, and T. Minemoto, "Structures of Cu(In,Ga)(S,Se)2

solar cells for minimizing open-circuit voltage deficit: Investigation of carrier recombination rates," *Prog. Photovoltaics Res. Appl.*, vol. 27, no. 7, pp. 630–639, 2019.

[24]   D. Hariskos *et al.*, "The Zn(S,O,OH)/ZnMgO buffer in thin-film Cu(In,Ga)(Se,S)2 - based solar cells part II: Magnetron sputtering of the ZnMgO buffer layer for in-line co-evaporated Cu(In,Ga)Se2 solar cells," *Prog. Photovoltaics Res. Appl.*, vol. 17, no. 7, pp. 479–488, Nov. 2009.

[25]   J. Song, T. J. Anderson, and S. S. Li, "Material parameter sensitivity study on CIGS solar cell performance," *Conf. Rec. IEEE Photovolt. Spec. Conf.*, pp. 15–18, 2008.

[26]   K. Takuya, "Cu (In, Ga)(Se, S)2 solar cell research in Solar Frontier : Progress and current status temperatures," *Jpn. J. Appl. Phys.*, vol. 56, no. 04CA02, p. 1, 2017.

[27]   S. A. Jensen *et al.*, "Beneficial effect of post-deposition treatment in high-efficiency Cu(In,Ga)Se2 solar cells through reduced potential fluctuations," *J. Appl. Phys.*, vol. 120, no. 6, 2016.

[28]   J. Adeeb, A. Farhan, and A. Al-Salaymeh, "Temperature Effect on Performance of Different Solar Cell Technologies," *J. Ecol. Eng.*, vol. 20, no. 5, pp. 249–254, 2019.

[29]   E. L. Meyer and O. K. Overen, "Blue skies and red sunsets: Reliability of performance parameters of various p-n junction photovoltaic module technologies," *Cogent Eng.*, vol. 6, pp. 1–20, 2019.

[30]   A. Al-Khazzar, "Behavior of Four Solar PV Modules with Temperature Variation," *Int. J. Renew. Energy Res.*, vol. 6, no. 3, pp. 1091–1099, 2016.

[31]   C. Coskun, U. Toygar, O. Sarpdag, and Z. Oktay, "Sensitivity analysis of implicit correlations for photovoltaic module temperature: A review," *J. Clean. Prod.*, vol. 164, pp. 1474–1485, 2017.

[32]   G. Nofuentes, J. De La Casa, M. Torres-Ramírez, and M. Alonso-Abella, "Solar spectral and module temperature influence on the outdoor performance of thin film PV modules deployed on a sunny inland site," *Int. J. Photoenergy*, vol. 2013, 2013.

[33]   S. P. Pless, M. Deru, P. Torcellini, and S. Hayter, "Procedure for Measuring and Reporting the Performance of Photovoltaic Systems in Buildings,National Renewable

Energy Laboratory (NREL)," 2005.

[34]   O. Dupré, R. Vaillon, and M. A. Green, *Thermal Behavior of Photovoltaic Devices*. 2017.

[35]   O. Dupre, R. Vaillon, and M. A. Green, "Experimental assessment of temperature coefficient theories for silicon solar cells," *2015 IEEE 42nd Photovolt. Spec. Conf. PVSC 2015*, vol. 6, no. 1, pp. 56–60, 2015.

[36]   P. Singh and N. M. Ravindra, "Temperature dependence of solar cell performance - An analysis," *Sol. Energy Mater. Sol. Cells*, vol. 101, pp. 36–45, 2012.

[37]   A. Virtuani, D. Pavanello, and G. Friesen, "Overview of Temperature Coefficients of Different Thin film Photovoltaic Technologies," 2010, no. September, pp. 6–10.

[38]   O. Dupré, R. Vaillon, and M. A. Green, "Physics of the temperature coefficients of solar cells," *Sol. Energy Mater. Sol. Cells*, vol. 140, pp. 92–100, 2015.

[39]   Y. Jiang, A. M. Soufiani, A. Gentle, F. Huang, A. Ho-Baillie, and M. A. Green, "Temperature dependent optical properties of CH3NH3PbI3 perovskite by spectroscopic ellipsometry," *Appl. Phys. Lett.*, vol. 108, no. 6, 2016.

[40]   J. C. C. Fan, "THEORETICAL TEMPERATURE DEPENDENCE OF SOLAR CELL PARAMETERS," *Sol. Cells*, vol. 17, pp. 309–315, 1986.

[41]   P. Löper *et al.*, "Analysis of the temperature dependence of the open-circuit voltage," *Energy Procedia*, vol. 27, pp. 135–142, Jan. 2012.

[42]   C. Schubbert *et al.*, "A simulation study on the impact of band gap profile variations and secondary barriers on the temperature behavior, performance ratio, and energy yield of Cu(In,Ga)(Se,S)2 solar cells," *Phys. Status Solidi Appl. Mater. Sci.*, vol. 212, no. 2, pp. 336–347, 2015.

[43]   N. Kata, D. Diouf, A. Darga, and A. Seidou Maiga, "The effect of the recombination mechanisms location on the temperature sensitivity of thin-film photovoltaic cells," *EPJ Photovoltaics*, vol. 10, no. January, pp. 6–11, 2019.

[44]   S. Grover and J. V. Li, "Theory and analysis of temperature coefficient of open-circuit voltage (dVOC/dT) in heterojunction solar cells," in *2015 IEEE 42nd Photovoltaic Specialist Conference, PVSC 2015*, 2015.

Bibliography

[45] G. Chicco, V. Cocina, P. Di Leo, F. Spertino, and A. Massi Pavan, "Error assessment of solar irradiance forecasts and AC power from energy conversion model in grid-Connected photovoltaic systems," *Energies*, vol. 9, no. 1, 2016.

[46] P. K. Dash and N. C. Gupta, "Variation of Temperature Coefficient of Different Technology Photovoltaic Modules with respect to Irradiance," *Int. J. Curr. Eng. Technol.*, vol. 55, no. 11, pp. 2277–4106, 2015.

[47] G. Makrides, B. Zinsser, G. E. Georghiou, M. Schubert, and J. H. Werner, "Temperature behaviour of different photovoltaic systems installed in Cyprus and Germany," *Sol. Energy Mater. Sol. Cells*, vol. 93, no. 6–7, pp. 1095–1099, 2009.

[48] A. H. Fanney, M. W. Davis, B. P. Dougherty, D. L. King, W. E. Boyson, and J. A. Kratochvil, "Comparison of photovoltaic module performance measurements," *J. Sol. Energy Eng. Trans. ASME*, vol. 128, no. 2, pp. 152–159, 2006.

[49] I. Repins *et al.*, "Large metastability in Cu (In,Ga)Se2 devices: The importance of buffer properties," *Prog. Photovoltaics Res. Appl.*, vol. 27, no. 9, pp. 749–759, 2019.

[50] M. Gostein and L. Dunn, "Light soaking effects on photovoltaic modules: Overview and literature review," *Conf. Rec. IEEE Photovolt. Spec. Conf.*, pp. 003126–003131, 2011.

[51] M. Igalson, M. Cwil, and M. Edoff, "Metastabilities in the electrical characteristics of CIGS devices: Experimental results vs theoretical predictions," *Thin Solid Films*, vol. 515, no. 15 SPEC. ISS., pp. 6142–6146, 2007.

[52] S. Lany and A. Zunger, "Light- and bias-induced metastabilities in Cu(In,Ga)Se2 based solar cells caused by the (VSe-VCu) vacancy complex," *J. Appl. Phys.*, vol. 100, no. 11, 2006.

[53] M. Pawłowski, P. Zabierowski, R. Bacewicz, N. Barreau, and A. Hultqvist, "Fill factor metastabilities in CIGSe-based solar cells investigated by means of photoluminescence techniques," *Conf. Rec. IEEE Photovolt. Spec. Conf.*, pp. 002787–002791, 2011.

[54] M. Igalson, A. Urbaniak, K. Macielak, M. Tomassini, N. Barreau, and S. Spiering, "Barriers for current transport in CIGS structures," *Conf. Rec. IEEE Photovolt. Spec. Conf.*, pp. 002727–002731, 2011.

Bibliography

[55]   S. Dongaonkar, E. Sheets, R. Agrawal, and M. A. Alam, "Reverse stress metastability of shunt current in CIGS solar cells," *Conf. Rec. IEEE Photovolt. Spec. Conf.*, pp. 868–872, 2012.

[56]   S. Lany and A. Zunger, "Intrinsic DX centers in ternary chalcopyrite semiconductors," *Phys. Rev. Lett.*, vol. 100, no. 1, pp. 1–4, 2008.

[57]   S. Lany and A. Zunger, "Anion vacancies as a source of persistent photoconductivity in II-VI and chalcopyrite semiconductors," *Phys. Rev. B - Condens. Matter Mater. Phys.*, vol. 72, no. 3, pp. 1–13, 2005.

[58]   J. T. Heath, J. D. Cohen, and W. N. Shafarman, "Distinguishing metastable changes in bulk CIGS defect densities from interface effects," *Thin Solid Films*, vol. 431–432, no. 03, pp. 426–430, 2003.

[59]   M. Chegaar, A. Hamzaoui, A. Namoda, P. Petit, M. Aillerie, and A. Herguth, "Effect of illumination intensity on solar cells parameters," *Energy Procedia*, vol. 36, pp. 722–729, 2013.

[60]   R. Gottschalg, T. R. Betts, A. Eeles, S. R. Williams, and J. Zhu, "Influences on the energy delivery of thin film photovoltaic modules," *Sol. Energy Mater. Sol. Cells*, vol. 119, pp. 169–180, 2013.

[61]   J. Chantana, T. Kato, H. Sugimoto, and T. Minemoto, "Investigation of correlation between open-circuit voltage deficit and carrier recombination rates in Cu(In,Ga)(S,Se)2-based thin-film solar cells," *Appl. Phys. Lett.*, vol. 112, no. 15, 2018.

[62]   R. Scheer and H. Schock, *Chalcogenide Photovoltaics Physics of Solar Cells Physics, Technologies, and Thin Film Devices*. Wiley, 2011.

[63]   K. Rühle, M. K. Juhl, M. D. Abbott, and M. Kasemann, "Evaluating Crystalline Silicon Solar Cells at Low Light Intensities Using Intensity-Dependent Analysis of I-V Parameters," *IEEE J. Photovoltaics*, vol. 5, no. 3, pp. 926–931, 2015.

[64]   S. Binetti *et al.*, "Fabricating Cu(In,Ga)Se2 solar cells on flexible substrates by a new roll-to-roll deposition system suitable for industrial applications," *Semicond. Sci. Technol.*, vol. 30, no. 10, 2015.

[65]   A. Hultqvist *et al.*, "Performance of Cu(In,Ga)Se2 solar cells using nominally alkali

free glass substrates with varying coefficient of thermal expansion," *J. Appl. Phys.*, vol. 114, no. 9, 2013.

[66]   S. H. Wei, S. B. Zhang, and A. Zunger, "Effects of Na on the electrical and structural properties of CuInSe2," *J. Appl. Phys.*, vol. 85, no. 10, pp. 7214–7218, 1999.

[67]   J. Hedström, H. Ohlsen, M. Bodegard, A. Kylner, and L. Stolt, "ZnO/CdS/Cu(In,Ga)Se2 thin film solar cells with improved performance," in *Conference Record of the Twenty Third IEEE Photovoltaic Specialists Conference*, 1993, pp. 364–371.

[68]   S. A. Pethe, V. Hadagali, and N. G. Dhere, "Development of silicon nitride barrier layer for CIGS thin film solar cells," *Thin Film Sol. Technol.*, vol. 7409, p. 740911, 2009.

[69]   M. Powalla *et al.*, "CIGS cells and modules with high efficiency on glass and flexible substrates," *IEEE J. Photovoltaics*, vol. 4, no. 1, pp. 440–446, 2014.

[70]   K. J. Hsiao, J. Da Liu, H. H. Hsieh, and T. S. Jiang, "Electrical impact of MoSe2 on CIGS thin-film solar cells," *Phys. Chem. Chem. Phys.*, vol. 15, no. 41, pp. 18174–18178, 2013.

[71]   X. Zhu, Z. Zhou, Y. Wang, L. Zhang, A. Li, and F. Huang, "Determining factor of MoSe 2 formation in Cu(In,Ga)Se 2 solar Cells," *Sol. Energy Mater. Sol. Cells*, vol. 101, pp. 57–61, 2012.

[72]   T. Wada, N. Kohara, S. Nishiwaki, and T. Negami, "Characterization of the Cu(In,Ga)Se2/Mo interface in CIGS solar cells," *Thin Solid Films*, vol. 387, no. 1–2, pp. 118–122, 2001.

[73]   K. H. Ong *et al.*, "Review on substrate and molybdenum back contact in CIGS thin film solar cell," *Int. J. Photoenergy*, vol. 2018, 2018.

[74]   J. Palm *et al.*, "Cd-Free CIS Thin Film Solar Modules at 17 % Efficiency," *29th Eur. Photovolt. Sol. Energy Conf. Exhib.*, pp. 1433–1438, Nov. 2014.

[75]   W. N. Shafarman, S. Siebentritt, and L. Stolt, *Cu (InGa) Se 2 Solar Cells*, vol. 346, no. 2010. 2003.

[76]   D. Abou-Ras, T. Kirchartz, and U. Rau, *Advanced Characterization Techniques for*

Thin Film Solar Cells: Second Edition, vol. 1–2. 2016.

[77]   T. Lepetit *et al.*, "Impact of DC-power during Mo back contact sputtering on the alkali distribution in Cu(In,Ga)Se2-based thin film solar cells," *Thin Solid Films*, vol. 582, pp. 304–307, 2015.

[78]   C. Spindler, "OPTICAL DETECTION OF DEEP DEFECTS IN CU(IN,GA)SE2," 2018.

[79]   W. Shockley and H. J. Queisser, "Detailed balance limit of efficiency of p-n junction solar cells," *J. Appl. Phys.*, vol. 32, no. 3, pp. 510–519, 1961.

[80]   M. Bär *et al.*, "Determination of the band gap depth profile of the penternary Cu(In (1-x)Gax)(SySe(1-y))2 chalcopyrite from its composition gradient," *J. Appl. Phys.*, vol. 96, no. 7, pp. 3857–3860, 2004.

[81]   N. E. I. Boukortt, S. Patanè, and Y. M. Abdulraheem, "Numerical investigation of CIGS thin-film solar cells," *Sol. Energy*, vol. 204, no. May, pp. 440–447, 2020.

[82]   O. Lundberg, M. Bodegård, J. Malmström, and L. Stolt, "Influence of the Cu(In,Ga)Se2 thickness and Ga grading on solar cell performance," *Prog. Photovoltaics Res. Appl.*, vol. 11, no. 2, pp. 77–88, 2003.

[83]   Z. Jehl *et al.*, "Thinning of CIGS solar cells: Part II: Cell characterizations," *Thin Solid Films*, vol. 519, no. 21, pp. 7212–7215, 2011.

[84]   P. Jackson, R. Wuerz, D. Hariskos, E. Lotter, W. Witte, and M. Powalla, "Effects of heavy alkali elements in Cu(In,Ga)Se2 solar cells with efficiencies up to 22.6%," *Phys. Status Solidi - Rapid Res. Lett.*, vol. 10, no. 8, pp. 583–586, 2016.

[85]   N. E. I. Boukortt, "Numerical optimization of 0.5-μm-thick Cu (In1-xGax) Se2 solar cell," *Optik (Stuttg).*, vol. 200, no. June 2019, 2020.

[86]   A. Khadir, "Simulation of effects of defects and layers thickness on the performance of CIGS solar cells," *Acta Phys. Pol. A*, vol. 137, no. 6, pp. 1128–1134, 2020.

[87]   J.-C. Park, J.-R. Lee, M. Al-Jassim, and T.-W. Kim, "Bandgap engineering of Cu(In_1-xGa_x)Se_2 absorber layers fabricated using CuInSe_2 and CuGaSe_2 targets for one-step sputtering process," *Opt. Mater. Express*, vol. 6, no. 11, p. 3541, 2016.

[88]   M. Mostefaoui, H. Mazari, S. Khelifi, A. Bouraiou, and R. Dabou, "Simulation of High Efficiency CIGS Solar Cells with SCAPS-1D Software," *Energy Procedia*, vol. 74, pp. 736–744, 2015.

[89]   H. Movla, "Optimization of the CIGS based thin film solar cells: Numerical simulation and analysis," *Optik (Stuttg).*, vol. 125, no. 1, pp. 67–70, 2014.

[90]   M. Saadat, M. Moradi, and M. Zahedifar, "CIGS absorber layer with double grading Ga profile for highly efficient solar cells," *Superlattices Microstruct.*, vol. 92, pp. 303–307, 2016.

[91]   K. Decock, J. Lauwaert, and M. Burgelman, "Characterization of graded CIGS solar cells," *Energy Procedia*, vol. 2, no. 1, pp. 49–54, 2010.

[92]   M. Gloeckler and J. R. Sites, "Band-gap grading in Cu(In,Ga)Se2 solar cells," *J. Phys. Chem. Solids*, vol. 66, no. 11, pp. 1891–1894, 2005.

[93]   A. Belghachi and N. Limam, "Effect of the absorber layer band-gap on CIGS solar cell," *Chinese J. Phys.*, vol. 55, no. 4, pp. 1127–1134, 2017.

[94]   M. B. and J. Marlein, "ANALYSIS OF GRADED BAND GAP SOLAR CELLS WITH SCAPS Marc," in *ANALYSIS OF GRADED BAND GAP SOLAR CELLS WITH SCAPS Marc*, 2008, pp. 69–73.

[95]   B. Peace *et al.*, "Characterization of Cu(In,Ga)Se2 (CIGS) films with varying gallium ratios," *J. Alloys Compd.*, vol. 657, pp. 873–877, 2016.

[96]   T. Kato, J. L. Wu, Y. Hirai, H. Sugimoto, and V. Bermudez, "Record Efficiency for Thin-Film Polycrystalline Solar Cells Up to 22.9% Achieved by Cs-Treated Cu(In,Ga)(Se,S)2," *IEEE J. Photovoltaics*, vol. 9, no. 1, pp. 325–330, 2019.

[97]   X. Song *et al.*, "Na incorporation into Cu(In,Ga)Se 2 thin-film solar cell absorbers deposited on polyimide: Impact on the chemical and electronic surface structure," *J. Appl. Phys.*, vol. 111, no. 3, 2012.

[98]   Y. C. Lin, K. T. Liu, T. P. Hsieh, and H. R. Hsu, "Improving Ga distribution and efficiency of flexible Cu(In,Ga)(S,Se) solar cell using CuGa:Na target route," *Mater. Sci. Semicond. Process.*, vol. 94, no. December 2018, pp. 151–155, 2019.

[99]   W. Li, X. Yan, A. G. Aberle, and S. Venkataraj, "Effect of sodium diffusion on the

properties of CIGS solar absorbers prepared using elemental Se in a two-step process," *Sci. Rep.*, vol. 9, no. 1, pp. 1–11, 2019.

[100] S. Siebentritt *et al.*, "Heavy Alkali Treatment of Cu(In,Ga)Se2 Solar Cells: Surface versus Bulk Effects," *Adv. Energy Mater.*, vol. 10, no. 8, 2020.

[101] M. I. Hossain, P. Chelvanathan, M. Zaman, M. R. Karim, M. A. Alghoul, and N. Amin, "Prospects of indium sulphide as an alternative to cadmium sulphide buffer layer in cis based solar cells from numerical analysis," *Chalcogenide Lett.*, vol. 8, no. 5, pp. 315–324, 2011.

[102] R. L. Garris *et al.*, "Efficient and stable CIGS solar cells with ZnOS buffer layer," *2014 IEEE 40th Photovolt. Spec. Conf. PVSC 2014*, pp. 353–356, 2014.

[103] V. Khomyak, I. Shtepliuk, V. Khranovskyy, and R. Yakimova, "Band-gap engineering of ZnO1-xSx films grown by rf magnetron sputtering of ZnS target," *Vacuum*, vol. 121, pp. 120–124, 2015.

[104] B. Sara, Z. Baya, and B. Zineb, "Investigation of Cu(In, Ga)Se2 solar cell performance with non-cadmium buffer layer using TCAD-SILVACO," *Mater. Sci. Pol.*, vol. 36, no. 3, pp. 514–519, 2018.

[105] S. Sharbati, S. H. Keshmiri, J. T. McGoffin, and R. Geisthardt, "Improvement of CIGS thin-film solar cell performance by optimization of Zn(O,S) buffer layer parameters," *Appl. Phys. A Mater. Sci. Process.*, vol. 118, no. 4, pp. 1259–1265, 2014.

[106] A. Timoumi, H. Bouzouita, M. Kanzari, and B. Rezig, "Fabrication and characterization of In2S3 thin films deposited by thermal evaporation technique," *Thin Solid Films*, vol. 480–481, pp. 124–128, 2005.

[107] E. Ghorbani and K. Albe, "Influence of Cu and Na incorporation on the thermodynamic stability and electronic properties of β-In2S3," *J. Mater. Chem. C*, vol. 6, no. 27, pp. 7226–7231, 2018.

[108] D. Hariskos, W. Hempel, R. Menner, and W. Witte, "Influence of substrate temperature during InxSy sputtering on Cu(In,Ga)Se2/buffer interface properties and solar cell performance," *Appl. Sci.*, vol. 10, no. 3, 2020.

[109] S. Spiering, A. Eicke, D. Hariskos, M. Powalla, N. Naghavi, and D. Lincot, "Large-

area Cd-free CIGS solar modules with In2S3 buffer layer deposited by ALCVD," *Thin Solid Films*, vol. 451–452, pp. 562–566, 2004.

[110] S. Ishizuka *et al.*, "Fabrication of wide-gap Cu(In1-xGa x)Se2 thin film solar cells: A study on the correlation of cell performance with highly resistive i-ZnO layer thickness," *Sol. Energy Mater. Sol. Cells*, vol. 87, no. 1–4, pp. 541–548, 2005.

[111] R. Scheer, L. Messmann-Vera, R. Klenk, and H. W.Schock, "On the role of non-doped ZnO in CIGSe solar cells," *Prog. PHOTOVOLTAICS Res. Appl. Prog.*, vol. 20, no. 6, pp. 1114–1129, 2012.

[112] S. Alhammadi, H. Park, and W. K. Kim, "Optimization of intrinsic ZnO thickness in Cu(In,Ga)Se2-based thin film solar cells," *Materials (Basel).*, vol. 12, no. 9, 2019.

[113] T. Minemoto, T. Negami, S. Nishiwaki, H. Takakura, and Y. Hamakawa, "Preparation of Zn1-xMgxO films by radio frequency magnetron sputtering," *Thin Solid Films*, vol. 372, no. 1, pp. 173–176, 2000.

[114] H. Heidarzadeh, A. Rostami, S. Matloub, M. Dolatyari, and G. Rostami, "Analysis of the light trapping effect on the performance of silicon-based solar cells: absorption enhancement," *Appl. Opt.*, vol. 54, no. 12, p. 3591, 2015.

[115] F. Larsson, "Window Layer Structures for Chalcopyrite Thin-Film Solar Cells," 2020.

[116] A. Kumar, A. Kumar Goyal, U. Gupta, Tanya, N. Gupta, and R. Chaujar, "Increased efficiency of 23% for CIGS solar cell by using ITO as front contact," *Mater. Today Proc.*, vol. 28, no. Part 1, pp. 361–365, 2020.

[117] Peter Y. Yu, *Fundamentals of semiconductors*, vol. 53, no. 9. 2005.

[118] J. S. Blakemore, *SEMICONDUCTOR STATISTICS*, vol. 1. 1962.

[119] D. Stefanakis and K. Zekentes, "TCAD models of the temperature and doping dependence of the bandgap and low field carrier mobility in 4H-SiC," *Microelectron. Eng.*, vol. 116, pp. 65–71, 2014.

[120] Y. P. Varshni, "TEMPERATURE DEPENDENCE OF THE ENERGY GAP IN SEMICONDUCTORS," *Physica*, vol. 34, no. 1, pp. 149–154, 1967.

[121] N. Cavassilas, J. L. Autran, F. Aniel, and G. Fishman, "Energy and temperature

dependence of electron effective masses in silicon," *J. Appl. Phys.*, vol. 92, no. 3, pp. 1431–1433, 2002.

[122] V. K. Khanna, *Temperature effects on semiconductor*, vol. 4, no. 1. 2020.

[123] P. Jackson *et al.*, "New world record efficiency for Cu(In,Ga)Se2 thin-film solar cells beyond 20%," *Prog. Photovoltaics Res. Appl.*, vol. 19, no. 6, pp. 894–897, 2011.

[124] G. Siefer and A. W.Bett, "Analysis of temperature coefficients for III–V multi-junction concentrator cells," *Prog. Photovoltaics Res. Appl.*, vol. 22, no. 5, pp. 515–524, 2012.

[125] M. Gloeckler, C. R. Jenkins, and J. R. Sites, "Explanation of Light/Dark Superposition Failure in CIGS Solar Cells," *Mater. Res. Soc. Symp. - Proc.*, vol. 763, pp. 231–236, 2003.

[126] L. C. Hirst and J. E.-D. Nicholas, "Fundamental losses in solar cells," *Prog. Photovoltaics Res. Appl.*, vol. 19, no. 3, pp. 286–293, 2010.

[127] M. A. Alam and M. Ryyan Khan, "Fundamentals of PV efficiency interpreted by a two-level model," *Am. J. Phys.*, vol. 81, no. 9, pp. 655–662, 2013.

[128] A. Nikolaeva *et al.*, "Electrostatic potential fluctuations and light-soaking effects in Cu(In,Ga)Se2 solar cells," *Prog. Photovoltaics Res. Appl.*, vol. 28, no. 9, pp. 919–934, 2020.

[129] J. A. Del Cueto, S. Rummel, B. Kroposki, C. Osterwald, and A. Anderberg, "Stability of CIS/CIGS modules at the outdoor test facility over two decades," *Conf. Rec. IEEE Photovolt. Spec. Conf.*, 2008.

[130] J. A. Del Cueto and B. Von Roedern, "Long-term Transient and Metastable Effects in Cadmium Telluride Photovoltaic Modules," *Prog. Photovoltaics Res. Appl.*, vol. 14, no. 7, pp. 615–628, 2006.

[131] S. Chen *et al.*, "Light soaking induced doping increase and sodium redistribution in Cu(In,Ga)Se2-based thin film solar cells," *Thin Solid Films*, vol. 582, pp. 35–38, 2015.

[132] C. A. Deline, J. A. del Cueto, D. S. Albin, and S. R. Rummel, "Metastable electrical characteristics of polycrystalline thin-film photovoltaic modules upon exposure and stabilization," *Reliab. Photovolt. Cells, Modul. Components, Syst. IV*, vol. 8112, no.

Bibliography

September, p. 81120T, 2011.

[133] F. Liu, C. Yan, K. Sun, F. Zhou, X. Hao, and M. A. Green, "Light-Bias-Dependent External Quantum Efficiency of Kesterite Cu2ZnSnS4 Solar Cells," *ACS Photonics*, vol. 4, no. 7, pp. 1684–1690, 2017.

[134] O. Breitenstein, P. Altermatt, K. Ramspeck, M. A. Green, J. Zhao, and A. Schenk, "Interpretation of the commonly observed I-V characteristics of C-SI cells having ideality factor larger than two," *Conf. Rec. 2006 IEEE 4th World Conf. Photovolt. Energy Conversion, WCPEC-4*, vol. 1, pp. 879–884, 2006.

[135] S. S. Hegedus and W. N. Shafarman, "Thin-film solar cells: Device measurements and analysis," *Prog. Photovoltaics Res. Appl.*, vol. 12, no. 2–3, pp. 155–176, 2004.

[136] M. A. Green, "Solar cells—Operating principles, technology and system applications," *Sol. Energy*, vol. 28, no. 5, p. 447, Jan. 1982.

[137] S. Siebentritt, "What limits the efficiency of chalcopyrite solar cells?," *Sol. Energy Mater. Sol. Cells*, vol. 95, no. 6, pp. 1471–1476, 2011.

[138] M. Richter, M. S. Hammer, T. Sonnet, and J. Parisi, "Bandgap extraction from quantum efficiency spectra of Cu(In,Ga)Se2 solar cells with varied grading profile and diffusion length," *Thin Solid Films*, vol. 633, pp. 213–217, 2017.

[139] T. K. Todorov *et al.*, "Beyond 11% efficiency: Characteristics of state-of-the-art Cu2ZnSn(S,Se)4 Solar Cells," *Adv. Energy Mater.*, vol. 3, no. 1, pp. 34–38, 2013.

[140] U. Rau, B. Blank, T. C. M. Müller, and T. Kirchartz, "Efficiency Potential of Photovoltaic Materials and Devices Unveiled by Detailed-Balance Analysis," *Phys. Rev. Appl.*, vol. 7, no. 4, pp. 1–9, 2017.

[141] R. Carron *et al.*, "Bandgap of thin film solar cell absorbers: A comparison of various determination methods," *Thin Solid Films*, vol. 669, pp. 482–486, 2019.

[142] H. Helmers, C. Karcher, and A. W. Bett, "Bandgap determination based on electrical quantum efficiency," *Appl. Phys. Lett.*, vol. 103, no. 3, 2013.

[143] T. Kodalle *et al.*, "Glow discharge optical emission spectrometry for quantitative depth profiling of CIGS thin-films," *J. Anal. At. Spectrom.*, vol. 34, no. 6, pp. 1233–1241, 2019.

[144] T. Dalibor *et al.*, "Advanced PVD buffers on the road to GW-scale CIGSSe production," in *Conference Record of the IEEE Photovoltaic Specialists Conference*, 2016, vol. 2016-November, pp. 1433–1437.

[145] H.-J. Yu *et al.*, "Light-soaking effects and capacitance profiling in Cu(In,Ga)Se$_2$ thin-film solar cells with chemical-bath-deposited ZnS buffer layers," *Phys. Chem. Chem. Phys.*, vol. 18, no. 48, pp. 33211–33217, Dec. 2016.

[146] H. Elanzeery, F. Babbe, M. Melchiorre, F. Werner, and S. Siebentritt, "High-performance low bandgap thin film solar cells for tandem applications," *Prog. Photovoltaics Res. Appl.*, vol. 26, no. 7, pp. 437–442, Jul. 2018.

[147] P. Würfel, *Physics of solar cells*. Wiley VCH, 2009.

[148] N. Sze, S., M.; Kwok, K., *Physics of Semiconductor Devices*. John Wiley & Sons, Inc., 2006.

[149] Y. Aida, V. Depredurand, J. K. Larsen, H. Arai, D. Tanaka, and M. Kurihara, "Cu-rich CuInSe$_2$ solar cells with a Cu-poor surface," *Prog. Photovoltaics Res. Appl.*, vol. 23, no. 6, pp. 754–764, 2015.

[150] J. M. Raguse, C. P. Muzzillo, J. R. Sites, and L. Mansfield, "Effects of Sodium and Potassium on the Photovoltaic Performance of CIGS Solar Cells," *IEEE J. Photovoltaics*, vol. 7, no. 1, pp. 303–306, 2017.

[151] T. Song, J. T. McGoffin, and J. R. Sites, "Interface-barrier-induced J-V distortion of CIGS cells with sputtered-deposited Zn(S,O) window layers," *IEEE J. Photovoltaics*, vol. 4, no. 3, pp. 942–947, 2014.

[152] S. H. Wei, S. B. Zhang, and A. Zunger, "Effects of Ga addition to CuInSe2 on its electronic, structural, and defect properties," *Appl. Phys. Lett.*, vol. 72, no. 24, pp. 3199–3201, 1998.

[153] M. Suja, S. B. Bashar, M. M. Morshed, and J. Liu, "Realization of Cu-doped p-type ZnO thin films by molecular beam epitaxy," *ACS Appl. Mater. Interfaces*, vol. 7, no. 16, pp. 8894–8899, 2015.

[154] S. Grover, J. V. Li, D. L. Young, P. Stradins, and H. M. Branz, "Reformulation of solar cell physics to facilitate experimental separation of recombination pathways," *Appl.*

Phys. Lett., vol. 103, no. 9, 2013.

[155] M. Boubakeur, A. Aissat, M. Ben Arbia, H. Maaref, and J. P. Vilcot, "Enhancement of the efficiency of ultra-thin CIGS/Si structure for solar cell applications," *Superlattices Microstruct.*, vol. 138, no. December 2019, p. 106377, 2020.

[156] G. Hanna, A. Jasenek, U. Rau, and H. W. Schock, "Influence of the Ga-content on the bulk defect densities of Cu(In,Ga)Se2," *Thin Solid Films*, vol. 387, no. 1–2, pp. 71–73, May 2001.

[157] R. E. Brandt, N. M. Mangan, J. V. Li, Y. S. Lee, and T. Buonassisi, "Determining interface properties limiting open-circuit voltage in heterojunction solar cells," *J. Appl. Phys.*, vol. 121, no. 18, 2017.

[158] U. Rau and M. Schmidt, "Electronic properties of ZnO/CdS/Cu(In,Ga)Se2 solar cells - Aspects of heterojunction formation," *Thin Solid Films*, vol. 387, no. 1–2, pp. 141–146, 2001.

[159] N. Nicoara *et al.*, "Direct evidence for grain boundary passivation in Cu(In,Ga)Se2 solar cells through alkali-fluoride post-deposition treatments," *Nat. Commun.*, vol. 10, no. 1, pp. 1–8, 2019.

[160] B. Idris, Z. Rafik, D. Kamal, B. Abdessalam, and G. Faouzi, "Size and grain-boundary effects on the performance of polycrystalline CIGS-based solar cells," *2015 6th Int. Renew. Energy Congr. IREC 2015*, pp. 1–5, 2015.

Publications

1. **H. Ahmed**, M. Elshabasi, J. Ohland, M. Stölzel, A. Weber, R. Lechner, T. Dalibor, J. Parisi, S. Schäfer and S. J. Heise, "Temperature coefficient characterization of CIGSSe solar cells with layer modifications," *Sol. Energy Mater. Sol. Cells*, vol. 225, p. 111059, 2021.
2. **H. Ahmed** *et al.*, "Identifying dominant recombination locations in double-graded CIGSSe solar cells and their impact on the performance at different light intensities" (To be published).
3. **H. Ahmed** *et al.*, "Buffer-absorber layer configurations' influence on metastable Fill Factor temperature coefficients of CIGSSe solar cells" (To be published).

Acknowledgements

During my PhD journey I have met several people who contributed to finalizing my thesis. Therefore, I would like to take the opportunity to thank them.

Particularly, I would like to convey my sincere gratitude to Prof. Sascha Schäfer for his constant professional support, flexibility, stoic patience, fairness, and his attentive care to the details of my research. His scientific skills pushed me to sharpen my thinking and improved my work level. I am really honored that I was a part of his research group.

I would also like to deeply thank Prof. Jürgen Parisi for getting the fund to this project, and for always having open doors to discuss tirelessly. Furthermore, for his high encouragement, accurate revisions of my thesis and constant help to publish my work. It was privilege to work under his leadership and to learn from his prosperous experience.

I express my gratitude to Prof. Carsten Agert and Prof. Michael Wark for their immediate will to examine my thesis and for assessing the work.

I profoundly thank Dr. Michael Richter for believing in my abilities and for considering my application of this position. I really appreciate his effective involvement for revising my thesis and for the intensive discussion of my papers. Thanks to his existence, it made me more enthusiast and kept me on track. I also would like to thank Dr. Stephan Heise for taking over the project leader position in difficult times and for his scientific suggestions. I acknowledge Dr. Levent Gütay for permanently distributing positive energy and for his rich scientific discussions. To Dr. Devendra Pareek for his scientific and personal useful advices.

A special thanks for Dr. Marko Stölzel, Robert Lechner, Thomas Dalibor, Alfons Weber and Jörg Palm for their wealthy experienced discussions on the CIGS field and for their nice and close cooperation.

I would like deeply thank Mohamed Elshabasi, my student, for spending days and nights in the laboratory to help me particularly with the measurements. I must admit that his help was of great contribution to my work. My appreciation and gratitude to my friend Marco Gonzalez for his help specially in my delicate health moments and for his fruitful scientific discussions. Of course, the positive vibes' atmosphere from my colleagues, Lukas Büsing, Aldana Lilén, Timo Pfeiffelmann, David Novak, Alexandra Janina Erdt, Nedal Gewo and Ashwin Hariharan worth

D Erklärung

Hiermit erkläre ich, dass ich die vorliegende Dissertation selbstständig verfasst und nur die angegebenen Hilfsmittel benutzt habe.

Personal Information

Name	Hamsa Ahmed
Birth	Alexandria, 16.09.1991
Nationality	Egyptian

Education

1996-2009	École Des Religieuses Franciscaines, Ibrahimieh

10/2009-07/2014	**Bachelor of Science in Communication Engineering & Electronics**: *Arab Academy for Science, Technology & Maritime Transport (AAST), Alexandria, Egypt*

- Excellent degree with honors
- Top ranking Student
- **Senior Project** "Investigation on Ground to Train Free Space Optical Based Communications''

Tutor of Calculus lecture at AAST

Internship: *Vodafone, Egypt*

- Telecommunications network installation and configuration

10/2014-02/2017	**Master of Science in Optics and Photonics**: *KIT, Karlsruhe, Germany*

- Specialization: Optical Systems
- Thesis "Development of Laser-Induced Breakdown Spectroscopy (LIBS) spectrometer and enhancement of the Spectral Resolution", in *Secopta Company, Berlin, Germany.*

Internship: *Bruker Optik GmbH Ettlingen.*

- Optimizing FTIR spectrometer by improving the geometry of He-Ne Laser, Near-and-mid-IR source and KBR beam splitter, Mirrors, DTGS and MCT detectors.

	- Perform a testing scheme for IR detectors, such as: LWIR, PV-MCT and FPA.
	- Development of FTR spectrometer performance by replacing a new beam splitter and getting the optimum distance of the mirrors at the detector.
10/2017-to date	**Ph.D. in Physics**: *University of Oldenburg, Oldenburg, Germany.* - **Thesis** "Performance Optimization of $Cu(In_{1-x},Ga_x)(Se_{1-y}, S_y)_2$ Thin-Film Solar Cells by Characterization and Modelling of Temperature and Low-Light Behavior" **Teacher Assistant**: *University of Oldenburg, Oldenburg, Germany.* Solid State Physics, Applied Mechanics and Electrodynamics.